Time-varying all-optical systems using highly nonlinear epsilon-near-zero materials

Mohammad Karimi

A thesis submitted to the University of Ottawa in partial fulfillment of the requirements for the degree of Doctor of Philosophy in Electrical Engineering.

The Ottawa-Carleton Institute for
Electrical and Computer Engineering
November, 2023

Abstract

Nonlinear optics represents a significant area of research and technology concerned with the modification of material optical properties using light. The interaction between light and such materials gives rise to a multitude of nonlinear optical effects, including second harmonic generation, third harmonic generation, high harmonic generation, and sum frequency generation. This thesis focuses on a specific and relevant nonlinear phenomenon within this field, namely the nonlinear Kerr effect, which involves the modification of a material's refractive index through the exposure to an intense beam of light. The nonlinear Kerr effect holds promise for various applications, such as self-phase modulation in laser technology and the utilization of optical solitons in telecommunications. However, the limited availability of materials with sufficiently strong Kerr effects often restricts the practical application of this effect across different industries.

Concurrently, optical time-varying systems play crucial roles in modern technologies, including optical modulators, LiDAR systems, and adaptive cameras. These systems involve the dynamic modification of optical properties. To achieve ultra-fast modulation of light properties, it is beneficial to explore materials with ultra-fast modulation speeds of the optical refractive index for integration into time-varying systems. While electro-optical effects represent the most common methods for achieving high-speed modulation of the effective refractive index, the utilization of all-optical methods, such as the nonlinear Kerr effect, presents an alternative approach. Nevertheless, the absence of simultaneous high speed and large nonlinear Kerr response in the majority of well-established materials restricts the utilization of the Kerr effect in time-varying systems.

This thesis focuses on the study of a group of materials known as epsilon-near-zero (ENZ) materials, where the real part of the permittivity vanishes at a specific wavelength referred to as the ENZ wavelength. Specifically, indium-tin-oxide (ITO), a transparent conducting oxide, is investigated, with its ENZ wavelength falling within the infrared region of the electromagnetic spectrum. ITO has been shown to possess a record-breaking large nonlinear Kerr effect with sub-picosecond response times, making it an excellent candidate for all-optical time-varying systems. The primary objective of this research is to investigate the applications of this large, fast nonlinear response and, where possible, enhance its effectiveness.

One notable application of rapid and substantial modifications in the refractive index of a material is adiabatic wavelength conversion of light. In one project, a thin layer of ITO is subjected to a pump-probe setup, where an intense pump beam of light triggers the nonlinear response of ITO, causing the refractive index to rapidly change while a probe beam passes through the modulated system. Consequently, the wavelength of the probe beam undergoes conversion.

Furthermore, it has been demonstrated that the nonlinear response of ITO can be significantly enhanced in the presence of a plasmonic metasurface. Metasurfaces consist of two-dimensional arrays of sub-wavelength scattering objects capable of manipulating the vectorial properties of light. In another project, we design a gradient metasurface composed of gold placed over ITO, enabling the diffraction of incident light into various diffraction orders depending on the ratio between the wavelength of light and the periodicity of the metasurface. This unique property is utilized to dynamically steer the diffraction orders of the probe beam, achieving wavelength conversion by exciting the nonlinear response of the ITO substrate with a second pump beam.

Additionally, we investigate the interaction of resonance modes in an amorphous silicon metasurface, known as Mie modes, with an inherently dark mode in a thin layer of ITO known as the ENZ mode. Through experimental and analytical approaches, we demonstrate that two fundamental Mie modes, electric dipole resonance and magnetic dipole resonance, can strongly couple with the ENZ mode. This strong coupling creates a highly complex system with a large and rapid nonlinear response, enabling the manipulation of light on sub-picosecond timescales.

In our final main project, we delve into investigating the nonlinear response of ITO nanoparticles. To accomplish this, we put forth a numerical recursive approach that allows us to incorporate the significant nonlinear Kerr effect of ITO into inherently linear simulation environments. Subsequently, we employ this proposed method to extract the scattering pattern of sub-wavelength antennas fabricated from ITO in both linear and nonlinear optical regimes. Our objective is to explore the potential applications of ITO nanoantennas in various fields.

Moreover, this thesis encompasses other projects related to ENZ materials. We investigate the nonlinear response of an artificially created ENZ medium by stacking subsequent layers of materials with negative and positive permittivities within the visible range of the electromagnetic spectrum. Additionally, we explore the nonlinear response of nanoparticles made of ITO. Lastly, we present our investigations into the strong coupling of the ENZ mode in a thin layer of ITO with surface plasmon polaritons in a layer of gold in contact with ITO.

I want to dedicate this thesis to my dear wife, Maryam, and also to honor the memory of my mother, Fereshteh. Both of these wonderful women have provided me with unconditional support and invaluable guidance throughout my life, leading me to where I am today.

Acknowledgment

I would like to express my sincere gratitude to Professor Robert W. Boyd for offering me an exceptional opportunity to work within one of the preeminent groups in the field of nonlinear optics and quantum photonics. Furthermore, I extend my heartfelt appreciation to Dr. M. Zahirul Alam for our insightful discussions on epsilon-near-zero optics and for the valuable opportunities he has provided me throughout the years.

I am immensely grateful to Dr. Jeremy Upham and Dr. Orad Reshef, whose unwavering support and patient guidance have been instrumental in shaping my journey. I am indebted to Dr. Yiyu Zhou and Mr. Tony Oliviery, who served as my initial mentors in the optical laboratory and clean room facilities, respectively.

Additionally, I wish to acknowledge the exceptional mentorship of Dr. Rasoul Alaei and Dr. Akbar Safari throughout my Ph.D. studies. I am deeply appreciative of the patience and assistance I received from Mr. Hugo Begin and Ms. Gloria Kaneza, the financial managers of our research group.

Finally, I would like to express my profound gratitude to all my colleagues who have made my path more manageable during these years. Among them, I would like to specifically mention Dr. Kashif Awan, Ms. Sisira Suresh, Mr. Yaswant Vaddi, Mr. Theng Loo Lim, Mr. Ryan Hogan, Dr. Lin Cheng, Dr. Boris Braverman, Dr. Enno Giese, Dr. Robert Fickler, Dr. Samuel Lemieux, Dr. Saad Bin Alam, Mr. Jeremy Rioux, Mr. Justin Gagnon, Ms. Maryam Amiri, Mr. Soheil Zibod, Dr. Payman Rasekh, Dr. Zohreh Hirbodvash, Dr. Ehsan Mobini, Dr. Wuhong Zhang, and Ms. Saumya Choudhary. Their collaboration and support have been invaluable to my research endeavors.

Table of Content

List of Figures

Appendix I:

Appendix II:

List of Abbreviations

ENZ	Epsilon Near Zero
ITO	indium tin oxide
DO	Diffraction Order
AWC	Adiabatic Wavelength Conversion
SEM	Scanning Electron Microscopy
FDTD	Finite Difference Time Domain
FEM	Finite Element Method
a-Si	amorphous silicon
EDR	Electric Dipole Resonance
MDR	Magnetic Dipole Resonance
fs	femtosecond
ps	picosecond
EQ	Electric Quadrupole
MQ	Magnetic Quadrupole
ext	extinction
sca	scattering
abs	absorption
OSA	Optical Spectrum Analyzer
TMM	Transfer Matrix Method
SPP	Surface Plasmon Polariton
LiDAR	Light Detection and Ranging

Chapter 1

Introduction

Background

Our goal in this thesis is to investigate the ultrafast all-optical time-varying systems based on the large and fast nonlinear response of epsilon-near-zero (ENZ) materials, the ones with the real part of their permittivity vanishing in a specific ENZ wavelength, with a special focus on indium-tin-oxide (ITO). ITO is a transparent conducting oxide where the real part of its permittivity vanishes in the infrared region, which makes it a perfect candidate for all-optical experiments in important communication wavelengths around 1300 nm and 1550 nm. Prior to the start of my Ph.D., our research group showed that thin layers of ITO show record-breaking nonlinear refractive indices with sub-picosecond modulation times around the ENZ wavelength.[1] The main focus of my research in my doctoral studies was to utilize that massive nonlinear response in practical applications and, in some cases, try to make the response even stronger. The structure of this thesis is article-based. I chose 3 accepted (chapters 2, 3, and 5) and 1 submitted (chapter 4) paper for the main body of the thesis, plus 2 accepted papers for the appendix part. I was a contributing co-author in all six of these projects, but I have elected to prioritize those where I was actively involved in all aspects of the project from beginning to end. Another criterion is to keep the harmony of the thesis and make the chapters reasonably connected with each other. In the rest of this chapter, I will first provide a short background on different fields related to my research. I will then use the material in the background section to elaborate on the idea behind each of the projects I have done in my Ph.D. separately and why they are important. I will also state the relation between different chapters. The statements of collaboration preceding each chapter describe my responsibilities and direct contributions to each project.

Nonlinear Optics

Nonlinear optics is a subfield of optics that deals with the interaction between light and matter in materials that exhibit nonlinear properties.[2] In other words, nonlinear optics studies how the behavior of light changes when it passes through materials that do not follow the linear relationship between the electric field and the induced polarization.[3] The principles of nonlinear optics are based on the fact that the polarization induced in a material by an electric field is not always proportional to the field strength.[2] This leads to a variety of nonlinear optical effects, such as frequency mixing, high-harmonic generation, and optical parametric amplification.

Frequency mixing is one of the most fundamental nonlinear optical effects. It occurs when two or more electromagnetic waves with different frequencies interact with a nonlinear material. The interaction between the waves generates new frequencies that are equal to the sum or difference of the original frequencies. This process is used in frequency converters, where high-frequency signals are converted into lower frequencies for transmission over long distances.

Second-harmonic generation is another important nonlinear optical effect. It occurs when a material produces light with a frequency that is twice that of the incident light. This process is used in green laser pointers, where the green light is produced by doubling the frequency of an infrared laser.[3] Second-harmonic generation is also used in microscopy, where it provides a powerful tool for studying biological samples.[4]

Optical parametric amplification is a third nonlinear optical effect that has important applications in laser technology. It occurs when an intense laser beam interacts with a nonlinear material, creating a new beam that has a different frequency and polarization. This process is used to amplify laser pulses, which are used in a variety of scientific and industrial applications.[5]

In this thesis, our focus is on one of the nonlinear effects known as the nonlinear Kerr effect. The nonlinear Kerr effect describes the change in the refractive index of a material in response to an applied electric field, as in the following equation,[2]

$$n_2 = \frac{3}{4n_0 Re(n_0)\epsilon_0 c}\chi^{(3)} \tag{1}$$

where n_2 is the nonlinear refractive index, n_0 is the linear refractive index, ϵ_0 is the permittivity of the vacuum, c is the speed of light in vacuum, and $\chi^{(3)}$ is the third-order susceptibility of the material. With n_2 defined as in equation 1, the total refractive index of the material in a nonlinear regime is,[2]

$$n = n_0 + n_2 I \tag{2}$$

where I is the intensity of the light within the material.

The nonlinear Kerr effect has several important applications in optics. One of its most significant applications is in the field of laser technology, where it is used to generate ultrashort laser pulses. The Kerr effect allows for the creation of self-phase modulation, which occurs when the intensity of the laser pulse changes as it travels through a nonlinear medium. This modulation causes the frequency of the pulse to broaden, resulting in a shorter pulse duration.[5]

Another important application of the nonlinear Kerr effect is in telecommunications. Optical fibers, which are used to transmit information over long distances, suffer from dispersion, which causes different frequencies of light to travel at different speeds. This dispersion limits the bandwidth of optical fibers, which is a critical factor in modern communication systems. The nonlinear Kerr effect can be used to compensate for this dispersion by introducing a frequency-dependent change in the refractive index of the fiber. This effect, known as the Kerr effect-induced self-phase modulation, allows for the creation of solitons, which are ultrashort optical pulses that can propagate over long distances without dispersing.[5]

The nonlinear Kerr effect also plays a crucial role in nonlinear optics and photonics. It is used in the study of nonlinear propagation of light in materials, as well as in the design of optical devices such as switches and modulators. Nonlinear Kerr effect-based devices have several advantages over traditional devices, including higher efficiency, lower power consumption, and faster switching times.[2]

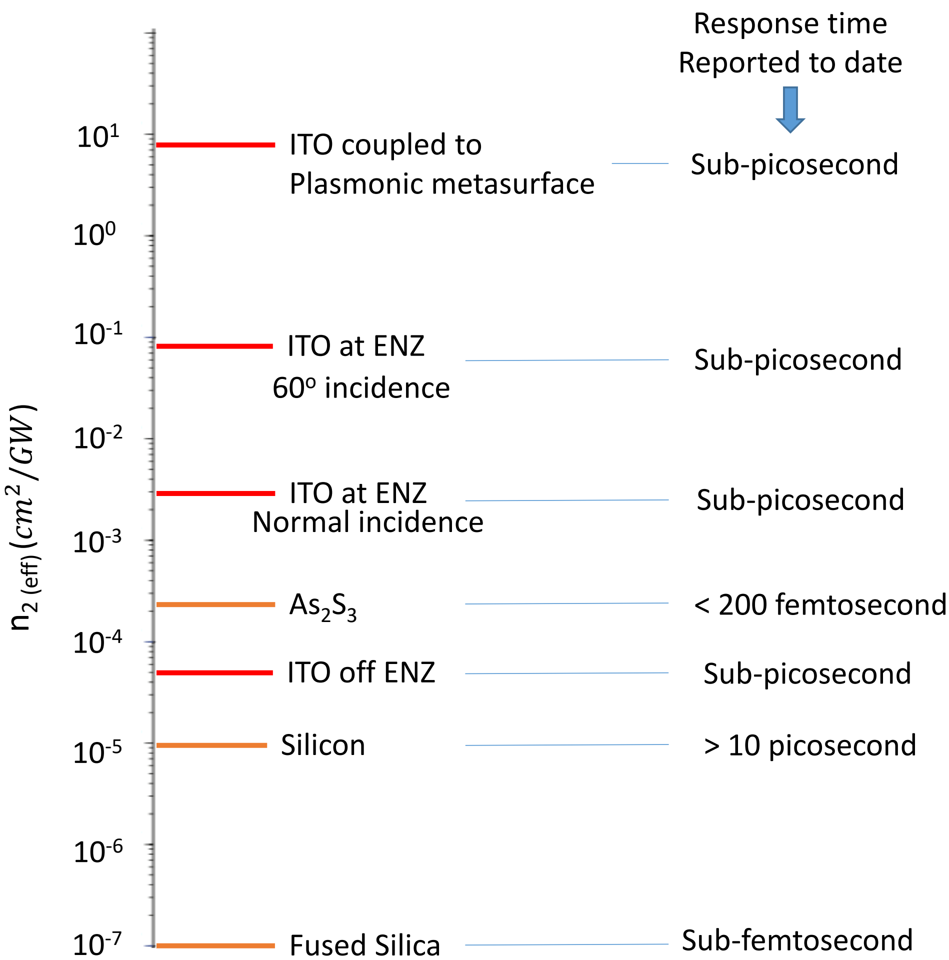

Figure 1: The comparison of the magnitude of the nonlinear refractive index in some famous materials for nonlinear Kerr effect. The column on the right side of each material specifies the order of the Kerr response time for that material that is reported up to date.[1,6–9]

Despite its many applications, the nonlinear Kerr effect presents significant challenges in the design and implementation of optical devices. One of the main challenges is to find materials with large enough nonlinear Kerr effect. As a point of reference, the nonlinear refractive index of fused silica is around $3 \times 10^{-7}\mathrm{cm}^2/\mathrm{GW}$. According to equation 2, one is required to apply an intensity of light at the order of 10^7GW/cm^2 in order to trigger the nonlinear Kerr effect in fused silica, which is not efficient for many practical applications.

Another challenge is the nonlinear response time of materials. The total response time can be evaluated as the addition of the rise and fall (also excitation and relaxation) times of the refractive index in response to the external excitation. For most of the materials, the rise time is much faster than the fall time, and it is usually limited by the duration of the pulse that triggers the nonlinearity. The total response time of materials to changes in the electric field is typically much slower than the duration of ultrashort pulses generating the Kerr effect. As a point of reference, for the case of silicon, the response time is in the order of 10s' of picoseconds due to the time taken for free carrier relaxation.[10,11] It means that if we excite a layer of silicon with an intense enough pulse of light with 100 fs duration, it takes more than 10 picoseconds for the refractive index of the silicon layer to go up and get back to the initial value. This limits the ability of Kerr effect-based devices to operate at high repetition rates.[5] Figure 1 compares the magnitude and response time of the Kerr effect in some typical materials. Note that the rise time of the material strongly depends on the duration of the pulse with which we excite the response, and the values demonstrated in the figure are what is reported up to the present moment. We observe that indium-tin-oxide (ITO) with a large and fast response can be an excellent candidate for applications based on the nonlinear Kerr effect.

Metasurfaces

Metasurfaces are 2D arrays of sub-wavelength scattering objects that can be used for controlling the vectorial properties of electromagnetic radiation.[16] These structures have been used for many different applications such as in making flat lenses,[12] holograms,[13] high-quality-factor resonators,[14] highly nonlinear platforms,[9] and vortex beam generators.[15] Figures 2 (a) to (d) demonstrate different types of metasurfaces used for flat lenses, holograms, high-Q resonators, and vector beams, respectively.

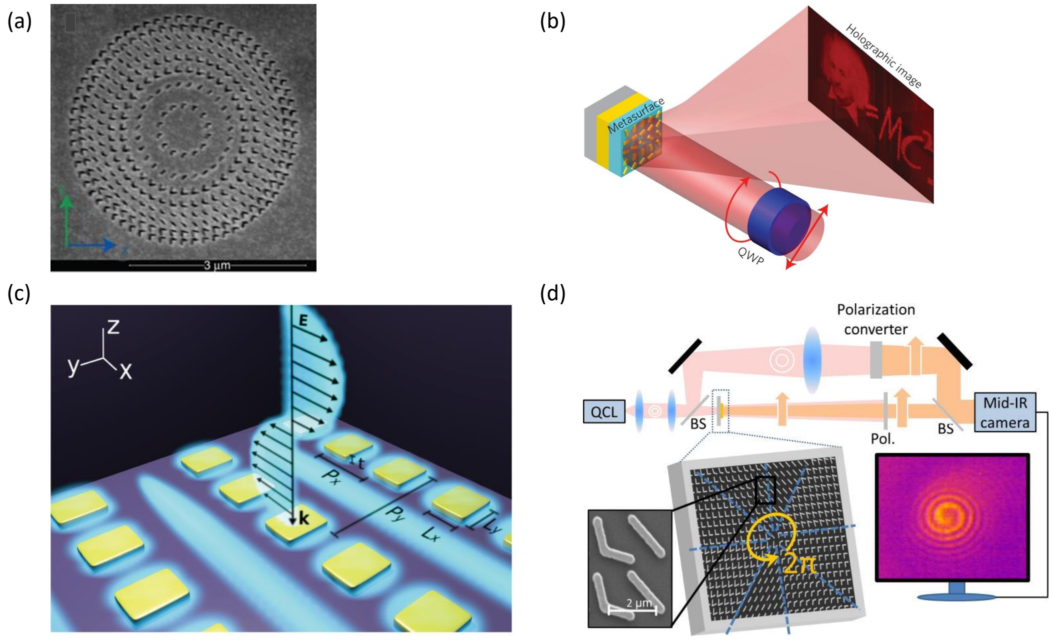

Figure 2: (a) The SEM image of a flat lens made by plasmonic nano-antennas,[12] (b) The schematics of a hologram made by metasurfaces,[13] (c) High-Q resonators using a plasmonic metasurface,[14] and (d) vector beam created by properly designed metasurfaces.[15] All of the figures are reprinted with permission from the related journals.

An important group of metasurfaces is gradient metasurfaces, where the electromagnetic response of the surface is position-dependent.[15] Figure 3 shows a simple scheme about the working mechanism of the gradient metasurface, which we used in chapter 3 of the thesis. Figures 3 (a) and (b) show one unit cell of such metasurface from top and side views, respectively. In this simple version of a gradient metasurface, we have antennas of different lengths in different positions. Due to different dimensions, each of these antennas is resonating at different wavelengths. As a result, when we excite the medium with a beam of light of a certain wavelength, the spectral distance of the resonance wavelength of each of the antennas to the excitation wavelength is different, and so is the amount of phase that each antenna introduces to the scattered field. As a consequence, The field effectively sees a phase ramp over the surface that scatters part of the incident beam to anomalous angles. Figure 3 (c) shows the phase and amplitude of the reflected field from metasurfaces with antennas of different lengths at the excitation wavelength of 1310 nm. It is noteworthy that

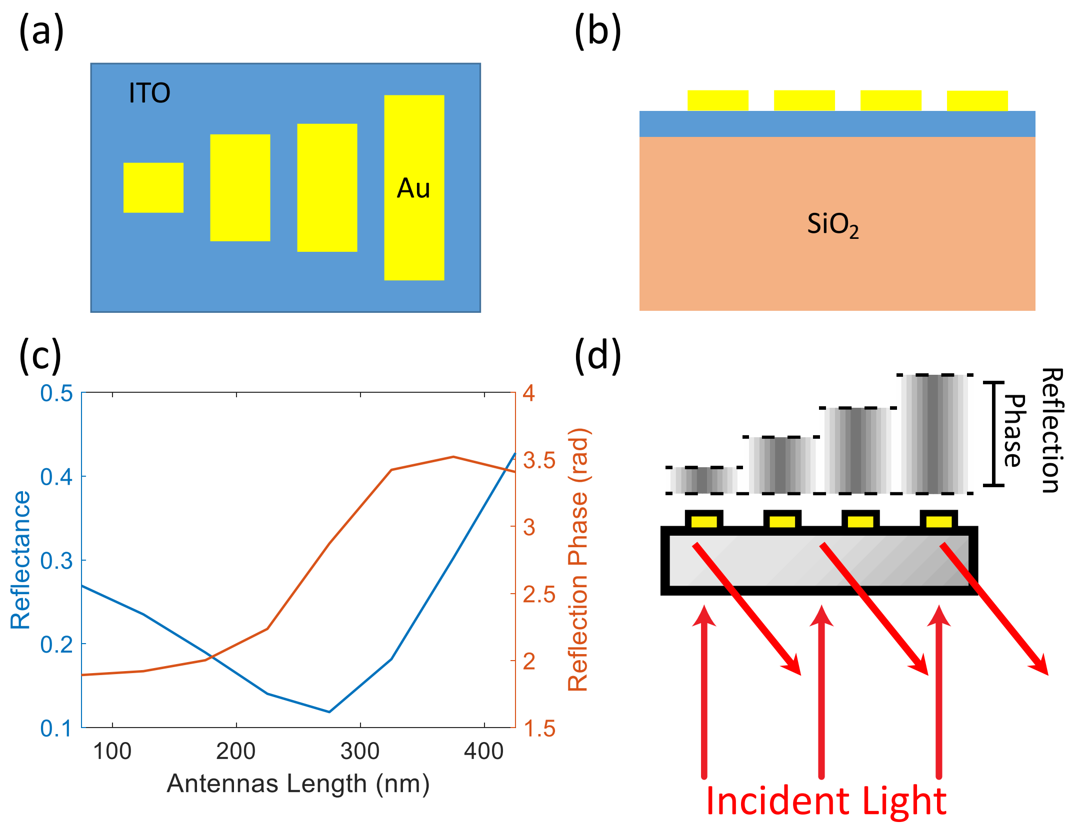

Figure 3: The schematics of a unit cell of the gradient metasurface used in the project related to chapter 3 of the thesis from top view (a) and side view (b). (c) shows the phase and amplitude of the reflected field from each of the antennas at the incident wavelength of 1310 nm. (d) shows a simple scheme of how the metasurface manipulates the vectorial properties of light.

due to the resonance nature of the device, the amplitude of the reflected field from each antenna is different. This affects the diffraction efficiency of the final metasurface, but we prioritized a larger phase distribution over uniform reflectance in our design. Figure 3 (d) shows a simple schematic of the mechanism that leads to the anomalous reflection of the beam from a gradient metasurface.

One application of such structures is to control the wave vector direction of the reflected or transmitted wave from the surface, known as anomalous reflection and refraction, respectively.[17] The underlying mechanism for this phenomenon is that the light that scatters from a sub-wavelength object experiences some phase shift that depends on the spectral distance between the central wavelength of the incident beam and the resonance wavelength of the object. If we prepare an array of differently sized scatterers that, as a result, have different resonance wavelengths, the incoming field experiences a position-dependent phase shift at the surface. This position-dependent phase shift produces an additional transverse k-vector, which consequently leads to an altered deflection angle of the scattered field.

Time-varying optical systems

Time-varying optical systems are of immense importance in a wide range of applications, such as in optical communications, light detection and ranging (LiDAR) systems, imaging, and sensing. These systems are designed to change their optical properties over time, allowing them to modulate light, adapt to changing environmental conditions, or capture dynamic scenes.

One of the applications of the optical time-varying systems related to this thesis is in the LiDAR systems. LiDAR is a remote sensing technology that uses optical technologies for environmental monitoring, urban planning, and autonomous vehicles.[18] It is based on the emission of laser pulses to different directions and analysis of the reflected beams for estimation of the distance, shape, and speed of the objects around. Such systems would benefit a lot from ultrafast optical beam steering devices to improve the speed of operation.

Moreover, time-varying optical systems are essential in developing photonic devices, such as optical communication networks. By using time-varying optical devices such as electro-optic modulators, optical switches, and optical amplifiers, researchers can develop high-speed communication networks capable of transmitting vast amounts of data over long distances. These photonic devices are critical for applications such as high-speed internet, medical diagnostics, and quantum computing.[19]

One of the major factors that limit the response time of optical systems is the inherent response time of materials in use. For example, the nonlinear optical response time of silicon, which is one of the most popular materials in optical technologies, is in the range of 10 picoseconds or more.[11] In this thesis, we investigate time-varying nonlinear systems where we can control the properties of the system in a sub-picosecond time scale using highly nonlinear epsilon-near-zero (ENZ) materials.

Epsilon-near-zero materials and their large fast nonlinear response

ENZ materials are a class of materials whose real part of permittivity vanishes at a specific wavelength, called ENZ wavelength. One can get a quick idea about the possibility of large nonlinear responses in such materials by looking at equation 1. We see that the nonlinear refractive index of the material reversely depends on the linear refractive index. As a result, if n_0 gets small, as in ENZ media around the ENZ wavelength, n_2 can get large.

From another point of view, the enhanced nonlinear response in ENZ materials can be attributed to the slow group velocity of light in such media.[20] When the group velocity of light is slow, the light spends more time in the material, allowing for more light-matter interactions. This leads to a higher nonlinear polarization and, thus, a stronger nonlinear response. Moreover, the nonlinear response in ENZ materials can be tailored by adjusting the material properties, such as the dielectric constant, thickness, and doping.[21]

ITO is a transparent conducting oxide (TCO) with a permittivity that follows the Drude model in the infrared (IR) region[22] as in equation 3 below:

$$\epsilon = \epsilon_\infty - \omega_p^2/(\omega^2 + i\gamma\omega) \tag{3}$$

, Where ϵ_∞ is the infinite frequency permittivity, ω_p is the plasma frequency, and γ is the damping rate. An exemplary plot of the permittivity of a thin layer of ITO is shown in figure 4 (a). The ENZ wavelength of ITO can be engineered in the infrared region of the spectrum by controlling the deposition conditions.

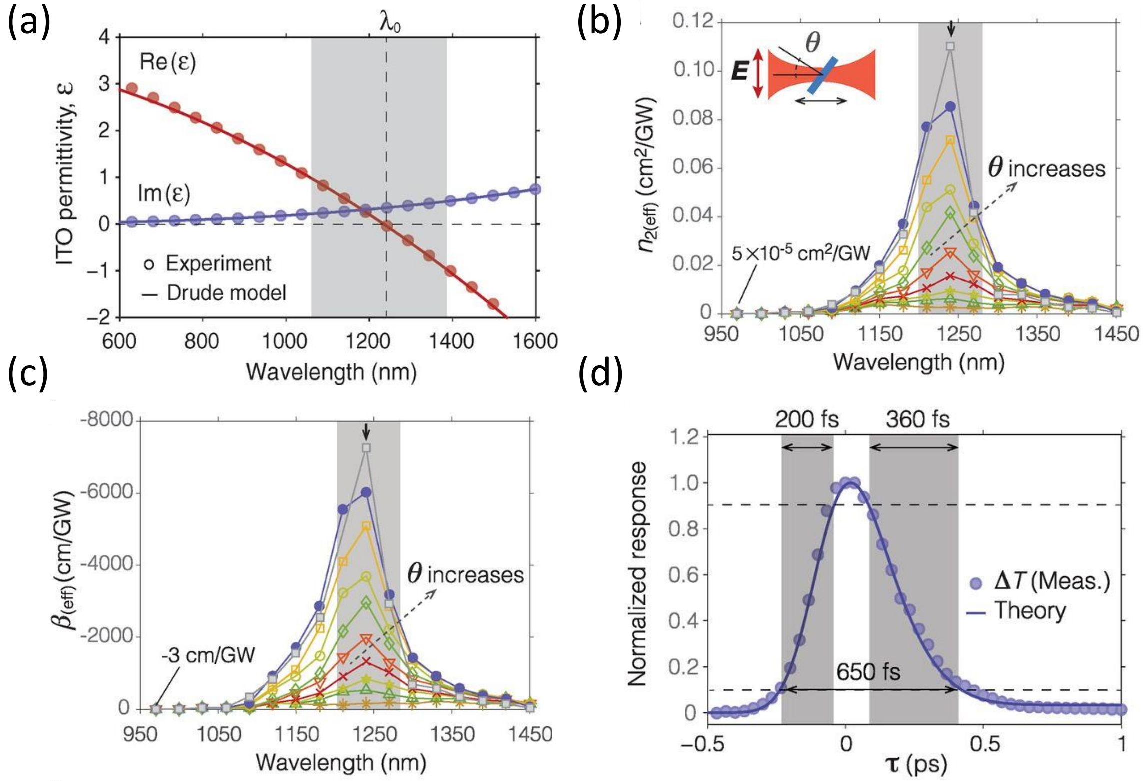

Figure 4: (a) The permittivity of a 310-nm layer of ITO using ellipsometry (circles) and Drude model (solid lines). (b) and (c) show the extracted nonlinear refractive index and nonlinear absorption, respectively, using the Z-scan technique at different wavelengths and different angles of incidence. (d) shows the response time of the effective collective temperature of the electrons of the conduction band of ITO to external excitation using the two-temperature model. All of the Figures are reprinted from reference[1] with permissions.

When a thin layer of ITO is illuminated with a sufficiently intense femtosecond (fs) laser pulse, the electrons in the conduction layer undergo an intraband energy level transition in a sub-picosecond time scale. As a result of this transition, the effective collective temperature of the electrons changes, which leads to the modification of the plasma frequency of the ITO layer. More details about this process can be found in the supplementary information of.[1] Finally, we see in equation 3 that any change in the plasma frequency leads to a modification of the refractive index of ITO. A 310 nm-thick film of ITO has been demonstrated to possess one of the largest ultrafast nonlinear refractive indices among solid materials.[1] Figures 4 (b) and (c) show the extracted nonlinear refractive index and nonlinear absorption coefficient at different wavelengths around the ENZ wavelength and at different angles of incidence, derived using Z-scan technique.[23] One can compare the magnitude of the nonlinear refractive index with that of fused silica mentioned above ($3 \times 10^{-7}\mathrm{cm}^2/\mathrm{GW}$). In addition to the large magnitude of the nonlinear response of ITO, it is also extremely fast compared to what has been reported before for other materials. Figure 4 (d) shows the change of the effective collective temperature of the electrons of the conduction band of ITO in response to an external excitation derived from the two-temperature model. We see that the temperature goes up in a 200 fs time-scale as the electrons undergo an intraband transition and come down in a slightly slower process as the electrons transfer their extra energy to the lattice due to electron-phonon interactions. The whole process happens in a sub-picosecond time scale, which can be compared to the time scales of the nonlinear response of silicon mentioned above (longer than 10 picoseconds).

The nonlinear response of ITO can be enhanced further when an array of properly designed plasmonic nanoantennas is placed over the ITO layer as in Figures 5 (a) and (b).[9] Figure 5 (c) shows the linear transmittance of light through the sample in measurement and experiment and demonstrates that the resonance wavelength of the plasmonic metasurface is around the ENZ region. One reason for this enhancement is that the nanoantennas can confine light inside the ITO layer when they are near their resonance condition. Another reason is that the ENZ mode within the ITO layer couples to the electric dipole resonance of an array of plasmonic nanoantennas.[9] This happens when the resonance of the antennas oc-

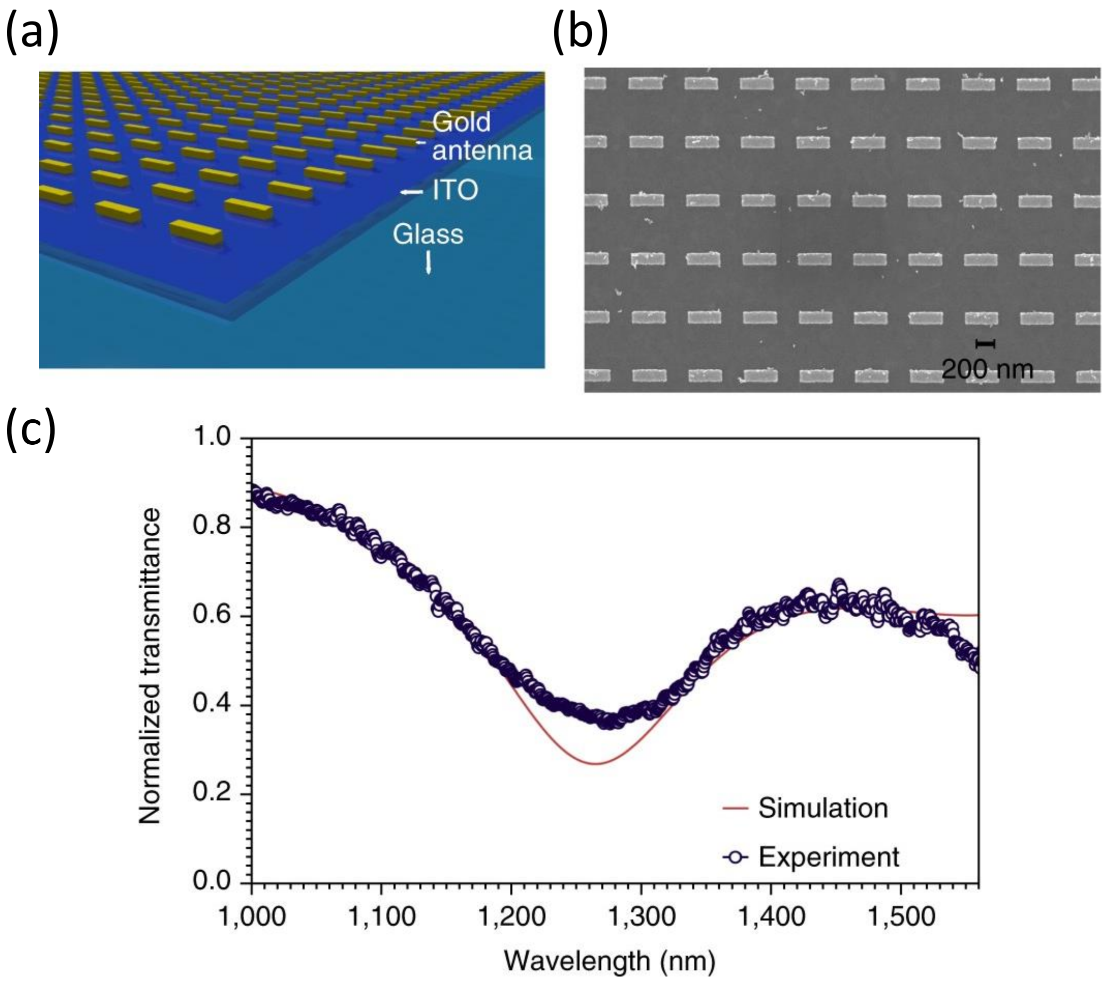

Figure 5: (a) The schematics of a plasmonic metasurface over ITO and (b) the SEM image of the fabricated sample. (c) shows the linear transmittance of light through the sample in simulation and experiment. All of the Figures are reprinted from reference[9] with permission.

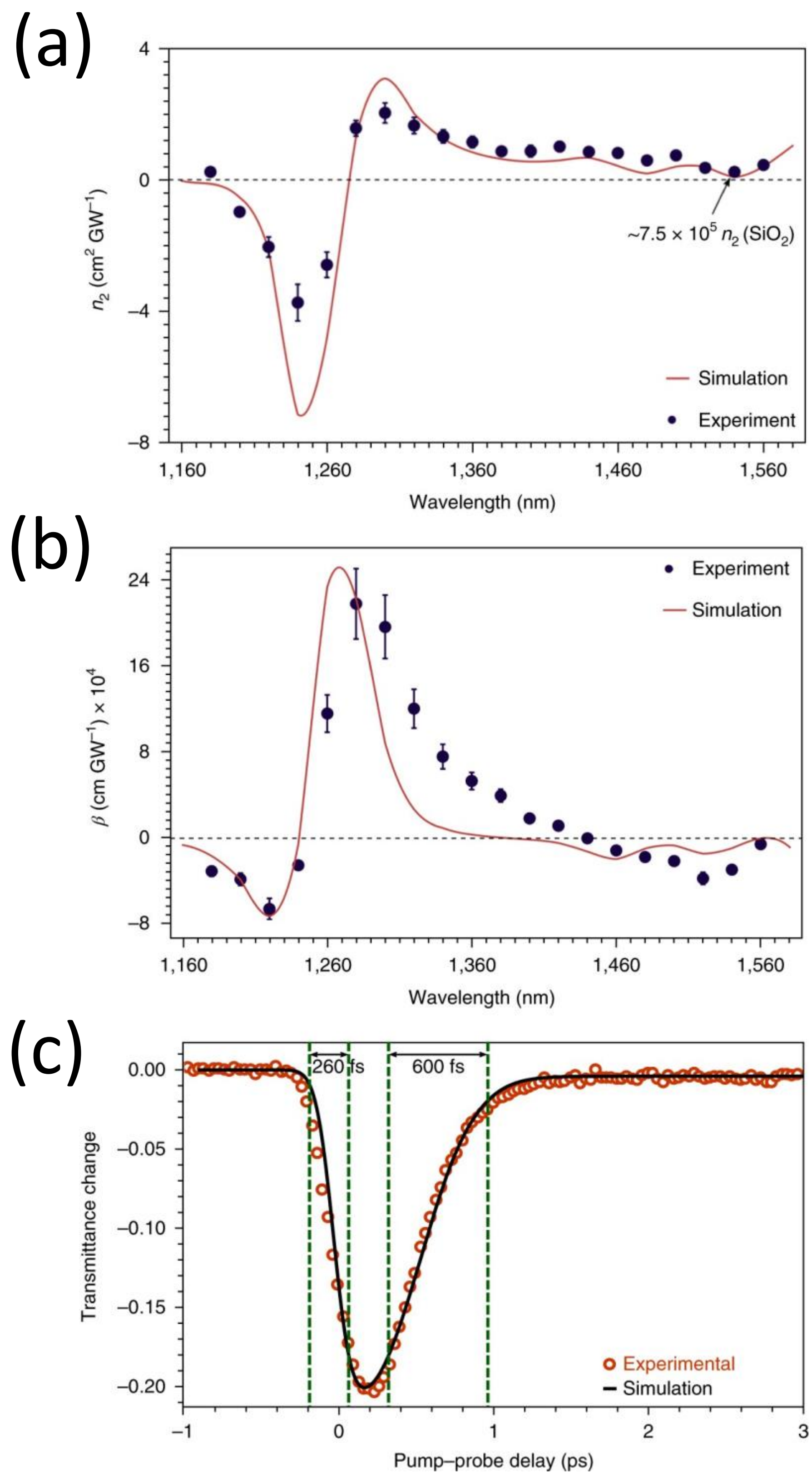

Figure 6: (a) The nonlinear refractive index and (b) the nonlinear absorption coefficient of the sample shown in Figure 5. (c) shows the linear transmittance of light through the sample in simulation and experiment with respect to the time delay between the pump and the probe. All of the Figures are reprinted from reference[9] with permission.

curs at a wavelength near the ENZ point of the ITO layer such that the ENZ mode strongly couples to the electric dipole mode of the metasurface.[24] The ENZ mode is a solution of the electromagnetic wave equations in an ENZ material sandwiched between two dielectric layers when the thickness of the ENZ layer is much less than the wavelength of light. The two important characteristics of this mode are that it is a dark mode, so it is not possible to directly couple into it from free space, and the electric field is hugely enhanced within the ENZ layer when this mode is excited.[25] The presence of the array of plasmonic antennas over ITO can make a bridge from the free space to the ITO to excite the ENZ mode and to further enhance the electric field magnitude within ITO. Figures 6 (a) and (b) show the nonlinear refractive index and the nonlinear absorption coefficient of the sample. We observe that the order of magnitude for n_2 is 10 times larger than the case of a bare 310-nm ITO sample. Figure 6 (c) shows the nonlinear response time of the sample in a pump-probe experiment. One sees that the transmittance of the probe is getting modified in response to the application of a pump beam in a sub-picosecond time scale.

The possibility of modifying the refractive index of ITO with an amount in the same order of magnitude as the linear refractive index in a sub-picosecond time scale makes it a fantastic candidate for all-optical time-varying systems. The main goal of this thesis is to investigate the applications of ITO in different dynamic schemes and their interaction with different types of metasurfaces.

Adiabatic Wavelength Conversion in ITO

An interesting application of the large and fast nonlinear response in ITO is adiabatic wavelength conversion (AWC).[26] In this process, an intense femtosecond (fs) laser pump beam induces the nonlinear response in the system and generates a refractive index response that rises considerably and then falls back to the initial value within a sub-picosecond time duration as in Figure 4 (d). A low-intensity laser probe beam may interact with the time-varying

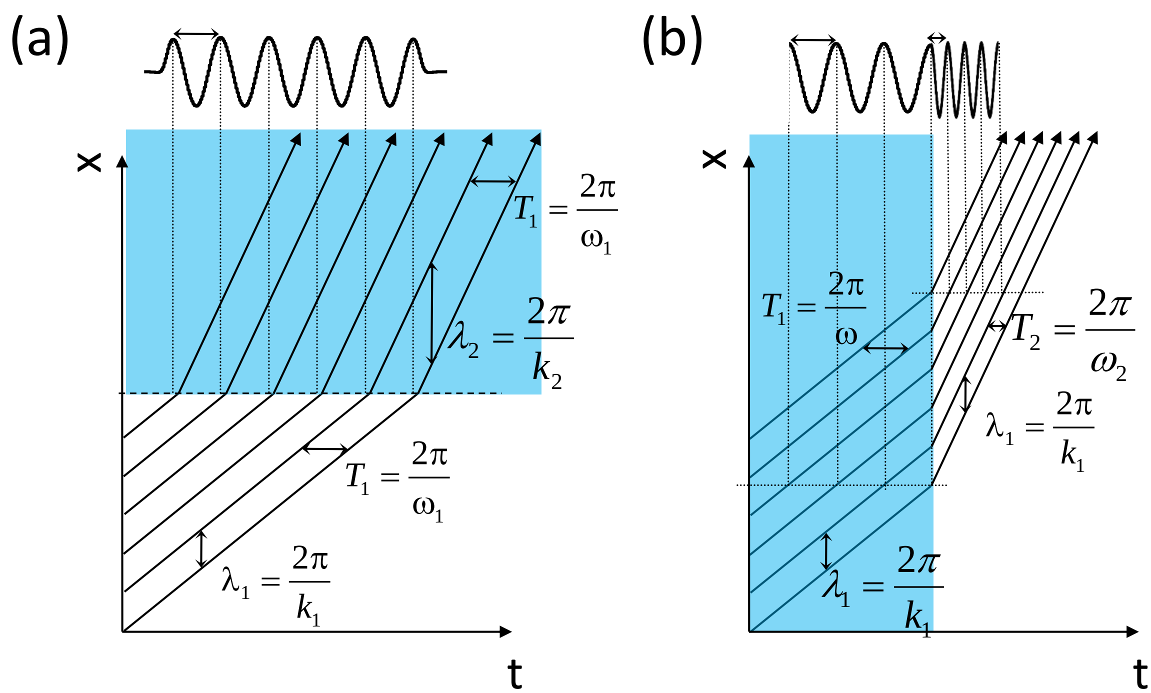

Figure 7: (a) The refraction of a beam of light travelling through the boundary of two regions with different refractive indices. (b) The time refraction of a beam of light travelling in a medium with varying refractive index. Note that the refractive index is larger in the blue material in both cases.

response caused by the pump, and depending on their relative timing, the probe may witness a rising ($\frac{\Delta n}{\Delta t} > 0$) or falling ($\frac{\Delta n}{\Delta t} < 0$) refractive index response, leading to a redshift or blueshift of the probe's wavelength respectively.[26] Since the index rise time is faster, the magnitude of the redshift is larger.

In order to have a better understanding of this phenomenon, we can compare it to the more familiar case of the refraction of light in space. We know that when a beam of light travels through the boundary of two media with different refractive indices, the direction of propagation or, equivalently, the wave vector changes in the second media as in Figure 7 (a). The famous Snell's law can be used to find the new direction of light. Now, assume that the boundary of the refractive index is in time instead of space; so, the medium in which the light is travelling is constant, but the refractive index changes over time. As a result, the wave vector stays constant as there is no boundary in space, but instead, the frequency converts as there is a boundary in time, as in Figure 7 (b).

We discussed this matter in more detail in our paper entitled "Broadband frequency translation through time refraction in an epsilon-near-zero material," which is the second chapter of this thesis. You can also find the supplementary information of the paper in Appendix 1 of the thesis.

All-optical Beam Steering

As mentioned above, the nonlinear response of ITO can be further enhanced if we couple the ENZ mode of ITO to the electric dipole mode of a plasmonic metasurface. This encourages us to combine the ability of metasurfaces in engineering the spacial properties of light with the large and fast time response of ITO to make applicable time-varying metasurfaces that can engineer light in time and space.

In chapter 3 of the thesis, we propose and experimentally investigate an all-optical beam steering device made of a gradient metasurface over ITO. Figures 3 (a) and (b) show simple schematics of a single unit cell of the gradient metasurface we used. The gradient metasurface diffracts the light into different diffraction orders while the angle of diffraction depends on the ratio between the wavelength of light and the lattice size of the metasurface. As a result, if we convert the wavelength of the light using the AWC process in ITO, explained in Chapter 2, the converted wavelengths diffract to new angles. We investigate this phenomenon in our paper entitled "Time-varying gradient metasurface with applications in all-optical beam steering", which is chapter 3 of this thesis. You can also find the supplementary information of the paper in Appendix 2 of the thesis.

Strong coupling between ENZ mode and Mie resonances

Although the interaction of ITO with plasmonic metasurfaces had been investigated, the coupling of the ENZ mode in ITO and the Mie modes in a dielectric metasurface was to be studied when I started my Ph.D. Dielectric metasurfaces are known to have benefits over plasmonic ones; they have much lower absorption loss, and exciting different resonance modes, such as different multi-polar resonances known as Mie modes, are easier in them.

In contrast to plasmonic nanoantennas, the Mie modes of a dielectric nanoantenna exhibit mode volumes that are a few times larger. Thus, the expectation would be that the Mie modes are only perturbatively modified by the presence of an ENZ substrate due to poor modal overlap between the Mie modes and a thin ENZ substrate. In our work in chapter 4 of the thesis, we experimentally and theoretically demonstrate that despite the relatively large mode volume, two fundamental Mie modes (electric and magnetic dipoles) of silicon dielectric antennas can enter into strong coupling regimes with the ENZ mode of a 23-nm-thick ITO substrate.

ITO nano-antennas

In the previous two chapters, we investigated the interaction of ENZ mode in ITO and different types of plasmonic and dielectric nano-antennas and demonstrated the large and fast nonlinear response of such coupled systems. However, nano-antennas made up of ITO can be another building block for all-optical time-varying metasurfaces. In Chapter 5 of the thesis, we propose a numerical method based on recurrence relations for including the nonlinear Kerr effect of the materials with a large nonlinear refractive index that can be implemented in any electromagnetic simulation environment, such as Comsol Multiphysics or Lumerical FDTD. As the next step, we apply the method to extract the scattering pattern of subwavelength ITO nanoantennas in both linear and nonlinear regimes and investigate the possible applications of these nanoantennas.

Additional projects

Aside from the main projects explained in the previous chapters, I contributed to other projects during my Ph.D. I explain the general concept of each project while more discussion about them is provided in the related appendix section.

multi-layer stack ENZ medium

In addition to bulk materials like ITO, whose real part of permittivity vanishes at one specific wavelength, it is also possible to make artificially engineered media that show ENZ properties. One way to do so is to create a multi-layer stack of two materials: with negative permittivity and positive. It has been shown that the effective permittivity of such a stack, assuming the thickness of each layer is much smaller than the wavelength of operation, can be derived as the weighted average of the permittivities of the individual materials.[27]

In the project explained in Appendix 3 of the thesis, we made a multi-layer stack from silver (Ag) and glass (SiO2), with negative and positive permittivities at the visible range of frequency, respectively, that shows ENZ behavior at the wavelengths of around 500 nm. We study its nonlinear behavior using the Z-scan technique and demonstrate that the nonlinear refractive index of the sample peaks around the ENZ point.

Strongly Coupled Plasmon Polaritons in Gold and ENZ Bifilms

It is widely known that surface-bounded electromagnetic modes, known as surface plasmon polaritons, can be excited near metal surfaces. We experimentally investigated the strong coupling of plasmon polaritons with the ENZ mode in a Gold-ITO bi-film. The complete discussion can be found in the paper of Appendix 5 of the thesis.

References

(1) Alam, M. Z.; De Leon, I.; Boyd, R. W. Large optical nonlinearity of indium tin oxide in its epsilon-near-zero region. *Science* **2016**, *352*, 795–797.

(2) Boyd, R. W. *Nonlinear optics*; Academic press, 2020.

(3) Saleh, B. E.; Teich, M. C. *Fundamentals of photonics*; john Wiley & sons, 2019.

(4) Chen, X.; Nadiarynkh, O.; Plotnikov, S.; Campagnola, P. J. Second harmonic generation microscopy for quantitative analysis of collagen fibrillar structure. *Nature protocols* **2012**, *7*, 654–669.

(5) Agrawal, G. P. *Nonlinear Science at the Dawn of the 21st Century*; Springer, 2000; pp 195–211.

(6) Eggleton, B. J. Chalcogenide photonics: fabrication, devices and applications Introduction. *Optics express* **2010**, *18*, 26632–26634.

(7) Weber, M.; Milam, D.; Smith, W. Nonlinear refractive index of glasses and crystals. *Optical Engineering* **1978**, *17*, 463–469.

(8) Vukovic, N.; Healy, N.; Suhailin, F.; Mehta, P.; Day, T.; Badding, J.; Peacock, A. Ultrafast optical control using the Kerr nonlinearity in hydrogenated amorphous silicon microcylindrical resonators. *Scientific reports* **2013**, *3*, 2885.

(9) Alam, M. Z.; Schulz, S. A.; Upham, J.; De Leon, I.; Boyd, R. W. Large optical nonlinearity of nanoantennas coupled to an epsilon-near-zero material. *Nature Photonics* **2018**, *12*, 79–83.

(10) Almeida, V. R.; Barrios, C. A.; Panepucci, R. R.; Lipson, M. All-optical control of light on a silicon chip. *Nature* **2004**, *431*, 1081–1084.

(11) Upham, J.; Tanaka, Y.; Asano, T.; Noda, S. On-the-fly wavelength conversion of photons by dynamic control of photonic waveguides. *Applied physics express* **2010**, *3*, 062001.

(12) Ni, X.; Ishii, S.; Kildishev, A. V.; Shalaev, V. M. Ultra-thin, planar, Babinet-inverted plasmonic metalenses. *Light: Science & Applications* **2013**, *2*, e72–e72.

(13) Zheng, G.; Mühlenbernd, H.; Kenney, M.; Li, G.; Zentgraf, T.; Zhang, S. Metasurface holograms reaching 80% efficiency. *Nature nanotechnology* **2015**, *10*, 308–312.

(14) Bin-Alam, M. S.; Reshef, O.; Mamchur, Y.; Alam, M. Z.; Carlow, G.; Upham, J.; Sullivan, B. T.; Ménard, J.-M.; Huttunen, M. J.; Boyd, R. W., et al. Ultra-high-Q resonances in plasmonic metasurfaces. *Nature communications* **2021**, *12*, 1–8.

(15) Genevet, P.; Yu, N.; Aieta, F.; Lin, J.; Kats, M. A.; Blanchard, R.; Scully, M. O.; Gaburro, Z.; Capasso, F. Ultra-thin plasmonic optical vortex plate based on phase discontinuities. *Applied Physics Letters* **2012**, *100*, 013101.

(16) Kildishev, A. V.; Boltasseva, A.; Shalaev, V. M. Planar Photonics with Metasurfaces. *Science* **2013**, *339*.

(17) Yu, N.; Genevet, P.; Kats, M. A.; Aieta, F.; Tetienne, J.-P.; Capasso, F.; Gaburro, Z. Light propagation with phase discontinuities: generalized laws of reflection and refraction. *Science* **2011**, *334*, 333–337.

(18) Taylor, T. S. *Introduction to laser science and engineering*; CRC Press, 2019.

(19) Agrawal, G. P. *Fiber-optic communication systems*; John Wiley & Sons, 2012.

(20) Benis, S.; Munera, N.; Faryadras, S.; Van Stryland, E. W.; Hagan, D. J. Extremely large nondegenerate nonlinear index and phase shift in epsilon-near-zero materials. *Optical Materials Express* **2022**, *12*, 3856–3871.

(21) Engheta, N.; Ziolkowski, R. W. *Metamaterials: physics and engineering explorations*; John Wiley & Sons, 2006.

(22) Naik, G. V.; Shalaev, V. M.; Boltasseva, A. Alternative plasmonic materials: beyond gold and silver. *Advanced Materials* **2013**, *25*, 3264–3294.

(23) Sheik-Bahae, M.; Said, A. A.; Wei, T.-H.; Hagan, D. J.; Van Stryland, E. W. Sensitive measurement of optical nonlinearities using a single beam. *IEEE journal of quantum electronics* **1990**, *26*, 760–769.

(24) Schulz, S. A.; Tahir, A. A.; Alam, M. Z.; Upham, J.; De Leon, I.; Boyd, R. W. Optical response of dipole antennas on an epsilon-near-zero substrate. *Physical Review A* **2016**, *93*, 063846.

(25) Vassant, S.; Hugonin, J.-P.; Marquier, F.; Greffet, J.-J. Berreman mode and epsilon near zero mode. *Optics express* **2012**, *20*, 23971–23977.

(26) Zhou, Y.; Alam, M. Z.; Karimi, M.; Upham, J.; Reshef, O.; Liu, C.; Willner, A. E.; Boyd, R. W. Broadband frequency translation through time refraction in an epsilon-near-zero material. *Nature Communications* **2020**, *11*, 1–7.

(27) Rytov, S. Electromagnetic properties of a finely stratified medium. *Soviet Physics JEPT* **1956**, *2*, 466–475.

Chapter 2

Broadband frequency translation through time refraction in an epsilon-near-zero material

Contribution Statement

M. Zahirul Alam and I initially discussed this project idea during the first year of my doctoral studies. Our group had demonstrated the large and fast nonlinear optical response of indium-tin-oxide (ITO) but wanted to pursue serious experiments applying this response to time-varying optical systems. The idea was to investigate the effect of the large modification of the ITO refractive index, triggered by an intense optical pump pulse, on an optical probe pulse propagating through the time-varying system. Based on preliminary calculations of the slope of refractive index change with respect to time, we predicted a large (potentially record-breaking) adiabatic wavelength conversion of the probe beam. Yiyu Zhou and I constructed a fully automated pump-probe experimental set-up from scratch to measure adiabatic wavelength conversion in ITO samples. While I had limited optical lab experience at the time, I had experience in automating instruments with Labview; Yiyu Zhou, conversely, was very experienced in optical alignment but had limited experience with Labview. This opportunity taught me how to build sophisticated, multi-beam nonlinear optical experiments. I also learned about the planning and demands around writing highly impacted publications. My contributions to the paper were as follows:

- Building the experimental set-up (1st alongside Yiyu Zhou and Zahirul Alam)
- Automating the set-up (main contributor)
- Performing experiment/data collection (1st alongside Yiyu Zhou)
- Making an analytical model to simulate the system's behaviour (3rd contributor)

nature COMMUNICATIONS

ARTICLE

https://doi.org/10.1038/s41467-020-15682-2 OPEN

Broadband frequency translation through time refraction in an epsilon-near-zero material

Yiyu Zhou[1,4]✉, M. Zahirul Alam[2,4], Mohammad Karimi[2], Jeremy Upham[2], Orad Reshef[2], Cong Liu[3], Alan E. Willner[3] & Robert W. Boyd[1,2]

Space-time duality in paraxial optical wave propagation implies the existence of intriguing effects when light interacts with a material exhibiting two refractive indexes separated by a boundary in time. The direct consequence of such time-refraction effect is a change in the frequency of light while leaving the wavevector unchanged. Here, we experimentally show that the effect of time refraction is significantly enhanced in an epsilon-near-zero (ENZ) medium as a consequence of the optically induced unity-order refractive index change in a sub-picosecond time scale. Specifically, we demonstrate broadband and controllable shift (up to 14.9 THz) in the frequency of a light beam using a time-varying subwavelength-thick indium tin oxide (ITO) film in its ENZ spectral range. Our findings hint at the possibility of designing (3 + 1)D metamaterials by incorporating time-varying bulk ENZ materials, and they present a unique playground to investigate various novel effects in the time domain.

[1] The Institute of Optics, University of Rochester, Rochester, NY 14627, USA. [2] Department of Physics, University of Ottawa, Ottawa, ON K1N 6N5, Canada. [3] Department of Electrical Engineering, University of Southern California, Los Angeles, CA 90089, USA. [4] These authors contributed equally: Yiyu Zhou, M. Zahirul Alam.

Maxwell's equations describe how an electromagnetic wave is modified by a material. The spatial boundary condition associated with Maxwell's equations can be used to derive the well-known Fresnel equations and Snell's law. A spatial variation in refractive index leads to reflection and refraction of a light beam incident on the boundary. As a consequence, the wavevector of the transmitted light changes, whereas the frequency is conserved. The spatial boundary can be abrupt (nonadiabatic) in refractive index variation such as at a glass-air interface. Or, the boundary can be smoothly varying, i.e., adiabatic in space, such as in a gradient-index lens. In both cases, the refracted beam of light must have a different k-vector (Fig. 1a), where $|k| = 2\pi n/\lambda$, n is the refractive index of the medium, and λ is vacuum wavelength of light. As the equations describing the paraxial wave propagation are unchanged upon the interchange of time and a spatial coordinate, one can define a boundary of refractive index in the time coordinate in a dual fashion to that in the spatial coordinates[1–5]. This effect is known as time refraction.

The concept of time refraction is presented in Fig. 1a. Let us assume that an optical pulse of frequency f_1 is traveling in a dispersionless medium with a refractive index of n_1. At $t = t_1$ the refractive index changes from n_1 to n_2. As a consequence of the broken time translation symmetry, the frequency of light has to change because of the change in the refractive index while leaving the wavevector unchanged[6]. The change in frequency, according to the dispersion relation $c/f = n\lambda$[7], can be expressed as $n_1 f_1 = n_2 f_2 = (n_1 + \Delta n)(f_1 + \Delta f)$, where $\Delta f = f_2 - f_1$ is the change in the frequency of light after it encounters the temporal boundary; $\Delta n = n_2 - n_1$ is the change in the refractive index; and c is the speed of light in vacuum. Consequently, we can express the change in frequency as $\Delta f = -\Delta n \cdot f_1/(n_1 + \Delta n)$. Thus, the frequency shift may be red (blue) if the change in index Δn is positive (negative). This effect is strongest when $\Delta n/(n_1 + \Delta n)$ is large. In a regular dielectric medium such as silicon[8], $\Delta n/(n_1 + \Delta n)$ can only be on the order of 10^{-3}. In contrast, in a highly nonlinear low-index medium, $\Delta n/(n_1 + \Delta n)$ can approach unity due to the near-zero linear refractive index n_1 and the large nonlinear index change Δn[9–11]. Thus, a highly nonlinear low-index medium is a natural platform with which to generate a large frequency translation using time refraction. In addition to frequency conversion, a time-varying medium with a large index change can also be used to investigate many novel effects in the time domain such as all-optical nonreciprocity[12,13], negative refraction[14], photonic topological insulators[15], photonic time crystals[16], achromatic optical switches[17], and the dynamic Casimir effect[18].

A number of effects have been used to experimentally implement a time-varying medium, such as free-carrier dispersion[19–24], Kerr nonlinearity[25–28], laser-induced plasma[29–32], and optomechanical interaction[33]. The magnitude of frequency conversion in a time-varying medium fundamentally depends on the available index change. This is in contrast to other nonlinear optical effects such as four-wave mixing[8], where the constraints of weak nonlinearity can be almost entirely overcome through use of a very long interaction length[34]. Resonant structures such as microring resonators and slow-light photonic crystals, tend to exhibit enhanced sensitivity to the change in the material's refractive index. Such resonant structures can be used to somewhat sidestep the restrictions imposed by the intrinsically low nonlinearity of materials to obtain appreciable adiabatic frequency conversion (AFC)[19–22,35–39]. Using these techniques, adiabatic frequency conversions up to 280 GHz (or ~0.145% of the carrier frequency) have been previously demonstrated[20]. Nevertheless, all prior demonstrations of AFC have exhibited the following limitations: narrow operational bandwidth[20,34,38,39]; relatively long interaction length[19,21–25,33,36,37,40]; limited tunability with respect to the magnitude and sign of shift[19–24,40]; the requirement of inhomogeneous structure limiting wide adoptions into various platforms[19–24,33,35–39]; and the possible requirement of out-of-plane above-bandgap excitation pulses[20].

Here, we show that we can simultaneously overcome all of the above-mentioned shortcomings by using a homogeneous and isotropic epsilon-near-zero (ENZ) medium of subwavelength thickness. Using a series of pump-probe measurements, we demonstrate optically controlled total frequency translations of a near-infrared beam of up to 14.9 THz (redshift of 11.1 THz and blueshift of 3.8 THz)—that is, over 6% of the bandwidth of the carrier frequency—using a 620-nm-thick ITO film. The effect of frequency translation is broadband in nature, i.e., the central wavelength of the degenerate input pump and probe pulses can be tuned over a 500 nm range. We also find that the effect is maximum near the zero-permittivity wavelength of ITO.

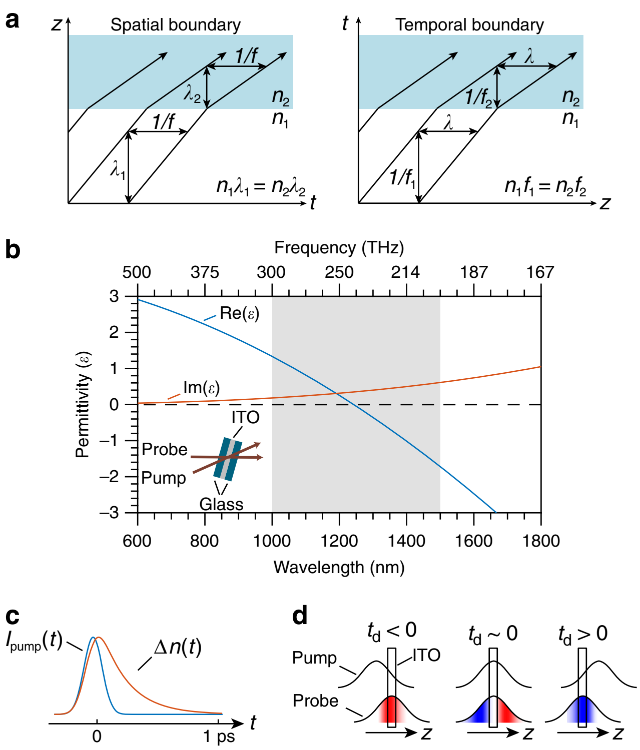

Fig. 1 Concept of time refraction. **a** A spatial boundary defined by a refractive index change from n_1 to n_2 leads to a change in the wavevector of a light beam as it passes through the boundary and is described by $n_1\lambda_1 = n_2\lambda_2$ (left panel). A refractive index boundary defined in time leads to time-refraction effect of a light beam as it passes through the boundary and is described by $n_1 f_1 = n_2 f_2$ (right panel). Here f is the frequency of light waves in the medium. **b** The permittivity of an ITO film used in the experiment. The inset shows the simplified experimental setup and the shaded region shows the spectral range of interest in this work. **c** Simplified illustration of the temporal index change $\Delta n(t)$ of ITO excited by a pump pulse. **d** The frequency of the probe redshifts (blueshifts) if the pump beam lags (leads) the probe. At near-zero delay both redshift and blueshift can occur.

Results

Nonlinear optical response of the ENZ material. An ENZ material is defined as a medium that has a near-zero linear permittivity, and consequently low linear refractive index. The near-zero permittivity in such a medium leads to highly non-intuitive linear effects[41–43] and strong nonlinear light-matter interactions[9,44–47]. In order to implement a temporal boundary with a large index change, we make use of the large and ultrafast optically induced change in refractive index of a 620 nm thick ITO film in its near-zero-permittivity spectral range. ITO is a degenerately doped semiconductor and near its zero-permittivity wavelength (1240 nm), the linear permittivity of the ITO sample can be well described by the Drude model (Fig. 1b). The temporal nonlinear optical response of ITO can be described by the two-temperature model when excited by an optical pulse with a central wavelength close to the ENZ region[9,44]. The optical excitation of ITO near the ENZ region leads to a strong modification of the Fermi-Dirac distribution of the conduction band electrons. The highly nonequilibrium distribution of electrons, within the formalism of the Drude model, leads to an effective redshift of the plasma frequency owing to the momentum-dependent effective mass of the electrons. According to the two-temperature model, the rise time of the change in the refractive index is limited by the thermalization time of the conduction band electrons owing to electron-electron scattering. The rise time also depends on the energy deposition rate in the ITO film and thus has a strong dependence on the temporal envelope of the pump pulse. Once the pump pulse peak leaves the ITO film, the index returns to the initial value within a sub-picosecond time scale through electron–phonon coupling (Fig. 1c). Owing to the time-dependent nature of the index change induced by the intensity of the pump pulse, the frequency of probe pulse can be redshifted or blueshifted depending on the pump-probe delay time (see Fig. 1d).

Measurements at the near-zero-permittivity wavelength. In order to measure the magnitude of the frequency translation using ITO, we performed a set of degenerate pump-probe experiments with ~120 fs pulses and recorded the spectra of the probe beam as a function of the delay between the pump and the probe for varying pump intensities. The ITO film has two 1.1-mm-thick glass slabs on both sides. Both pump and probe beams are p-polarized, and the intensity of the probe beam is kept low to avoid nonlinear effects (See Methods and Supplementary Note 1 for more details). The results for $\lambda_0 = \lambda_{\mathrm{pump}} = \lambda_{\mathrm{probe}} = 1235$ nm at the pump-probe delay time of ±60 fs is shown in Fig. 2. The pump induces a nonlinear change in the refractive index of ITO with a rate that depends on the pump intensity, the temporal envelope of the pump, and the intrinsic nonlinear dynamics of the ITO. When the pump pulse is delayed with respect to the probe, i.e., pump-probe delay time $t_{\mathrm{d}} < 0$, the probe experiences a rising refractive index and thus its spectrum redshifts (Fig. 2a). If the probe reaches the ITO after the peak of the pump pulse is passed ($t_{\mathrm{d}} > 0$), it experiences a falling refractive index change and the spectrum of the probe blueshifts (Fig. 2b). We also note that for $t_{\mathrm{d}} \approx 0$ both blueshift and redshift can occur (Fig. 1d). As the thickness of the ITO film is only 620 nm, 120 fs pump, and the probe pulses never reside entirely within the ITO thin film (Fig. 1d). Thus, the magnitude of the frequency shift of the probe pulse becomes dependent on the index change rate $\Delta n/\Delta t$ it experiences while transiting through the ITO film. We extract the effective values of the index change rate based on the experimental data through numerical simulations (see Supplementary Note 2). In numerical simulation we use the slowly varying envelope approximation and, as a result, the predictions of our model are only dependent on the envelope-averaged dynamics of the ITO.

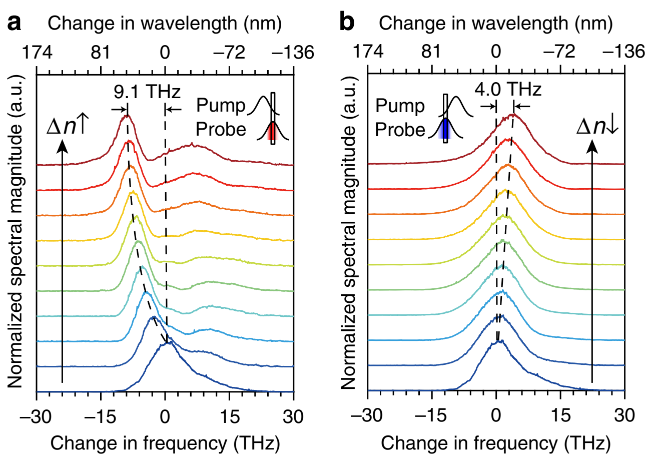

Fig. 2 Pump-induced frequency translation at a fixed delay time. a–b The frequency of a 1235 nm probe beam redshifts at the delay time $t_{\mathrm{d}} = -60$ fs in **a** and blueshifts at the delay time $t_{\mathrm{d}} = 60$ fs in **b**. The insets show the relative position of the pump and the probe. The top-most (bottom-most) spectra in both panels correspond to the largest (zero) pump intensity and, consequently, the largest (zero) change in the refractive index.

We find that both the pump intensity and the value of the pump-probe delay time modify the spectra of the transmitted probe. We present the results for $\lambda_0 = 1235$ nm for three pump intensities in Fig. 3a–c. In general, the time refraction leads to the modification of amplitude, bandwidth, temporal width, and the carrier frequency of the probe pulse (see Supplementary Note 3). In order to focus on the spectral shift, the magnitude of spectrum for each pump-probe delay value is individually normalized in Fig. 3. We find that when the absolute value of the pump-probe delay time $|t_{\mathrm{d}}|$ is increased, the magnitude of the frequency translation for the probe decreases. Furthermore, when pump-probe delays are small, the leading portion of the probe pulse experiences an increase in refractive index (thus redshifts), whereas the trailing portion experiences a decrease of refractive index (thus blueshifts). This is evident in Fig. 3a–c by the presence of two peaks at $t_{\mathrm{d}} \approx 0$. For a fixed pump-probe delay time an increase in pump intensity leads to larger change in index and, as a result, a larger shift in the central frequency of the probe pulse. Furthermore, we find that the fall time of the index change is slower than the rise time of the index change. The fall time of the index change is longer because it—within the formalism of the two-temperature model—is dictated by the intrinsic electron–phonon coupling rate, the maximum temperature of the conduction band electrons, and the thermodynamical properties of the lattice. As a result, the rate of decrease in index after the pump leaves the ITO film is smaller compared with that of the rising edge, and therefore the magnitude of the achievable redshift for a constant pump intensity is larger than the achievable blueshift. At a sufficiently high pump intensity, we observe an appearance of a large blueshifted spectral peak when the pump is at 1235 nm owing to higher-order nonlinear optical effects. At a peak pump intensity of 483 GW cm^{-2} the blueshift can be as large as 10.6 THz (~52 nm in wavelength), and the total maximum frequency translation can be larger than 20 THz (see Supplementary Note 4). This value corresponds to a fractional frequency shift ($\Delta f/f_0$) of ~9%.

We model the time-refraction effect in ITO using the nonlinear Schrödinger equation, and the split-step Fourier method is used to numerically solve the Schrödinger equation[48]. We use an iterative algorithm to calculate the approximate shape of the time-varying nonlinear phase variations induced by the index change to fit the experimentally measured spectra (see Supplementary Note 2). The simulation results are shown in Fig. 3d–f. Our numerical model is in excellent agreement with the experimental data, confirming that the origin of the shift is owing to the rapid change of index experienced by the probe pulse while transiting through the ITO sample.

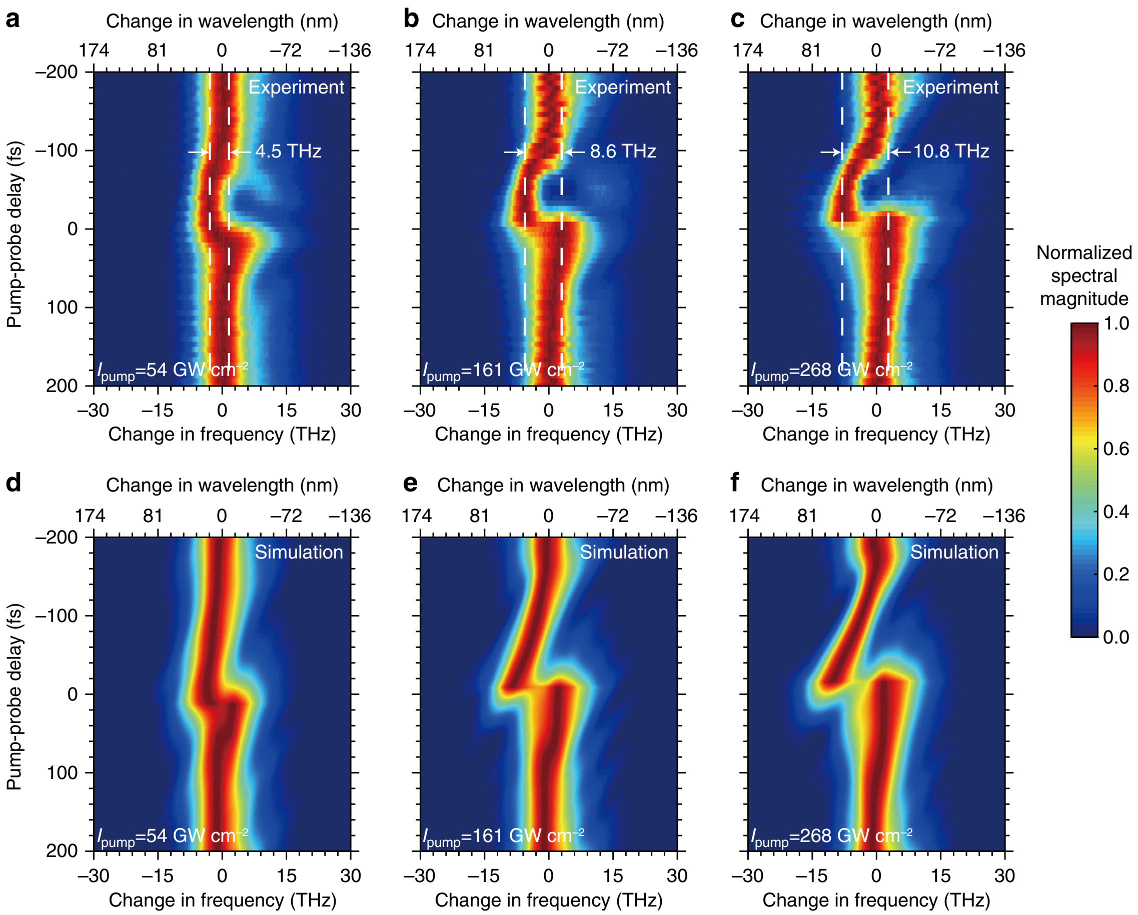

Fig. 3 Experimental and simulated probe spectra at $\lambda_0 = 1235$ nm. a–c Experimental probe spectra as a function of the pump-probe delay time for varying pump intensities. The spectral magnitude for each pump-probe delay is normalized individually. **d–f** The corresponding numerically simulated probe spectra modeled by the nonlinear Schrödinger equation. The spectra of the probe show a strong dependence on the pump intensity and pump-probe delay time. For a pump intensity of 268 GW cm^{-2}, the total frequency translation at this wavelength is 10.8 THz.

Measurements over a broad spectral range. Next, we investigate the dynamics away from the zero-permittivity wavelengths. We repeat the measurements at different excitation wavelengths from $\lambda_0 = 1000$ nm−1500 nm. For each excitation wavelength and pump intensity, we extract the maximum frequency translation of the probe over a range of pump-probe delay time (see Supplementary Note 5). We summarize the wavelength- and intensity-dependent maximum frequency translations in Fig. 4a–e. Here, we limit the pump intensities to avoid the occurrence of significant higher-order nonlinearities. Our results reveal a number of trends. First, both the total achievable frequency translation (redshift and blueshift) and the maximum achievable redshift for a constant pump intensity are the highest near 1235 nm (where $\mathrm{Re}(\varepsilon) \approx 0$) than at other wavelengths. For example, at $\lambda_0 = 1495$ nm the measured maximum magnitude of the redshift (5.4 THz) is a factor of two smaller than what can be achieved at $\lambda_0 = 1235$ nm using a lower pump intensity. Nevertheless, we find that the total maximum fractional frequency translation ($\Delta f/f_0$) at near-zero permittivity is unprecedentedly large (Fig. 4f). The maximum total frequency translation of 14.9 THz (redshift of 11.1 THz and blueshift of 3.8 THz) at $\lambda_0 = 1235$ nm (redshift plus blueshift) is over 53 times larger than what was achieved using a silicon ring resonator of a 6 μm diameter exhibiting a Q-factor greater than 18,000[20]. In contrast, the propagation distance in our material is only 620 nm which is 30 times shorter in physical length and four orders of magnitude smaller than the effective interaction length in a high-Q cavity. Moreover, our results show the operation bandwidth of ITO is much larger than what can be achieved using high-Q resonant structures.

Discussion

As the refractive index of the ENZ material depends on the intensity of the pump, the work presented here may be formally described by cross-phase modulation with a delayed response[8]. However, the concept of time refraction is independent of the source type of the index change (e.g., thermally, optomechanically, or electrically induced index change) and is a more general effect than the simple cross-phase modulation that arises when the temporal boundary is specifically induced by an optical pulse. Furthermore, in contrast to a typical four-wave-mixing-based frequency conversion, the frequency shift obtained through time refraction does not depend on the frequency difference between the pump and the probe and is completely free from phase-mismatching. Although in this work the pump and the probe are frequency degenerate and produced from the same source using a beam splitter, it is not necessary for the beams to be frequency degenerate. Nevertheless, the maximum frequency shift with minimum energy expenditure can be achieved when both the pump and the probe lie within the ENZ spectral range. As the maximum index change happens at the zero-permittivity wavelength, the probe will undergo maximum frequency shift if its wavelength is at or near the zero-permittivity wavelength, whereas the energy expenditure will be

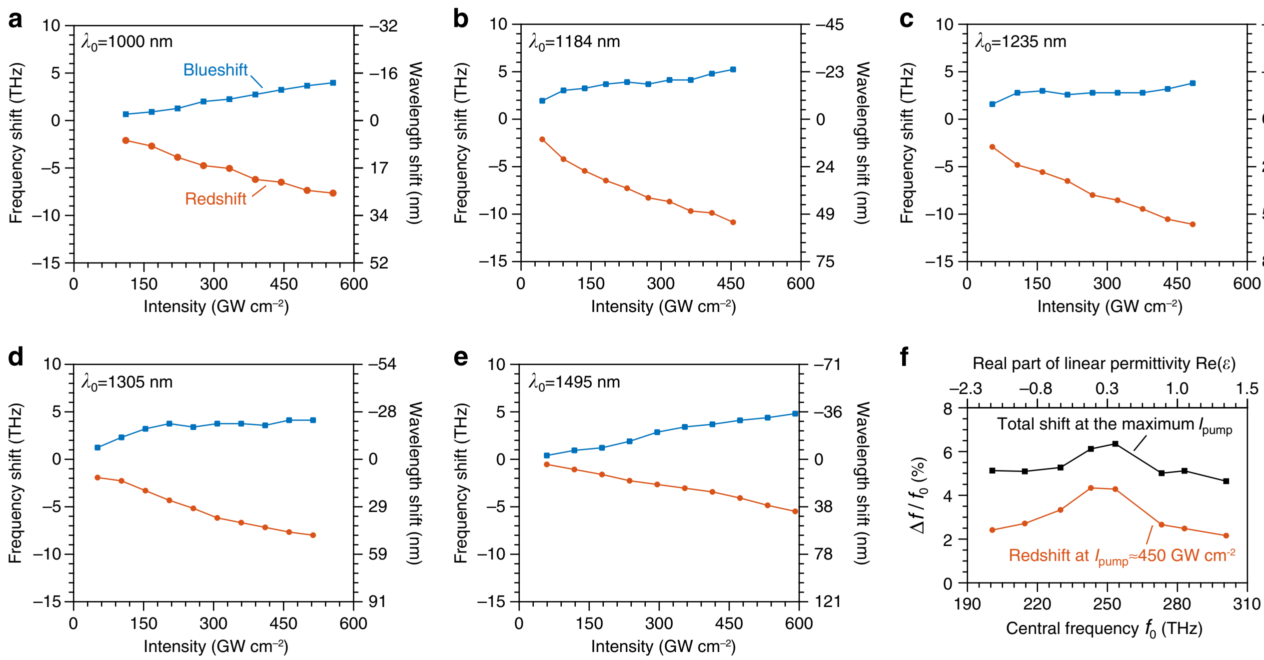

Fig. 4 Wavelength-dependent time-refraction effect. a–e Experimentally measured maximum redshifts and blueshifts at different wavelengths λ_0 as a function of peak pump intensities. **f** The red line denotes the fractional redshift $|\Delta f_{red}|/f_0$ as a function of probe beam's central frequency f_0 at a peak pump intensity ~450 GW cm^{-2}. The real part of the linear permittivity Re(ε) of ITO film at the corresponding central frequency f_0 is shown in the top axis. The black line shows the total fractional shift (redshift plus blueshift) measured at the maximum pump intensities before the onset of higher-order nonlinear optical effects. We find that both the maximum fractional redshift and the total shift occur near the zero-permittivity wavelength.

minimum if the wavelength of pump is also at or near the zero-permittivity wavelength.

In conclusion, we have shown that a subwavelength-thick ITO film can be used to obtain unprecedentedly large (~6.5% of the carrier frequency), broadband and tunable frequency translation. The large time-refraction effect in the ENZ material raises the intriguing possibility of wavelength conversion over an octave using a time-varying ENZ medium. The magnitude of the frequency translation is primarily limited by the linear loss, higher-order nonlinear optical effects, dispersion, and the interplay between the pulse width and the interaction time. We note that the ENZ spectral region of ITO and other conducting oxides can be tuned at any wavelength between 1 μm and 3 μm by choosing the appropriate doping level[49,50]. Furthermore, because the effect is present in a bulk, homogeneous and isotropic material, one can engineer nanostructures incorporating ENZ media such as plasmonic waveguides, photonic crystal waveguides, and dynamic metasurfaces to arbitrarily control the sign and the magnitude of the frequency shift in order to build efficient octave-spanning frequency tuners while simultaneously lowering the required pump power by a few orders of magnitude[9]. For example, an appropriately engineered ITO-based platform can be used to shift an entire band of optical signals in the frequency domain. Such devices may find practical usage in quantum communication protocols requiring conversion of visible photons to infrared[51] and in classical coherent optical communications[52,53]. We anticipate that the large time-refraction effect, we report here, can be exploited to engineer magnet-free nonreciprocal devices[54,55], spatiotemporal metasurfaces[13], and to investigate photonic time crystals and other topological effects in the time domain[16,56] using free-space or on-chip ENZ-based structures.

Methods

Measurements. We use a tunable optical parametric amplifier (OPA) pumped by an amplified Ti:sapphire laser of ~120 fs for the experiments. The output of the OPA is split into two beams to produce the degenerate pump and probe beams using a pellicle beam splitter. Both beams are rendered *p*-polarized. The pump beam is focused onto the sample by a 25 cm lens yielding to a spot size of ~100 μm. The probe beam is focused by a 10 cm lens and its spot diameter is ~45 μm at 1235 nm. Although the spot size can change when the wavelength of the OPA output is adjusted, we always keep the probe beam spot size significantly smaller than the pump beam so that the probe beam experiences a nearly uniform change in the refractive index in the transverse dimensions. The angles of incidences are 15° and 10° for the pump and probe, respectively. The transmitted probe light is coupled to an optical spectrum analyzer via a multimode fiber with a 50 μm core diameter. The commercially available ITO thin film (PGO GmbH) has a thickness of 310 nm and is deposited on a 1.1-mm-thick glass substrate. We sandwich two such ITO films to make the 620 nm thick ITO sample by using a customized sample holder with adjustable tightening screws (See Supplementary Note 6). We use a translation stage to control the delay time between the pump and the probe beams. The experimental setup is presented in Supplementary Note 1.

Data availability

All data supporting this study are available from the corresponding author upon request.

Code availability

All relevant computer codes supporting this study are available from the corresponding author upon request.

Received: 6 March 2020; Accepted: 19 March 2020;
Published online: 01 May 2020

References

1. Akhmanov, S., Sukhorukov, A. & Chirkin, A. Nonstationary phenomena and space-time analogy in nonlinear optics. *Sov. Phys. JETP* **28**, 748–757 (1969).
2. Kolner, B. H. Space-time duality and the theory of temporal imaging. *IEEE J. Quant. Electron* **30**, 1951–1963 (1994).
3. Xiao, Y., Maywar, D. N. & Agrawal, G. P. Reflection and transmission of electromagnetic waves at a temporal boundary. *Opt. Lett.* **39**, 574–577 (2014).
4. Xiao, Y., Agrawal, G. P. & Maywar, D. N. Spectral and temporal changes of optical pulses propagating through time-varying linear media. *Opt. Lett.* **36**, 505–507 (2011).

5. Plansinis, B. W., Donaldson, W. R. & Agrawal, G. P. What is the temporal analog of reflection and refraction of optical beams? *Phys. Rev. Lett.* **115**, 183901 (2015).
6. Mendonça, J., Guerreiro, A. & Martins, A. M. Quantum theory of time refraction. *Phys. Rev. A* **62**, 033805 (2000).
7. Mendonça, J. & Guerreiro, A. Time refraction and the quantum properties of vacuum. *Phys. Rev. A* **72**, 063805 (2005).
8. Boyd, R. W. *Nonlinear optics*. 3rd edn (Elsevier, 2003).
9. Alam, M. Z., Schulz, S. A., Upham, J., De Leon, I. & Boyd, R. W. Large optical nonlinearity of nanoantennas coupled to an epsilon-near-zero material. *Nat. Photonics* **12**, 79–83 (2018).
10. Caspani, L. et al. Enhanced nonlinear refractive index in ε-near-zero materials. *Phys. Rev. Lett.* **116**, 233901 (2016).
11. Reshef, O., De Leon, I., Alam, M. Z. & Boyd, R. W. Nonlinear optical effects in epsilon-near-zero media. *Nat. Rev. Mat.* **4**, 535–551 (2019).
12. Yu, Z. & Fan, S. Complete optical isolation created by indirect interband photonic transitions. *Nat. Photonics* **3**, 91–94 (2009).
13. Shaltout, A. M., Shalaev, V. M. & Brongersma, M. L. Spatiotemporal light control with active metasurfaces. *Science* **364**, eaat3100 (2019).
14. Pendry, J. Time reversal and negative refraction. *Science* **322**, 71–73 (2008).
15. Fang, K., Yu, Z. & Fan, S. Realizing effective magnetic field for photons by controlling the phase of dynamic modulation. *Nat. Photonics* **6**, 782–787 (2012).
16. Lustig, E., Sharabi, Y. & Segev, M. Topological aspects of photonic time crystals. *Optica* **5**, 1390–1395 (2018).
17. Williamson, I. A. & Fan, S. Broadband optical switch based on an achromatic photonic gauge potential in dynamically modulated waveguides. *Phys. Rev. Appl.* **11**, 054035 (2019).
18. Wilson, C. M. et al. Observation of the dynamical casimir effect in a superconducting circuit. *Nature* **479**, 376–379 (2011).
19. Yacomotti, A. M. et al. Nonadiabatic dynamics of the electromagnetic field and charge carriers in high-q photonic crystal resonators. *Phys. Rev. Lett.* **96**, 093901 (2006).
20. Preble, S. F., Xu, Q. & Lipson, M. Changing the colour of light in a silicon resonator. *Nat. Photonics* **1**, 293–296 (2007).
21. Upham, J., Tanaka, Y., Asano, T. & Noda, S. On-the-fly wavelength conversion of photons by dynamic control of photonic waveguides. *Appl. Phys. Express* **3**, 062001 (2010).
22. Kampfrath, T. et al. Ultrafast adiabatic manipulation of slow light in a photonic crystal. *Phys. Rev. A* **81**, 043837 (2010).
23. Castellanos Muñoz, M., Petrov, A. Y. & Eich, M. All-optical on-chip dynamic frequency conversion. *Appl. Phys. Lett.* **101**, 141119 (2012).
24. Kondo, K. & Baba, T. Dynamic wavelength conversion in copropagating slow-light pulses. *Phys. Rev. Lett.* **112**, 223904 (2014).
25. Dekker, R. et al. Ultrafast kerr-induced all-optical wavelength conversion in silicon waveguides using 1.55 μm femtosecond pulses. *Opt. Express* **14**, 8336–8346 (2006).
26. Agrawal, G. P., Baldeck, P. & Alfano, R. Temporal and spectral effects of cross-phase modulation on copropagating ultrashort pulses in optical fibers. *Phys. Rev. A* **40**, 5063–5072 (1989).
27. Li, J., Olsson, B.-E., Karlsson, M. & Andrekson, P. A. Otdm add-drop multiplexer based on xpm-induced wavelength shifting in highly nonlinear fiber. *J. Lightwave Technol.* **23**, 2654–2661 (2005).
28. Mehta, P., Healy, N., Day, T., Badding, J. V. & Peacock, A. Ultrafast wavelength conversion via cross-phase modulation in hydrogenated amorphous silicon optical fibers. *Opt. Express* **20**, 26110–26116 (2012).
29. Bloembergen, N. Laser-induced electric breakdown in solids. *IEEE J. Quant. Electron.* **10**, 375–386 (1974).
30. Yablonovitch, E. Self-phase modulation of light in a laser-breakdown plasma. *Phys. Rev. Lett.* **32**, 1101–1104 (1974).
31. Wood, W. M., Siders, C. & Downer, M. Measurement of femtosecond ionization dynamics of atmospheric density gases by spectral blueshifting. *Phys. Rev. Lett.* **67**, 3523–3526 (1991).
32. Lopes, N. et al. Laser pulse frequency up-shifts by relativistic ionization fronts. *Europhys. Lett.* **66**, 371–377 (2004).
33. Fan, L. et al. Integrated optomechanical single-photon frequency shifter. *Nat. Photonics* **10**, 766–770 (2016).
34. Del'Haye, P. et al. Optical frequency comb generation from a monolithic microresonator. *Nature* **450**, 1214–1217 (2007).
35. Li, Q., Davanço, M. & Srinivasan, K. Efficient and low-noise single-photon-level frequency conversion interfaces using silicon nanophotonics. *Nat. Photonics* **10**, 406–414 (2016).
36. Gaafar, M. A. et al. Reflection from a free carrier front via an intraband indirect photonic transition. *Nat. Commun.* **9**, 1447 (2018).
37. Beggs, D. M., Krauss, T. F., Kuipers, L. & Kampfrath, T. Ultrafast tilting of the dispersion of a photonic crystal and adiabatic spectral compression of light pulses. *Phys. Rev. Lett.* **108**, 033902 (2012).
38. Lee, K. et al. Linear frequency conversion via sudden merging of meta-atoms in time-variant metasurfaces. *Nat. Photonics* **12**, 765–773 (2018).
39. Shcherbakov, M. R. et al. Photon acceleration and tunable broadband harmonics generation in nonlinear time-dependent metasurfaces. *Nat. Commun.* **10**, 1345 (2019).
40. Gaburro, Z. Photonic energy lifters and event horizons with time-dependent dielectric structures. *J. Nanophotonics* **2**, 021853 (2008).
41. Silveirinha, M. & Engheta, N. Tunneling of electromagnetic energy through subwavelength channels and bends using ε-near-zero materials. *Phys. Rev. Lett.* **97**, 157403 (2006).
42. Engheta, N. Pursuing near-zero response. *Science* **340**, 286–287 (2013).
43. Liberal, I. & Engheta, N. Near-zero refractive index photonics. *Nat. Photonics* **11**, 149–158 (2017).
44. Alam, M. Z., De Leon, I. & Boyd, R. W. Large optical nonlinearity of indium tin oxide in its epsilon-near-zero region. *Science* **352**, 795–797 (2016).
45. Kinsey, N. et al. Epsilon-near-zero al-doped zno for ultrafast switching at telecom wavelengths. *Optica* **2**, 616–622 (2015).
46. Ferrera, M. & Carnemolla, E. G. Ultra-fast transient plasmonics using transparent conductive oxides. *J. Optics* **20**, 024007 (2018).
47. Capretti, A., Wang, Y., Engheta, N. & Dal Negro, L. Enhanced third-harmonic generation in si-compatible epsilon-near-zero indium tin oxide nanolayers. *Opt. Lett.* **40**, 1500–1503 (2015).
48. Agrawal, G. P. Nonlinear fiber optics. in *Nonlinear Science at the Dawn of the 21st Century. Lecture Notes in Physics*, Vol. 542 (Springer, 2000).
49. Gui, Y. et al. Towards integrated metatronics: a holistic approach on precise optical and electrical properties of indium tin oxide. *Sci. Rep.* **9**, 1–10 (2019).
50. Yang, Y. et al. Femtosecond optical polarization switching using a cadmium oxide-based perfect absorber. *Nat. Photonics* **11**, 390–395 (2017).
51. Saglamyurek, E. et al. Quantum storage of entangled telecom-wavelength photons in an erbium-doped optical fibre. *Nat. Photonics* **9**, 83–87 (2015).
52. Yanik, M. F. & Fan, S. Stopping light all optically. *Phys. Rev. Lett.* **92**, 083901 (2004).
53. Yoo, S. B. Wavelength conversion technologies for wdm network applications. *J. Lightwave Technol.* **14**, 955–966 (1996).
54. Caloz, C. et al. Electromagnetic nonreciprocity. *Phys. Rev. Appl.* **10**, 047001 (2018).
55. Sounas, D. L., Caloz, C. & Alu, A. Giant non-reciprocity at the subwavelength scale using angular momentum-biased metamaterials. *Nat. Commun.* **4**, 2407 (2013).
56. Giergiel, K., Dauphin, A., Lewenstein, M., Zakrzewski, J. & Sacha, K. Topological time crystals. *N. J. Phys.* **21**, 052003 (2019).
57. Bruno, V. et al. Broad frequency shift of parametric processes in epsilon-near-zero time-varying media. *Appl. Sci.* **10**, 1318 (2020).

Acknowledgements
R.W.B. C.L., Y.Z. and A.E.W. acknowledge support from DARPA (grant No. W911NF-18-0369). O.R. acknowledges the support of the Banting Postdoctoral Fellowship from the Natural Science and Engineering Research Council, Canada. This work was supported by the US Office of Naval Research and the Natural Science and Engineering Research Council, Canada. Note: while our paper was in review, a complementary paper was submitted and published[57]. In contrast to our work, they demonstrate wavelength conversion using four-wave mixing process in a time-varying ENZ thin film.

Author contributions
M.Z.A., J.U., and R.W.B. conceived the work after serendipitous observation of the effect in the laboratory by M.Z.A. M.Z.A. performed the first set of laboratory tests. M.Z.A., Y.Z., O.R., and J.U. designed the experiment. Y.Z. with help from M.Z.A., M.K., O.R., J.U., and C.L. performed laboratory measurements. Y.Z. with help from M.Z.A. performed data analysis and developed the numerical model. Y.Z and M.Z.A. wrote the first draft. All authors contributed to the discussion of the results and the preparation of the final version of the manuscript. A.E.W. and R.W.B. supervised the work.

Competing interests
The authors declare no competing interests.

Additional information
Supplementary information is available for this paper at https://doi.org/10.1038/s41467-020-15682-2.

Correspondence and requests for materials should be addressed to Y.Z.

Peer review information *Nature Communications* thanks the anonymous reviewers for their contribution to the peer review of this work. Peer reviewer reports are available.

Chapter 3

Time-varying gradient metasurface with application in all-optical beam steering

Contribution Statement

During the first year of my doctoral studies, M. Zahirul Alam and I discussed utilizing the significant and rapid nonlinear response exhibited by indium-tin-oxide (ITO) coupled with a plasmonic metasurface. Our objective was to explore the potential of this combination for achieving all-optical beam steering. We initially conceived constructing an array of antennas with varying dimensions or shapes on an ITO layer to create an effective phase ramp across the surface. By operating in the nonlinear regime, we anticipated a change in the effective refractive index of the medium, resulting in a shift in the resonance position of the antennas as a function of wavelength. This shift in resonance would alter the amount of phase accumulation applied to the scattered field at the antenna positions, consequently modifying the slope of the phase ramp as compared to the linear case. Thus, the beam of light would exhibit varying deflection angles in linear and nonlinear scenarios. While this concept was highly motivating, it became apparent that it was not viable in a periodic structure of antennas due to the strong diffraction response of the array overshadowing the optical response of individual unit cells. Additionally, the experimental challenges associated with experimenting on a single unit cell further hindered progress.

After extensive deliberation aimed at circumventing these challenges, we ultimately devised a novel approach that involved combining the adiabatic wavelength conversion effect explored in Chapter 2 with the wavelength-dependent diffraction response of a gradient metasurface. This approach enabled the development of an ultrafast all-optical scheme for beam steering and, more broadly, for light modulation. Alongside revising the main idea, I encountered numerous challenges at various stages of the project. Primarily, I had to determine the optimal shape of the nano-antennas and the degree of design freedom required. Additionally, I needed to choose between designing the sample for reflection or transmission mode. Once these decisions were made, the key challenge involved striking a balance between the diffraction efficiency of the grating and the proximity of the design wavelength to the epsilon-near-zero (ENZ) wavelength to maximize the nonlinear effects. After finalizing different designs and their subsequent characterization, I confronted challenges related to sample fabrication and constructing a pump-probe setup from scratch.

Throughout the experiment, we encountered both expected and unexpected challenges. A predictable challenge arose from our light beams' non-single-frequency nature and finite linewidths, resulting in diffraction patterns that appeared as spread lines rather than single points. This made tracking the beam centers in the pump's presence more difficult and posed challenges when measuring the spectrum. The most significant unexpected challenge was the asymmetric nonlinear response observed in the +1 and -1 diffraction orders. Overcoming this challenge necessitated extensive simulations and discussions to arrive at a satisfactory explanation for this behavior. I extend my gratitude to all of the co-authors who provided guidance and supervision throughout the project, assisting in overcoming these obstacles.

My contributions to the paper were as follows:

- Conception of the project (main contributor)
- Design and simulation of various gradient metasurfaces using both Lumerical FDTD and Comsol Multiphysics (main contributor)
- Fabrication of the samples (main contributor)
- Building the experimental set-up (main contributor)
- Automating the set-up (main contributor)
- Performing experiment/data collection (main contributor)
- Analysing the experimental data (main contributor)
- Writing the first draft of the paper (main contributor)

Research Article

Mohammad Karimi*, M. Zahirul Alam, Jeremy Upham, Orad Reshef and Robert W. Boyd

Time-varying gradient metasurface with applications in all-optical beam steering

https://doi.org/10.1515/nanoph-2022-0756
Received December 12, 2022; accepted March 6, 2023;
published online March 22, 2023

Abstract: Integrating the large, subpicosecond nonlinear optical response of epsilon-near-zero (ENZ) materials with the broad design freedoms of plasmonic metasurfaces shows potential for creating rapidly modulated optical devices with possible applications in telecommunications, sensing, and reactive beam steering. In this work, we experimentally investigate a metasurface consisting of a plasmonic gradient array on a thin layer of indium tin oxide (ITO), characterize how incident probe pulses diffract from a system as it is being dynamically modulated by a pump pulse at wavelengths near the ENZ region. Angular shifts in the diffraction orders are observed and can be principally attributed to the adiabatic wavelength conversion of the probe as it witnesses the temporal change of index induced by the pump. Of note, the asymmetric gradient metasurface, considered to be a blazed diffraction grating, shows significantly different dynamic responses for different diffraction orders. The free-space wavelength shift to +1 and −1 diffraction orders is 6 and 12 nm, resulting in steering angle changes of 0.65 and 1.5°, respectively.

Keywords: epsilon-near-zero (ENZ); metasurface; nonlinear optics.

1 Introduction

Metasurfaces are 2D arrays of subwavelength scattering objects that can be used to control the vectorial properties of electromagnetic radiation [1]. These structures have been used for many different applications, such as in making flat lenses [2], holograms [3], high-quality factor resonators [4], highly nonlinear platforms [5], and vortex beam generators [6]. An important group of metasurfaces is gradient metasurfaces, where the electromagnetic response of the surface is position dependent.

One application of such structures is to control the wave vector direction of the reflected or transmitted wave from the surface, known as anomalous reflection and refraction, respectively [7]. The underlying mechanism for this phenomenon is that the light that scatters from a subwavelength object experiences some phase shift that depends on the spectral separation between the incident beam's central wavelength and the object's resonance wavelength. If we prepare an array of differently sized scatterers that, as a result, have different resonance wavelengths, the incoming field experiences a position-dependent phase shift at the surface. This position-dependent phase shift produces an additional transverse k-vector, which consequently leads to an altered deflection angle of the scattered field. In the case of a periodic pattern of differently sized antennas, the metasurface will behave very similar to a grating that diffracts the incident light into different diffraction orders (DOs). The angle of diffraction for the first DOs, DO = +1 or −1, is determined by the ratio between the wavelength and the lattice size (Λ) through the equation

$$\sin\left(\theta_t^{\pm 1}\right) = \sin\left(\theta_r^{\pm 1}\right) = \pm\frac{\lambda_0}{\Lambda}. \tag{1}$$

The portion of the incident power that couples into each diffraction order at each wavelength depends on the phase distribution over each unit cell [8].

A challenge that has attracted much attention in recent years is how to make time-varying metasurfaces that dynamically control the vectorial properties of scattered light [9–14]. To this end, the metasurfaces are typically embedded within some host medium with optical properties that can be controlled dynamically. Many different host media have been proposed for this purpose, such as mechanically elastic materials [10], liquid crystals [11], phase-change materials [12], semiconductors [13], and transparent conduction oxides (TCOs) [14]. Among these media, elastic materials, liquid crystals, and phase-change materials provide comparatively slower mechanisms with response times in the order of milliseconds or longer [10–12]. One can have much faster control over the optical characteristics of the system by applying a voltage through a gate to the host media made of semiconductors or TCOs and manipulating the electron distribution within these materials [13, 14]. This method, although providing the possibility of microsecond control over the system, requires connecting subwavelength scattering objects to external voltage sources, which may lead to design limitations and fabrication complications. Also, in metasurfaces that are dynamically controlled by an external voltage, the nanoantennas themselves are usually playing the role of the gate, which limits the application of this method to metallic metasurfaces.

To achieve high-speed control over the optical characteristics of a system and to also create an environment to engineer the phase profile of the surface, one may find it useful to design an all-optically controlled scheme to manipulate the optical properties of the system. This would require that a material with high nonlinear optical responses host the metasurface. Incorporating such material would enable changes to the optical properties of the system by applying a pump field of sufficient intensity to trigger the nonlinear response of the host medium.

Indium tin oxide is a TCO with a permittivity that follows the Drude model in the infrared (IR) region [15]. The real part of ITO permittivity vanishes at a wavelength in the IR range called the ENZ point [15]. When illuminating a thin layer of ITO with a sufficiently intense laser pulse, the electrons undergo an intraband energy level transition in a subpicosecond time scale, leading to a large and fast refractive index modification of ITO. Thin films (310 nm) of ITO are known to possess one of the largest ultrafast nonlinear refractive indices among solid materials [16]. This nonlinear response can be enhanced further when the ENZ mode within the ITO layer couples to the electric dipole resonance of an array of plasmonic nanoantennas [5]. This enhancement will occur when the resonance wavelength of the antennas is close to the ENZ point of the ITO layer such that the ENZ mode strongly couples to the electric dipole mode of the metasurface [17].

An exciting application of the large and fast nonlinear response in ITO, or the coupled system of ITO and a plasmonic metasurface, is adiabatic wavelength conversion (AWC) [18]. In this process, an intense pulsed laser pump beam induces a nonlinear response in the system, generating a refractive index change that rises considerably and then falls back to the initial value within a subpicosecond time duration. A low-intensity laser probe beam may interact with the time-varying response caused by the pump and depending on their relative timing, the probe may observe a rising $\left(\frac{\Delta n}{\Delta t} > 0\right)$ or falling $\left(\frac{\Delta n}{\Delta t} < 0\right)$ refractive index response, leading to a red-shift or blue-shift of the probe's wavelength, respectively [18]. Since the index rise time is shorter, the magnitude of the red-shift is larger.

Our goal has been to design and fabricate a gradient metasurface with gold nanoantennas over a thin layer of ITO to optically manipulate the light diffracted by the metasurface. The device is tested in a pump-probe setup providing a system for the all-optical control of the spectral and vectorial distribution of the probe beam DOs. For an appropriate time delay between the pump and the probe, the free-space wavelength of the diffracted beam would be shifted and so the deflection angle for DO $= \pm 1$ will change based on Eq. (1) and its following discussion. This system can be considered to be an all-optical beam steering device.

2 Metasurface design

We designed the metasurface as a repeating group of nanoantennas of different lengths to provide an overall response akin to a blazed diffraction grating while ensuring that each antenna showed good coupling to the ITO substrate. This requirement considers both the dimensions of each antenna in a unit cell and the properties of the ITO substrate.

The selected ITO thickness (65 nm) has an ENZ mode that can couple to electric dipole resonance modes of the nanoantennas and provides the best trade-off between the diffraction efficiency and the strength of the nonlinear response. The ENZ mode is a naturally dark mode that exists in very thin layers of ENZ material sandwiched between two dielectrics [19]. The ENZ point for our ITO layer is 1360 nm (Figure S1 of the supplementary information). The value of the imaginary part of the permittivity of ITO at the zero-permittivity wavelength of 1360 nm is 0.35. Thus, the 65-nm-thick ITO films considered in this work have a non-negligible absorption loss of around 20% in our wavelength range of interest. We require that the electric dipole moment of each antenna resonate near the zero-permittivity wavelength while also differing from the resonance wavelength of the adjacent nanoantennas. Therefore, all the dipole moments couple to the ENZ mode of the ITO substrate efficiently while contributing to creating the gradient metasurface. The wavelength of the peak of the ENZ mode may be found by solving the wave equation in the thin ENZ layer sandwiched between a glass substrate and air superstrate

[19]. That wavelength can be slightly different from the ENZ wavelength, but this does not affect our design procedure.

Each unit cell consists of four antennas with identical widths but different lengths. To select the lengths of the antennas, we simulated uniform metasurfaces made of identical antennas using the finite difference time domain (FDTD) method and after sweeping over the length of the antennas, recorded the phase of the reflected and transmitted field for each length. Since the antennas exhibit a broader range of phases in reflection than in transmission, we designed our metasurface to apply the largest linear phase ramp over a unit cell on the reflected field. The distance between adjacent antennas (344 nm) is sufficient to neglect the coupling between neighboring antennas, which is essential in our design as we require the resonance behavior of individual antennas to be the same in the final gradient metasurface as it would be in a uniform metasurface. The number of antennas in each unit cell makes the unit cell size slightly larger than the wavelength of interest, thus maximizing the steering angle of the 1st DOs in response to wavelength conversion (see Eq. (1)), as explained in the following.

Figure 1(a) shows the phase of the reflected field from a metasurface of homogeneous antennas of constant thickness and width but different lengths across different wavelengths simulated by Ansys Lumerical's FDTD software. The maximum phase ramp for a wavelength around the ENZ point is at an operating wavelength of 1300 nm. The black dots indicate the lengths of the nanoantennas selected for the final gradient metasurface such that they provide the maximum phase ramp on the reflected field over each unit cell. Figure 1(b) represents the schematics of the designed structure. Four antennas of thickness = 50 nm, width = 100 nm, and lengths = 440, 330, 270, and 100 nm were selected to make a unit cell of size 1375 nm by 600 nm for the final design. With the selected lattice size, ± 1 DOs deflect to an angle of $\theta = 71°$ (as in Figure 1(c)) under normal incidence of the incident beam, as can be derived using Eq. (1). Figure 1(d) shows the angular dispersion of the DOs of reflection for the gradient

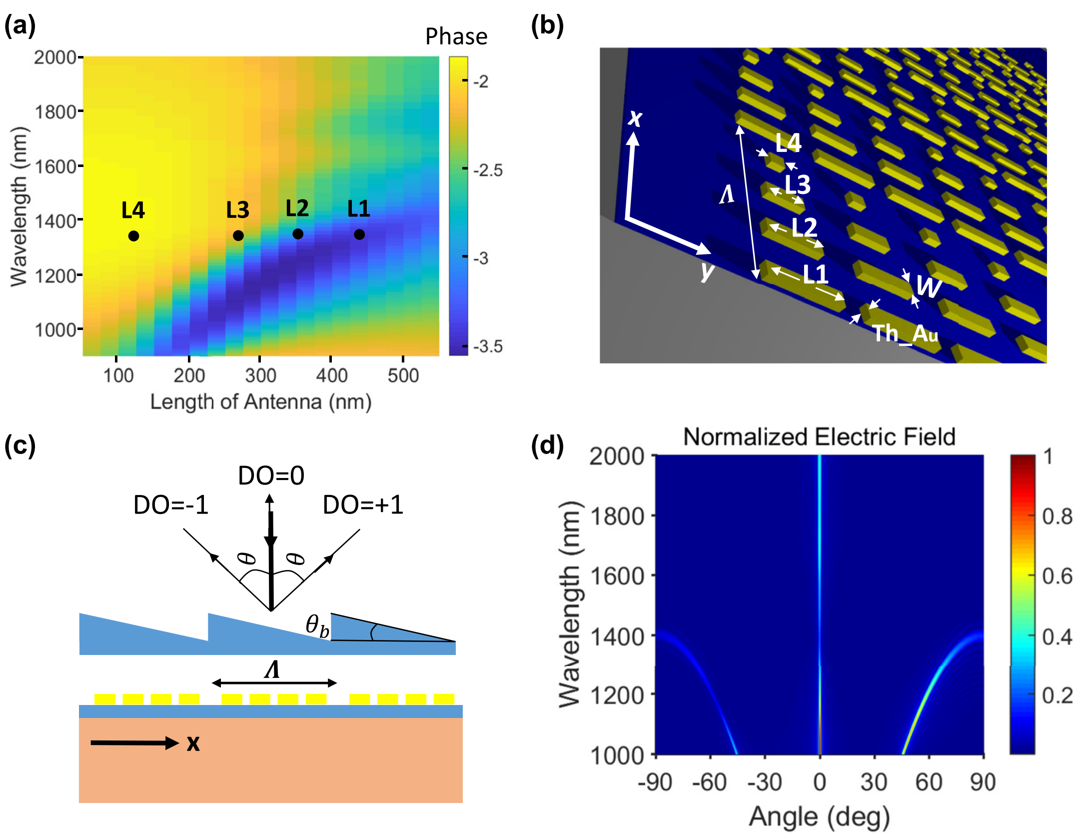

Figure 1: The design procedure of the plasmonic metasurface. (a) The phase of the reflected field from a metasurface of homogeneous gold antennas of a constant thickness (50 nm) and width (90 nm). The four selected lengths (L1 to L4) are indicated with black dots. (b) 3D schematic of the final design of the device; the dimensions in the figure are L1 = 420 nm, L2 = 330 nm, L3 = 270 nm, and L4 = 100 nm. The period along the gradient is $\Lambda = 1375$ nm, and the separation between rows is $P = 600$ nm. (c) Schematic demonstrating the similarity of a periodic gradient metasurface and a blazed grating. (d) FDTD simulation of the angular distribution of the +1, 0, and −1 DOs of reflection at different wavelengths.

metasurface. The metasurface primarily diffracts light toward the +1 DO as it is a blazed grating. However, the metasurface also diffracts a non-negligible amount of power in the −1 DO direction primarily due to phase and digitization errors introduced by the antennas.

3 Results and discussion

Device fabrication used a standard lift-off process on a sample of 65-nm-thick ITO on glass. Two layers of PMMA with different molecular weights, 495PMMA and 950PMMA, were spun over the sample as the bottom and the top resist layers, respectively. The layout of the metasurface was then written into the resist using electron beam lithography followed by a development of the sample in MIBK/IPA 1:3. A 27-nm-thick gold layer was then evaporated onto the sample using a thermal source. Finally, the excess gold over the resist lifted off the sample after laying inside 70 °C acetone overnight. Figure 2(a) shows an SEM image of the final fabricated device. We used a degenerate pump-probe setup to test the sample. The pump and probe pulses are 120 fs in duration with a repetition rate of 1 KHz, generated together by a tunable optical parametric amplifier driven by a Ti:sapphire source and then split and routed to the metasurface, as shown (Figure 2(b)). The probe illuminates the sample from the ITO side at normal incidence and a constant, low intensity of 100 MW/cm^2. The reflectance of the pump from the metasurface increases with increasing angles of incidence (Figure S3). Thus, to avoid large reflectance of the pump, we choose a small (5°) angle of incidence, which appear to produce the best response.

We could distinguish DO $= \pm 1$ of the probe in reflection and transmission. While our measurements focus on the reflected DOs, we observed similar responses for the transmitted DOs. We placed an observing screen in the path of each of the DOs and then imaged the screen onto an IR camera. We repeated this procedure for DO $= \pm 1$ as a function of the time delay between the pump and the probe.

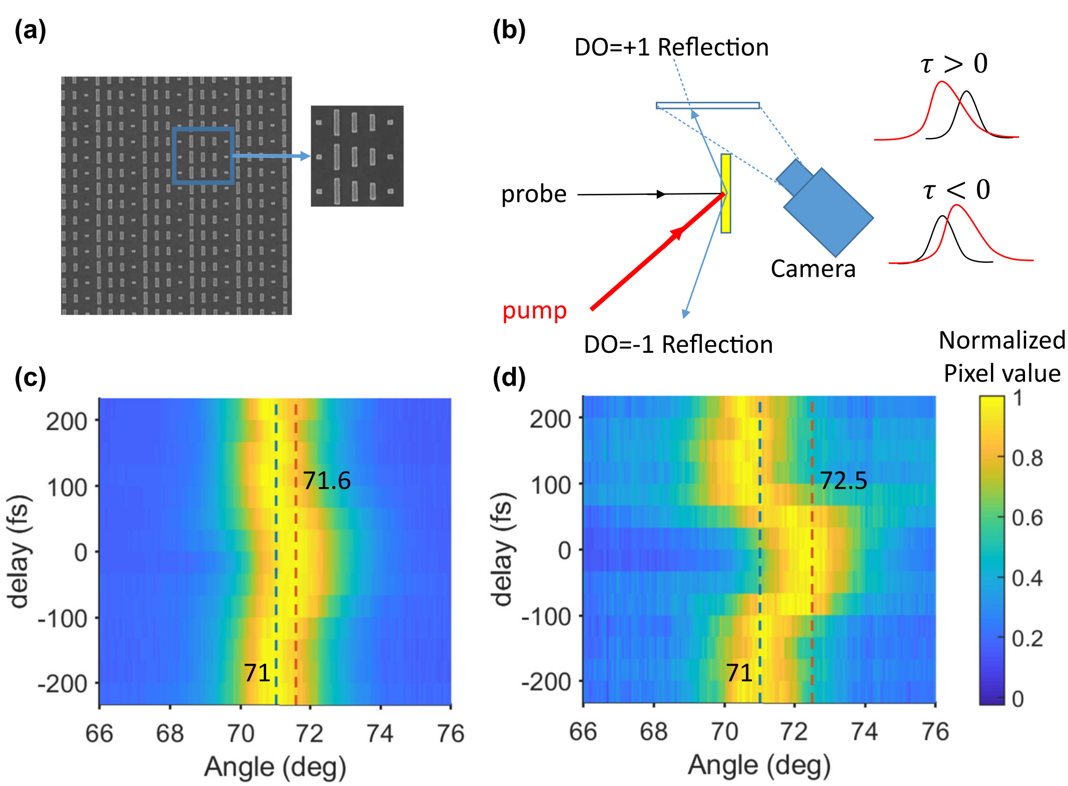

Figure 2: Fabrication and characterization of the sample. (a) The SEM image of the fabricated device. (b) A simple schematic of the pump-probe set-up with a camera to image the diffracted beams at different time delays between the pump and the probe. (c) and (d) The angular distribution of DO = +1 and DO = −1 of the probe, respectively, at different time delays between the pump and the probe. The power of each row (each delay) is normalized to the brightest pixel in that row.

Figure 2(c) and (d) show the angular distribution of the power of DO = ±1 for different time delays between the pump and the probe. A negative time delay means that the probe precedes the pump. The central wavelength of the incident light is 1300 nm, and the intensity of the pump is 14 GW/cm^2. The results for different wavelengths and intensities will be presented and discussed later. We see that the DO power is distributed around a central angle of 71°. When the pump and the probe overlap in time, the diffraction angles of the DOs change. The maximum steering occurs at a negative time delay of −33 fs.

Of particular interest is the surprising result that the magnitude of steering is 0.6° for DO = +1 and 1.5° for DO = −1, suggesting that these two diffraction orders respond significantly differently to the temporal change of the refractive index. This asymmetric response was not anticipated but is consistent and repeatable. It could not be readily explained by asymmetries of the characterization stage; while the pump beam illuminates the sample at an angle, switching between the DO = +1 and −1 sides by loading the sample upside down or interchanging the pump and the probe beams produced the same asymmetric nonlinear behavior of the DOs. This asymmetry of steering response was also consistent across separately fabricated metasurfaces, as long as they followed this same design. Similarly, the difference in response holds for different input powers and wavelengths. Therefore, for this metasurface design, the DO = −1 diffraction order shows a consistent steering response that is roughly twice as large as its DO = +1 counterpart.

Having dismissed these other possible causes for this asymmetric response in beam steering, we are left to conclude that it is caused by the asymmetry of the metasurface itself, which is to say, the blazing angle imposed by the asymmetry of the nanoantenna placement within each unit cell of the metasurface. One possible explanation is that because the blazing frustrates the coupling of the probe light to the −1 diffraction mode through built-up interference of the different nanoantennas, light that does ultimately couple to this less preferred mode has spent more time in the metasurface compared to light diffracting in the DO = +1 mode. If so, it would consequently have witnessed more of the temporal change of refractive index induced by the pump. Should this be the case, we would predict that the light diffracted to the DO = −1 mode would have not only a larger change in angle but also a larger change in the spectrum as this mode has undergoes a greater degree of AWC by the pump. Also, to compare the interaction time of different DOs with the metasurface and confirm the longer interaction time of DO = −1, we extracted the phase accumulated by each diffraction order over the interaction with the metasurface from the Comsol Multiphysics simulation of the device in the linear regime. Figure S5 in the supplementary shows this phase for different reflected DOs and demonstrates that the phase accumulation over the metasurface for DO = −1 is almost two times larger than that of DO = +1 in our wavelength range of interest. This phase accumulation suggests that DO=−1 has a longer interaction time with the metasurface. It is also noteworthy that a similar asymmetric nonlinear response of different scattering modes in ENZ media has also been reported by Bruno et al. [20].

In order to confirm that AWC is the principal mechanism for the steering of the beam, we measured the spectrum of different portions of the beams that diffracted to different angles with respect to the time delay between the pump and the probe. Figure 3 demonstrates the wavelength

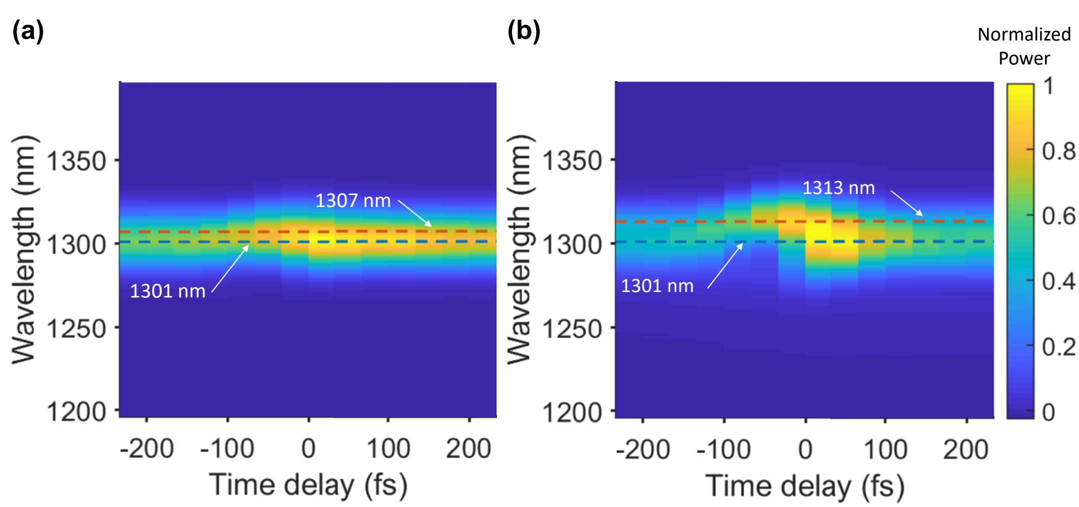

Figure 3: The spectral distribution of the (a) DO = +1 and (b) DO = −1 for different time delays between the pump and the probe. Here power is normalized to the brightest value in the whole graph.

distribution of DO = ±1 for the incident-field central wavelength of 1300 nm at a constant 14 GW/cm^2 pump intensity and for different time delays between the pump and the probe. In order to create this graph, we measured the spectra of DO = ±1 separately for different diffraction angles and then integrated the data over these angles to create a 1D wavelength-dependent data for each time delay. The largest wavelength shift happened for the delay time of −33 fs and was 6 nm for DO = +1 and 12 nm for DO = −1. These magnitudes of wavelength conversion reflect the proportional changes to the steering angles of 0.8 and 1.6° using Eq. (1) for DO = +1 and DO = −1, respectively, and are in good agreement with the camera data discussed above.

We also investigated the effect of the pump power on the steering angle of the DOs of the probe. Figure 4(a) and (b) show the maximum steering angle for the incident field central wavelength of 1300 nm at different pump intensities. The steering angle increases with intensity for up to 14 GW/cm^2 and then starts to saturate. This saturation can be attributed to the limited capacity of the upper levels in the conduction band of ITO that limits the intraband transitions, which are the primary source of nonlinearity in ITO [16]. The damage threshold of our sample is approximately 20 GW/cm^2 and is dictated by that of the gold nanoantennas. This value is consistent with previous reports [21]. Note that the asymmetry between DO = +1 and DO = −1 is observable in all powers of the pump.

It is crucial to study the response of the device at different wavelengths. This can be investigated in two different regimes: linear and nonlinear. The linear response of the antennas has wavelength dependence, so the phase ramp over each unit cell will be modified, as will the distribution of power that couples into the DOs. Similarly, the

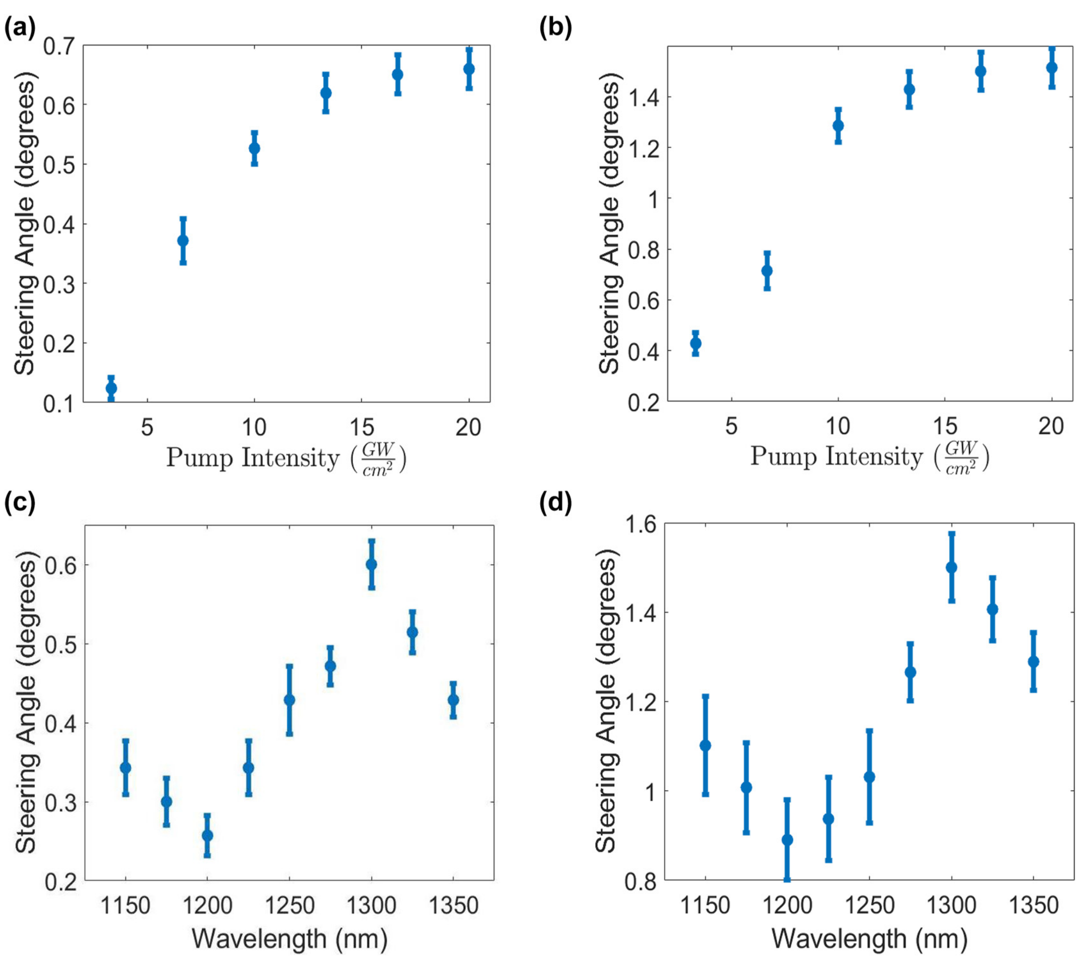

Figure 4: The maximum steering angle at different incident wavelengths and powers. (a) and (b) Show the maximum steering angle of DO = +1 and DO = −1, respectively, at different pump intensities for an incident central wavelength of 1300 nm. (c) and (d) Show the maximum steering angle of DO = +1 and DO = −1, respectively, for different wavelengths of the incident beams while the intensity of the pump is kept constant at 14 GW/cm^2.

nonlinear response is also wavelength dependent, as we expect a larger nonlinear response when we are near the resonance wavelength of at least one of the antennas. The closer and stronger the resonance, the larger the confinement of light in the nonlinear substrate. As a result, the spectral response of the device is mainly influenced by the resonance properties of the nanoantennas. Figure 4(c) and (d) show the maximum steering angles for different central wavelengths of the incident field while the pump power is kept constant. The maximum steering angle for both DOs happens at a probe central wavelength of 1300 nm. While the maximum nonlinearity for a bare sample of ITO occurs around the ENZ wavelength, when we place nanoplasmonic antennas on top of the ITO, the maximum nonlinearity wavelength blue-shifts [5]. One observes that the asymmetric response of DO = +1 and DO = −1 holds for all wavelengths measured.

Going forward from this proof-of-principle experiment, there are a few design approaches to increase the observed angular shifts. First, the observed angular shift's magnitude is proportional to the wavelength change's magnitude, so increasing the achievable AWC can be considered. Larger AWC has been reported [18] in an ENZ material and could be presumably improved by increasing the interaction time between the probe and metasurface during the latter's nonlinear response to the pump. Second, this metasurface was designed for a large phase ramp across the unit cell to maximize the diffraction efficiency in the linear regime rather than to produce optimal coupling to the ENZ material. As a consequence, some of the antennas resonate away from the ENZ wavelength and will have reduced nonlinear enhancement. Designing for a different trade-off between the power coupling efficiency and the strength of the nonlinear response could increase the AWC and thus the angular swing. Third, if the metasurface incorporated a back-reflecting plane below the ENZ material, it would likely improve both the nonlinear phase shift and the power coupling efficiency, thus increasing the range of angular shift.

In conclusion, we propose an all-optical scheme to make a dynamic gradient metasurface using the large and subpicosecond nonlinear response of ITO around its ENZ wavelength. We designed a periodic gradient plasmonic metasurface consisting of an array of gold nanoantennas over a 65-nm ITO layer. The incident light diffracted as expected to different DOs in both reflection and transmission with the diffraction angle dependent on the free-space wavelength and the periodicity of the array. We induced the large, fast nonlinear response of the ITO-based metasurface, leading to adiabatic wavelength conversion (AWC) of the diffracting beam, and the converted wavelengths diffracted to new angles. In other words, this scheme uses an optically pumped AWC effect to steer the DOs of a light beam to different angles. This effect was studied in detail for the reflected DOs, but similar responses are achievable in transmission.

The maximum amount of wavelength conversion and steering angle was different for the cases of DO = +1 and DO = −1. A question that remains is whether the asymmetry of the metasurface which produce asymmetry in the frequency shift and thus also the magnitude of beam steering is a designable parameter. For instance, how would the relative magnitude of the shift of these two diffraction orders change with blazing angle? Would the relative magnitude of shift be proportional to the relative diffraction efficiency of these two diffraction orders? Finally, how would this asymmetry DO behave for higher order (2nd, 3rd) diffraction modes? These questions all require the design, fabrication, and characterization of new asymmetric metasurfaces and are, therefore, beyond the scope of this report but may be an intriguing avenue for further study.

Finally, the scheme for dynamic control of light scattering from a metasurface is entirely compatible with metasurfaces of different antenna shapes or different materials, including dielectrics. Hence, opportunities exist to expand functionality via holography or explore different wavelength ranges.

Acknowledgment: The authors acknowledge support from the Canada Research Chairs (CRC) Program, and the Natural Sciences and the Innovation for Defence Excellence and Security (IDEaS) Program of the Department of National Defence. RWB acknowledges support through US DARPA award W911NF-18-1-0369, US ARO award W911NF-18-1-0337, US Office of Naval Research MURI award N00014-20-1-2558, US National Science Foundation Award 2138174, and a DOE award.
Author contributions: All the authors have accepted responsibility for the entire content of this submitted manuscript and approved submission.
Research funding: None declared.
Conflict of interest statement: The authors declare no conflicts of interest regarding this article.

References

[1] A. V. Kildishev, A. Boltasseva, and V. M. Shalaev, "Planar photonics with metasurfaces," *Science*, vol. 339, no. 6125, pp. 1232009-1—1232009-6, 2013.

[2] X. Ni, S. Ishii, A. V. Kildishev, and V. M. Shalaev, “Ultra-thin, planar, babinet-inverted plasmonic metalenses,” *Light: Sci. Appl.*, vol. 2, no. 4, p. e72, 2013.
[3] G. Zheng, H. Mühlenbernd, M. Kenney, G. Li, T. Zentgraf, and S. Zhang, “Metasurface holograms reaching 80% efficiency,” *Nat. Nanotechnol.*, vol. 10, no. 4, pp. 308—312, 2015.
[4] M. S. Bin-Alam, O. Reshef, Y. Mamchur, et al., “Ultra-high-q resonances in plasmonic metasurfaces,” *Nat. Commun.*, vol. 12, no. 1, pp. 1—8, 2021.
[5] M. Z. Alam, S. A. Schulz, J. Upham, I. De Leon, and R. W. Boyd, “Large optical nonlinearity of nanoantennas coupled to an epsilon-near-zero material,” *Nat. Photonics*, vol. 12, no. 2, pp. 79—83, 2018.
[6] P. Genevet, N. Yu, F. Aieta, et al., “Ultra-thin plasmonic optical vortex plate based on phase discontinuities,” *Appl. Phys. Lett.*, vol. 100, no. 1, p. 013101, 2012.
[7] N. Yu, P. Genevet, M. A. Kats, et al., “Light propagation with phase discontinuities: generalized laws of reflection and refraction,” *Science*, vol. 334, no. 6054, pp. 333—337, 2011.
[8] B. D. Guenther and D. Steel, *Encyclopedia of Modern Optics*, Cambridge, Massachusetts, Academic Press, 2018.
[9] A. M. Shaltout, V. M. Shalaev, and M. L. Brongersma, “Spatiotemporal light control with active metasurfaces,” *Science*, vol. 364, no. 6441, p. eaat3100-1—eaat3100-10, 2019.
[10] S. M. Kamali, E. Arbabi, A. Arbabi, Y. Horie, and A. Faraon, “Highly tunable elastic dielectric metasurface lenses,” *Laser Photon. Rev.*, vol. 10, no. 6, pp. 1002—1008, 2016.
[11] A. Komar, R. Paniagua-Dominguez, A. Miroshnichenko, et al., “Dynamic beam switching by liquid crystal tunable dielectric metasurfaces,” *ACS Photonics*, vol. 5, no. 5, pp. 1742—1748, 2018.
[12] Y. Kim, P. C. Wu, R. Sokhoyan, et al., “Phase modulation with electrically tunable vanadium dioxide phase-change metasurfaces,” *Nano Lett.*, vol. 19, no. 6, pp. 3961—3968, 2019.
[13] Y. C. Jun, J. Reno, T. Ribaudo, et al., “Epsilon-near-zero strong coupling in metamaterial-semiconductor hybrid structures,” *Nano Lett.*, vol. 13, no. 11, pp. 5391—5396, 2013.
[14] Y.-W. Huang, H. W. H. Lee, R. Sokhoyan, et al., “Gate-tunable conducting oxide metasurfaces,” *Nano Lett.*, vol. 16, no. 9, pp. 5319—5325, 2016.
[15] G. V. Naik, V. M. Shalaev, and A. Boltasseva, “Alternative plasmonic materials: beyond gold and silver,” *Adv. Mater.*, vol. 25, no. 24, pp. 3264—3294, 2013.
[16] M. Z. Alam, I. De Leon, and R. W. Boyd, “Large optical nonlinearity of indium tin oxide in its epsilon-near-zero region,” *Science*, vol. 352, no. 6287, pp. 795—797, 2016.
[17] S. A. Schulz, A. A. Tahir, M. Z. Alam, J. Upham, I. De Leon, and R. W. Boyd, “Optical response of dipole antennas on an epsilon-near-zero substrate,” *Phys. Rev. A*, vol. 93, no. 6, p. 063846, 2016.
[18] Y. Zhou, M. Z. Alam, M. Karimi, et al., “Broadband frequency translation through time refraction in an epsilon-near-zero material,” *Nat. Commun.*, vol. 11, no. 1, pp. 1—7, 2020.
[19] S. Vassant, J.-P. Hugonin, F. Marquier, and J.-J. Greffet, “Berreman mode and epsilon near zero mode,” *Opt. Express*, vol. 20, no. 21, pp. 23971—23977, 2012.
[20] V. Bruno, S. Vezzoli, C. DeVault, et al., “Broad frequency shift of parametric processes in epsilon-near-zero time-varying media,” *Appl. Sci.*, vol. 10, no. 4, p. 1318, 2020.
[21] R. Czaplicki, A. Kiviniemi, M. J. Huttunen, et al., “Less is more: enhancement of second-harmonic generation from metasurfaces by reduced nanoparticle density,” *Nano Lett.*, vol. 18, no. 12, pp. 7709—7714, 2018.

Supplementary Material: This article contains supplementary material (https://doi.org/10.1515/nanoph-2022-0756).

Chapter 4

Interactions of fundamental Mie modes with thin epsilon-near-zero substrates

Contribution Statement

This project was jointly conceived by M. Zahirul Alam and myself during the middle of my first year of doctoral studies. Dielectric metasurfaces have emerged as promising platforms in the field of optics due to their ability to manipulate light at sub-wavelength scales, offering advantages over their metallic counterparts such as lower loss and a large refractive index. Our research group, after investigating the significant nonlinear optical response of both bare indium-tin-oxide (ITO) samples and plasmonic metasurfaces on ITO, became intrigued by the potential for achieving substantial nonlinear responses with dielectric metasurfaces on ITO. The project was divided into two distinct phases: linear and nonlinear.

In the linear phase, I utilized Comsol Multiphysics to design and simulate two sets of metasurfaces, each specifically tailored to explore the strong coupling between the epsilon-near-zero (ENZ) mode and one of the fundamental Mie modes of a dielectric metasurface: electric dipole resonance (EDR) and magnetic dipole resonance (MDR). Subsequently, I generated layouts for electron beam lithography and collaborated with Kashif Awan, who fabricated the physical samples based on these designs. I conducted the linear optical measurements of the metasurfaces, providing guidance to Y. Vaddi throughout the process. Additionally, I refined the measurement procedures to enhance the clarity of the observed spectral features exhibited by the devices. The analysis of the acquired data and the development of a fitting model were also undertaken by me. Furthermore, I took the lead in writing the initial draft of the research paper.

During the nonlinear phase of the project, the sample was subjected to testing within the identical pump-probe setup made by myself in the experiments discussed in Chapter 2.

Numerous nonlinear experiments can be conducted utilizing these samples. However, for the purposes of this paper, our focus is exclusively directed towards the investigation of ultra-fast modulation pertaining to the transmittance of a probe beam through the samples, triggered by the presence of an intense pump beam.

My contributions to the paper were as follows:

- Conception of the project (main contributor alongside with M. Zahirul Alam)
- Design and simulation of two separate groups of metasurfaces using Comsol Multiphysics (main contributor)
- Building the experimental set-up (main contributor)
- Automating the set-up (main contributor)
- Performing experiment/data collection (main contributor)
- Analysing the experimental data (main contributor)
- Writing the first draft of the paper (main contributor)

Interactions of fundamental Mie modes with thin epsilon-near-zero substrates

Mohammad Karimi,[*,†] Kashif Masud Awan,[‡] Yaswant Vaddi,[†] Rasoul Alaee,[¶] Jeremy Upham,[§] M. Zahirul Alam,[*,§] and Robert W. Boyd[§,‖]

†*Department of Electrical and Computer Engineering, University of Ottawa, Ottawa, ON, Canada, K1N 6N5*

‡*Institute of Materials Science and Engineering, Washington University in Saint Louis, St.Louis, MO 63130, USA*

¶*Institute of Theoretical Solid State Physics, Karlsruhe Institute of Technology, Wolfgang-Gaede-Str.1, 76131, Karlsruhe, Germany*

§*Department of Physics, University of Ottawa, Ottawa, ON, Canada, K1N 6N5*

‖*Institute of Optics, University of Rochester, 275 Hutchison Rd Wilmot Bldg, Rochester, NY 14620, USA*

Abstract

Extensive research has focused on Mie modes in dielectric nano-resonators, enabling the creation of thin optical devices surpassing their bulk counterparts. This study investigates the interactions between two fundamental Mie modes, electric and magnetic dipoles, and epsilon-near-zero (ENZ) mode. Analytical, simulation, and experimental analyses reveal that the presence of the ENZ substrate significantly modifies these modes despite a large size mismatch. Electric and magnetic dipole modes, both with

~12 THz linewidths, exhibit 21 and 26 THz anti-crossings, respectively, when coupled to the ENZ mode, indicating strong coupling. We also demonstrate that this strongly-coupled system yields notably large sub-picosecond nonlinear responses. Our results establish a solid foundation for designing functional, nonlinear, dynamic dielectric metasurfaces with ENZ materials.

KEYWORDS: Nonlinear Optics, Epsilon-Near-Zero, Metasurface, Nano-optics

Introduction

Dielectric nanoantennas, constructed from materials with high refractive indices and low loss compared to plasmonic counterparts, serve as the building blocks for the next generation of nanophotonic devices.[1] Unlike plasmonic nanoantennas, they easily integrate into existing CMOS fabrication lines[2] and, even with simple geometries, support multiple optical resonances, including electric and magnetic dipoles and quadrupoles referred to as Mie modes.[3] The availability of multiple resonant modes in the dielectric nanoantennas allows for tailoring near-field and far-field properties of light.[4–22] In a parallel vein, thin layers of ENZ materials have distinctive linear and nonlinear optical properties, arising from a nearly zero real part of permittivity within specific wavelength ranges.[23] Notably, materials such as indium tin oxide (ITO) and aluminum-doped zinc oxide (AZO) have been extensively explored for their large nonlinear responses.[24,25]

In this work, we investigate how the Mie resonances of dielectric nanoantenna couple with the ENZ mode of a thin ITO substrate. An ENZ mode is an inherently dark mode with a largely enhanced electric field inside a very thin ENZ layer sandwiched between two dielectrics.[26] Extensive research has been conducted on the interaction between the modes of plasmonic nanostructures and the ENZ mode of various near-zero-permittivity materials, including transparent conducting oxides,[27,28] semiconductors,[29] and phonon-based ENZ materials.[30] Plasmonic systems often exhibit pronounced losses, which need to be addressed. Additionally, achieving higher-order modes in these systems necessitates intricate engineering efforts to shape the antennas, adding an additional layer of complexity to the design process.[31] In Mie resonances, unlike plasmonic resonances, the mode is typically concentrated within the dielectric material rather than along the surfaces; therefore, the opportunity for strong modal overlap with the ENZ mode of a nearby structure is expected to be smaller. However, we show that even for a simple dielectric nanoantenna geometry, the field enhancement of Mie modes is sufficient to achieve strong coupling with the ENZ mode. We experimentally and theoretically demonstrate that the two fundamental Mie modes (electric and magnetic dipole resonances) of silicon dielectric antennas can strongly couple with the ENZ mode of a 23-nm-thick ITO substrate. Furthermore, using simple pump-probe measurements, we demonstrate strongly enhanced transmission modulation of these structures, in comparison to bare ITO. This suggests that that metasurface composed of dielectric nanoantennas and ENZ thin films have significant potential for nonlinear optical applications, at least as significant, and perhaps more varied, than their plasmonic counterparts.

Results and discussion

Simulations

In general, the resonance wavelength of a Mie mode is a complicated function of the geometric and material properties of the dielectric nano-antenna. We selected cuboid antenna shapes since the three geometric parameters – length, width, and height – allow sufficient freedom to investigate the interaction between one fundamental dipole resonance (either electric or magnetic) and the ENZ mode while keeping the other dipole resonance spectrally separate from the ENZ resonance condition.[32] Figure 1(a) and 1(b) demonstrate the permittivity of the ITO substrate we used and a schematic of the device with and without ITO, respectively. The ENZ mode resonance, as discussed in the following section, is near the wavelength where the real part of the permittivity crosses from positive to negative, so that is the wavelength at which Mie resonances could couple to the ENZ mode. In this work, we focus on the electric

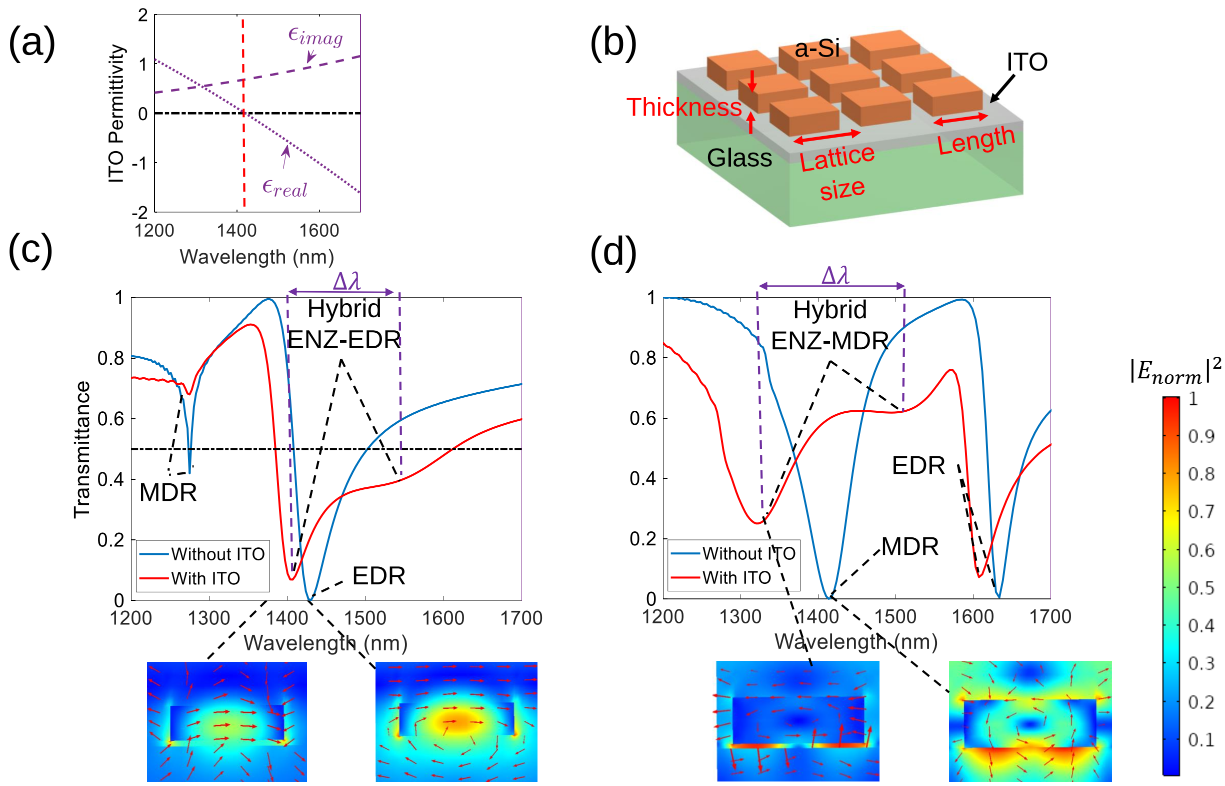

Figure 1: (a) The real and imaginary parts of the permittivity of the ITO sample taken from the ellipsometry data; the red dashed line specifies at 1410 nm is the zero crossing point. (b) The schematics of the a-Si metasurface on ITO on glass. (c) and (d) The comparison of the transmittance of the metasurfaces over the glass and over ITO for observing the interaction of the (c) electric dipole resonance (EDR) and (d) magnetic dipole resonance (MDR) with the ENZ mode. The length, width, and thickness of the antennas and the lattice constant in the Figure are 560, 500, 140, and 850 nm, respectively, for part (c) and 650, 650, 210, and 810 nm, respectively for part (d). The parameter $\Delta\lambda$ indicates the amount of anti-crossing that occurs due to the strong coupling effect, and it is around 140 nm for the EDR case and around 200 nm for the MDR case. The insets show the electric field amplitude distribution and direction around the antennas for different resonance modes specified in the transmittance plots.

dipole resonance (EDR) and the magnetic dipole resonance (MDR) of the antennas. Higher-order modes, such as quadrupole, likely respond similarly but will be subject of subsequent research. We designed two groups of metasurfaces, each designed to center either the EDR or the MDR near the ENZ mode wavelength while keeping all other resonance modes at least two linewidths away from the ENZ wavelength. To design the metasurfaces, we swept over different dimensions of the single antennas and the lattice constant over the glass in our simulations using Comsol Multiphysics while tracking the resonance wavelength and mode of each of the Mie resonances. We then found the dimensions that set the resonances to the ENZ mode's central wavelength, added the ITO layer as the substrate, and compared the results in the presence and absence of ITO. Figure 1 demonstrate the effect of a 23-nm layer of ITO as the substrate on the transmittance of one of our EDR samples and one of our MDR samples, respectively. The length, width, and thickness of the antennas and the lattice constant in the Figure 1 are 560, 500, 140, and 850 nm, respectively, for the EDR case and 650, 650, 210, and 810 nm, respectively for the MDR case. In both cases, the presence of ITO splits the Mie resonance into two hybrid modes: one at a shorter and one at a longer wavelength than the resonance wavelength of the same metasurfaces on glass; we call them lower polariton branch and upper polariton branch, respectively, for the remainder of the manuscript. Note that the lower polariton branch exhibits a smaller dip in transmittance than the upper polariton branch, which can be attributed to the non-negligible loss of ITO. similar asymmetry in the depth of the transmission resonances has been reported before.[33,34] The appearance of these hybrid modes is the main sign of coupling between the fundamental Mie modes and the ENZ mode.[35] The spectral separation of the hybrid modes, $\Delta\lambda$, is proportional to the strength of coupling, and the system is said to be in a strong coupling regime if the spectral separation is larger than the linewidth of the fundamental Mie mode in the absence of ITO.[35] These simulations predict hybridized mode splitting larger than the FWHM linewidth of the Mie resonances without the ITO substrate, suggesting that the systems are in strong coupling regimes.

The field distributions of the EDR and MDR are distinguishable inside and in the vicinity of the nanoantennas at the resonance wavelength. The insets in Figures 1 (c) and 1 (d) show the electric field intensities and vectorial distributions at the EDR and MDR without the ITO thin film, as well as the higher polariton branch of each when this ENZ substrate is included. At the EDR, the electric field concentrates within the center of the nanoantenna, with the polarization determined by the incident field. At the MDR, the electric field vectors circle inside the antenna such that the curl of the electric field points in the direction of the magnetic dipole. When introducing a thin ITO layer as the substrate, the upper polariton resonances show that a visibly significant portion of the electric field within the antennas penetrates the ITO layer due to strong coupling for both resonances.

Analytical modelling and comparison to the simulations

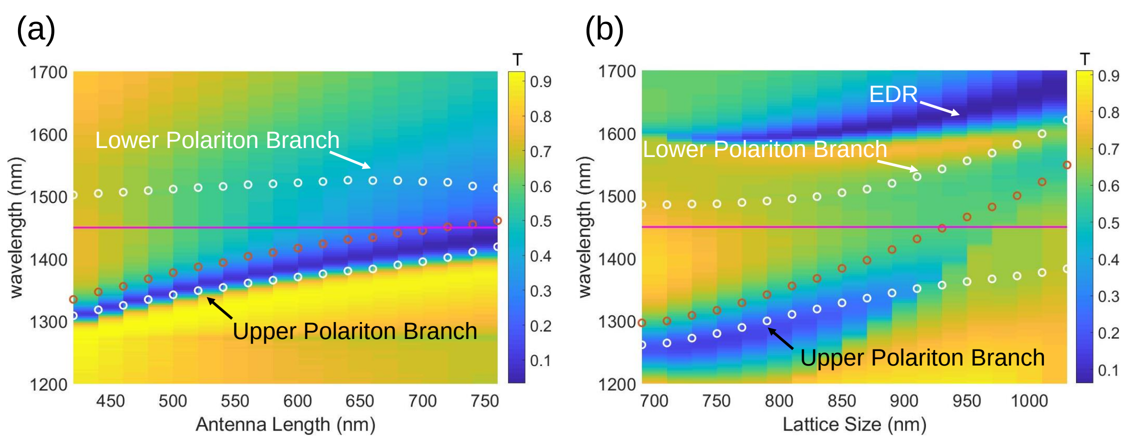

Figure 2: Comparison of analytical derivation and numerical simulation of hybridized mode splitting. To show tuning of (a) the EDR and (b) the MDR across the ENZ mode transmission spectra for different antenna lengths or lattice sizes, respectively, were simulated in Comsol Multiphysics. The red circles are the position of the EDR and MDR in (a) and (b), respectively, with the antennas without ITO derived from the simulation results. The white circles specify the position of the upper and lower polariton branches predicted by the analytical solution.

To investigate the strongly coupled system in more detail, we simulated the transmittance of the metasurfaces with different dimensions for the EDR and MDR samples using Comsol

Multiphysics. Sweeping the dimensions such that one Mie resonance crossed the ENZ mode revealed the anticrossing of the hybridized modes in the transmittance. Figures 2 (a) and 2 (b) show the simulated transmittance at different wavelengths for EDR and MDR samples, respectively, as functions of the length of the antennas for the EDR samples and the size of the lattice for the MDR samples. The red circles in both figures specify the spectral positions of the numerically obtained resonances under study with metasurfaces over the glass without ITO, while the central wavelength of the ENZ mode ($\sim$ 1460 nm), derived from the wave equation 2, is demonstrated with solid lines. For the hybridized modes, the polariton branches are observable in Figure 2 as transmittance dips. While the upper polariton is clearly visible, the lower polariton's dip in transmission is more subtle.

In our analytical model, the central wavelength of the ENZ mode was derived by solving the following dispersion relation of the modes in a thin layer of material with a permittivity of ε_1 sandwiched between two layers of permittivities ε_0 and ε_2 [26] :

$$1 + \frac{\varepsilon_0 k_{z2}}{\varepsilon_2 k_{z0}} = i\tan(k_{z1}d)(\frac{\varepsilon_1 k_{z2}}{\varepsilon_2 k_{z1}} + \frac{\varepsilon_0 k_{z1}}{\varepsilon_1 k_{z0}}) \tag{1}$$

where $k_{zi}^2 = \varepsilon_i \frac{\omega^2}{c^2} - k_{||}^2$, $k_{||}$ is the transverse wavenumber; ω is the angular frequency; d is the thickness of the middle layer; and c is the speed of light in vacuum. To solve these equations, we used the permittivity of ITO derived from the ellipsometry data. We found that the central wavelength of the ENZ mode is around 1460 nm. Note that this wavelength is different from the point where the real part of permittivity vanishes, although they are near each other.

To analyze the strongly coupled system, we used the theory explained in previous works.[35,36] According to this model, the frequencies of the lower and upper branches after the coupling can be calculated as a function of the isolated resonance frequencies using the following relations:

$$\omega_{\pm} = \frac{1}{2}(\omega_{\mathrm{DR}} + \omega_{\mathrm{ENZ}} \pm \sqrt{(\omega_{\mathrm{DR}} - \omega_{\mathrm{ENZ}})^2 + 4\Delta^2}) \tag{2}$$

where $\Delta = 2\pi\Delta f$ is the angular frequency difference between the split modes; ω_+ and ω_- are the frequencies of the hybrid modes of upper and lower polariton branches, respectively; and ω_{DR} and ω_{ENZ} are the resonance frequencies for the dipole resonances and the ENZ mode, respectively. The white circles in Figures 2(a) and 2(b) represent the analytically obtained resonances. We use Δf as a fitting parameter in our analytical model to minimize the deviation of the upper and lower polariton branches between the numerical simulation and the analytical results. This value of Δf is equal to the spectral separation of hybrid modes at the dimension that they are nearest to each other. This value of Δf is equal to the spectral separation of hybrid modes at the dimension that they are nearest to each other. We find Δf = 21 THz for the EDR case and Δf = 26 THz for the MDR case. Comparing the magnitude of this anti-crossing with the linewidths of the resonances in the absence of ITO (around 12 THz) shows that the degree of anti-crossing is significantly larger than the linewidths of either Mie resonance in the absence of ITO, suggesting a strong coupling between those resonances and the ENZ mode. We note that this simple strong coupling theory describes the coupling of each Mie mode to the ENZ mode in a geometrically complex system. According to Eq. 1, the ENZ mode's central frequency depends on the superstrate's permittivity. In our case, the effective permittivity of the metasurface superstrate undergoes significant modification due to the antennas and their resonant conditions. Covering over 40% of the surface area and possessing substantial refractive indices, combined with non-negligible thicknesses, these antennas substantially alter the central frequency of the ENZ mode. That can explain the slight deviations in analytical results from the simulation.

Experimental results

We fabricated structures with different antennas/lattice dimensions to study the coupling of the EDR/MDR to the ENZ mode. A 23 nm-thick ITO on SiO2 samples was obtained from a commercial source. The ITO samples were cleaned, followed by deposition of 230 nm a-Si via PECVD at 1000 mT, 210 oC with an RF power of 10 W using 25 sccm Silane

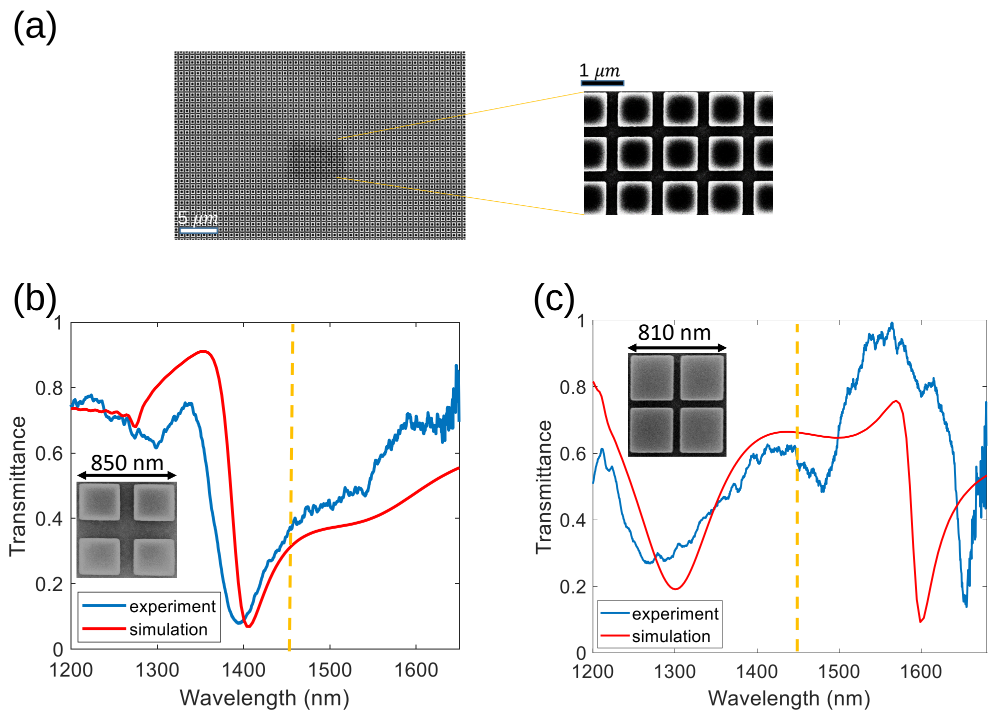

Figure 3: (a) The SEM image of one of the fabricated devices. (b) and (c) The comparison of the transmittance in simulation and experiment of one representative EDR sample (b) and one representative MDR sample (c). The vertical dashed line shows the central wavelength of the ENZ mode. The SEM images in the insets show 4 unit cells of the metasurface for which the experimental data is shown. The dimensions of the samples were the same as those used for Figures 1. The orange dashed lines specify the central wavelength of the ENZ mode derived by solving the wave equation 2.

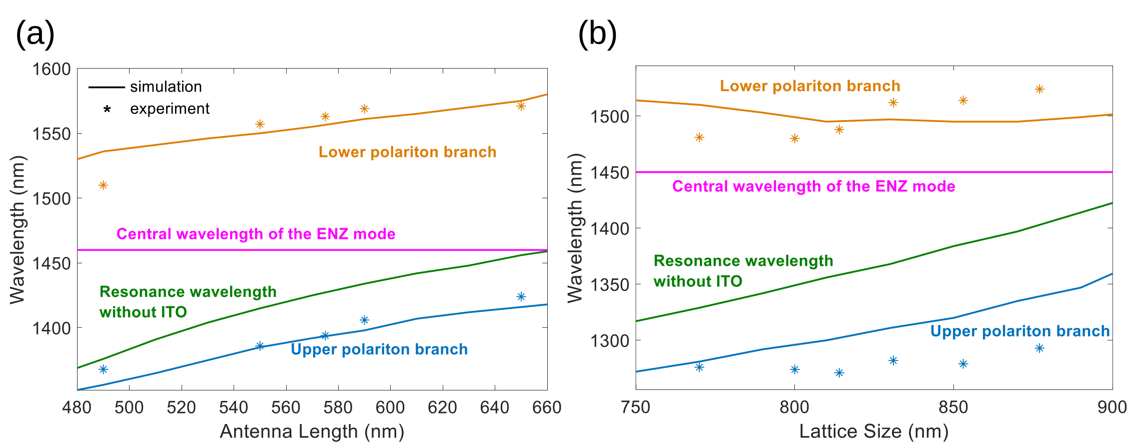

Figure 4: The position of different resonances in the wavelength domain for (a) the EDR sample for different antenna lengths and (b) the MDR sample for different lattice sizes.

and 475 sccm of Argon. To pattern the metasurface into the a-Si layer, a spin-coat of 500 nm Zep-520a (a positive-tone EBL resist) was hard baked at 180 oC for 2 min, then was exposed using a 100 keV EBL system with a dosage of 210 $\mu C/cm2$ followed by development in N-Amy Acetate for 1 min. The pattern is then transfered into the a-Si layer by ICP-RIE a pressure of 10 mT, temperature of 20 oC, ICP power of 100 W, and RIE power of 20 W with 30 sccm of C4F8 and 20 sccm of SF6. Residual Zep resist was then removed using acetone before inspection of the samples using optical and electron microscopes. Figure 3 in the main text (a) shows the SEM image of one of the fabricated devices. Figure 3 (a) shows the SEM image of one of the fabricated devices.

The samples were characterized in a wide-band linear measurement set-up where a polarized uncollimated white light was focused on the samples and then recollected to measure the transmittance of the metasurfaces on ITO. Figures 3 (b) and 3(c) show the simulated and experimental transmittance of representative EDR and MDR samples, respectively. We observe a very good agreement between the experimental and simulation data in the magnitude of the anti-crossings and the depth of the upper polariton branch, although there are some minor deviations in the resonance wavelengths and the transmittance. The deviations mostly arise from the uncertainty in the thickness of ITO at different locations of the samples. During fabrication, the dry etching process may have partially removed ITO from the exposed spaces between nanoantennas. fabrication variations in the dimensions of the antennas could be another reason for deviations.

Figures 4(a) and 4(b) show the simulation and experimental results of the resonant wavelengths of different resonances as a function of dimensions. We extracted the position of the polariton branches in the experiment from the transmittance for each sample as indicated by points in Figure 4(a) for the EDR case and Figure 4(b) for the MDR case. We observe a good agreement between the simulation and experiment for the EDR and MDR cases.

We have shown with simulations, analytical modeling, and experimental characterization that the two fundamental Mie modes of an a-Si metasurface, EDR, and MDR, can strongly couple to the ENZ mode of a 23-nm layer of ITO. The main evidence for the strong coupling between the modes above is the avoided crossing of the hybrid modes of the metasurface over ITO that is larger than the linewidths of the Mie modes in the absence of ITO. The strength of the coupling and the depth of the resonances related to the hybrid modes could be further strengthened by using slightly thicker ITO layers to reduce the modal volume mismatch between the ENZ mode and the Mie modes.

Nonlinear response of the strongly-coupled system

Plasmonic metasurfaces that are strongly coupled to an ENZ mode of a TCO substrate have been shown to strongly enhance the nonlinear optical response of the ENZ material and thus create the opportunity for engineering dynamic, highly nonlinear metasurfaces.[33,36,37] As a proof of principle for using the strongly coupled Mie-ENZ hybridized modes shown here in nonlinear applications, we performed degenerate pump-probe experiments, sketched schematically in Figure 5(a), using 120 femtoseconds (fs) pulses. The pump pulses trigger a nonlinear response of the coupled sample of nanoantennas and ITO substrate similar to the plasmonic nanoantennas over ITO, which is then characterized by the transmittance of the weaker probe pulse at different relative timings to the pump.[33,37] Note that the role of antennas is crucial here both because they confine more light into the ITO layer, as can be seen in Figure 1, and also because they pave the way for the light to couple from free space to the ENZ mode of the ITO layer.[24] By transferring from the linear to the nonlinear regime, the effective refractive index of the coupled system changes, consequently leading to the shift of the resonance position of the hybrid modes, as well as the depth of the resonances. Under such circumstances, the transmittance of a probe beam that travels through the sample may increase or decrease depending on the spectral position of the incident wavelength with respect to the resonances. The experimental results obtained from our samples are shown in Figure 5(b). We swept over the delay time between the pump and the probe for different

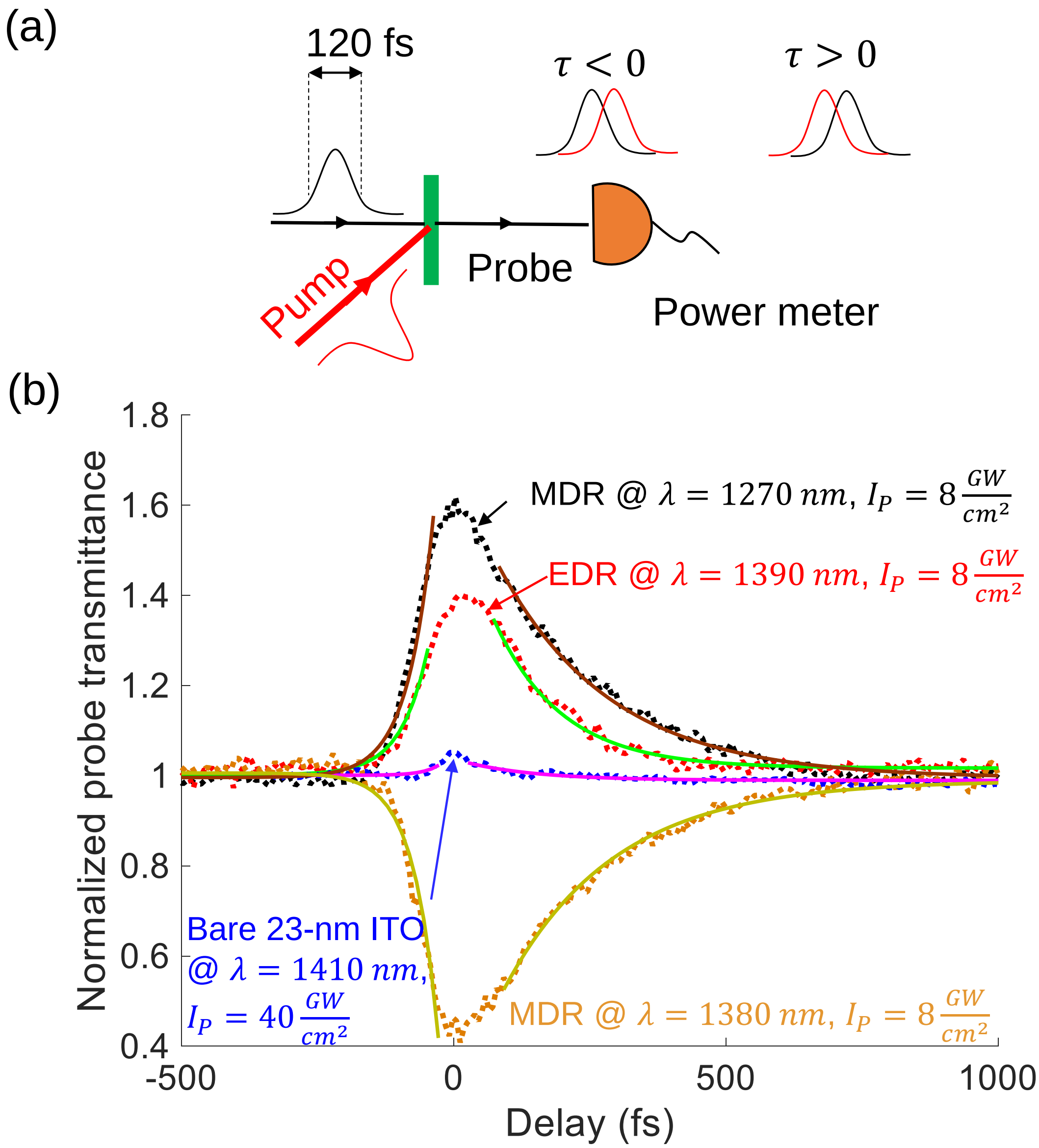

Figure 5: Nonlinear behavior of the samples. (a) A simple schematic of the time-resolving degenerate nonlinear measurement set-up. An intense femtosecond (fs) pump beam triggers the nonlinear response of the sample, while a probe beam of the same duration interacts with the modified medium. (b) The normalized transmittance of the probe. The dotted lines show the normalized transmittance of a probe beam of light plotted with respect to the time delay between the pump and the probe for a bare 23-nm ITO sample (in blue), one of the arrays in the EDR sample (in red), and one of the arrays in MDR sample at different incident wavelengths (1270nm in black, and 1380 nm in brown). Negative time delays mean the probe precedes the pump at the sample. The solid curves represent the fitting results of the rising and falling edges of each curve to exponential equations to derive the rise and fall times of the induced nonlinear change in transmission. for the blue, red, black, and brown dotted curves, the faster rise times are 35, 49, 47, and 46 fs, while the slower relaxation times are 132, 130, 205, and 200 fs, respectively.

samples and in different central wavelengths of the beams and recorded the transmitted power of the probe for various time delays. Significantly, we also include transmission results obtained in the same pump-probe setup for a bare 23-nm ITO sample for comparison. All of the metasurfaces show immensely larger (up to 20 times) modifications in the transmitted power of the probe compared to the bare 23-nm ITO sample, despite the metasurfaces being pumped with one-fifth the intensity used to pump the bare ITO sample. This reinforces that the metasurfaces do achieve a stronger nonlinear response by enabling coupling to the ENZ mode and enhancing the fields therein. The solid curves in the figure represent the fitting results of the rising and falling edges of each curve to exponential equations to derive the rise and fall times of the induced nonlinear change in transmission. For the blue, red, black, and brown curves, the faster rise times are 35, 49, 47, and 46 fs, while the slower relaxation times are 132, 130, 205, and 200 fs, respectively.

The MDR sample specifically shows much richer dynamics than what was observed for the EDR one, with increasing or decreasing transmission response with respect to the time delay depending on the incident wavelength. This richer response can be attributed to the stronger coupling of the MDR to ENZ and larger line widths of hybrid modes in the MDR samples. A transmittance amplitude modulation of the same order of magnitude as in our case is achievable using plasmonic metasurfaces over ITO. However, the multi resonance nature of our scheme, with the possibility to control each resonance separately, can make it a more powerful building block for designing dynamic all-optical systems.[38] A complete investigation of the nonlinear response of these samples and how they compare with each other and with a bare ITO sample requires a more detailed analysis and is beyond the scope of this work. We note here that the speed of modification of the transmittance in our strongly coupled system of a-si and ITO is at least one order of magnitude higher than the previously reported modification speeds of systems based on silicon.[39,40] This shows the potential of our scheme for ultrafast all-optical modulators. In addition, the nonlinear response of the samples may get stronger by using slightly thicker ITO layers. The nonlinear response of an array of dielectric metasurfaces over 33-nm ITO, where the EDR and the MDR both overlap with each other at some wavelength at the ENZ region, has been recently reported.[41] However, their discussion lacks the impact of each resonance on the linear and nonlinear responses of the sample at different wavelengths separately, as included in our work. Understanding how each of these modes responds to the presence of an ENZ layer separately is essential for designing systems with more complicated spatiotemporal responses, such as gradient metasurfaces, where antennas of different resonance properties form the metasurface.

In conclusion, we designed, simulated, fabricated, and tested a system to demonstrate strong coupling between the fundamental EDR and MDR Mie modes in an a-Si metasurface to the ENZ mode of a thin layer of ITO. Clear agreement between analytical, simulation, and experimental results confirmed that strong coupling of individual Mie resonances to the ENZ mode could be achieved, eliminating the concern that Mie resonances would have insufficient mode overlap with the ENZ mode to do so. Furthermore, we performed pump-probe nonlinear measurements that showed at least a 100-fold enhancement of transmission modulation through the metasurface in comparison to the already highly nonlinear bare ITO. The metasurface also seems to alter the sub-picosecond onset and relaxation times of this modulation, although this relationship merits further investigation. Such coupled metasurface systems could be used for many applications requiring highly nonlinear responses with sub-ps temporal modulation. While this was already known for plasmonic metasurfaces,[33,36,37] the option for doing so with dielectric nanoantennas significantly expands the fabrication options. Potentially, even more importantly, it enables dynamically modulated coupling to higher quality factor resonances and magnetic dipole modes.

acknowledgement

This work was supported by Natural Sciences and Engineering Research Council of Canada under Discovery Grant RGPIN/2017-06880, the Canada Research Chairs program under award 950-231657, the Canada First Research Excellence Fund on Transformative Quantum Technologies under award 072623. RWB acknowledges the US Office of Naval Research award N00014-19-1-2247 and MURI award N00014-20-1-2558. R. A. acknowledges the support of the Alexander von Humboldt Foundation through the Feodor Lynen Fellowship. We acknowledge the support of Stewart Blusson Quantum Matter Institute and the use of their Advanced Nanofab Facility for the fabrication of the samples. KA acknowledges funding from SiEPIC fab for the fabrication of the devices.

References

(1) Jahani, S.; Jacob, Z. All-dielectric metamaterials. *Nature nanotechnology* **2016**, *11*, 23–36.

(2) Xiong, C.; Bell, B.; Eggleton, B. J. CMOS-compatible photonic devices for single-photon generation. *Nanophotonics* **2016**, *5*, 427–439.

(3) Liu, T.; Xu, R.; Yu, P.; Wang, Z.; Takahara, J. Multipole and multimode engineering in Mie resonance-based metastructures. *Nanophotonics* **2020**, *9*, 1115–1137.

(4) Azzam, S. I.; Kildishev, A. V. Photonic bound states in the continuum: from basics to applications. *Advanced Optical Materials* **2021**, *9*, 2001469.

(5) Tian, J.; Li, Q.; Belov, P. A.; Sinha, R. K.; Qian, W.; Qiu, M. High-Q all-dielectric metasurface: super and suppressed optical absorption. *Acs Photonics* **2020**, *7*, 1436–1443.

(6) Kuznetsov, A. I.; Miroshnichenko, A. E.; Brongersma, M. L.; Kivshar, Y. S.; Luk'yanchuk, B. Optically resonant dielectric nanostructures. *Science* **2016**, *354*, aag2472.

(7) Chong, K. E.; Wang, L.; Staude, I.; James, A. R.; Dominguez, J.; Liu, S.; Subramania, G. S.; Decker, M.; Neshev, D. N.; Brener, I.; others Efficient polarization-insensitive complex wavefront control using Huygens' metasurfaces based on dielectric resonant meta-atoms. *Acs Photonics* **2016**, *3*, 514–519.

(8) Rahimzadegan, A.; Arslan, D.; Dams, D.; Groner, A.; Garcia-Santiago, X.; Alaee, R.; Fernandez-Corbaton, I.; Pertsch, T.; Staude, I.; Rockstuhl, C. Beyond dipolar Huygens' metasurfaces for full-phase coverage and unity transmittance. *Nanophotonics* **2019**, *9*, 75–82.

(9) Yang, Q.; Kruk, S.; Xu, Y.; Wang, Q.; Srivastava, Y. K.; Koshelev, K.; Kravchenko, I.; Singh, R.; Han, J.; Kivshar, Y.; others Mie-Resonant Membrane Huygens' Metasurfaces. *Advanced Functional Materials* **2020**, *30*, 1906851.

(10) Alaee, R.; Filter, R.; Lehr, D.; Lederer, F.; Rockstuhl, C. A generalized Kerker condition for highly directive nanoantennas. *Optics letters* **2015**, *40*, 2645–2648.

(11) Liu, W.; Kivshar, Y. S. Generalized Kerker effects in nanophotonics and meta-optics. *Optics express* **2018**, *26*, 13085–13105.

(12) Hwang, M.-S.; Lee, H.-C.; Kim, K.-H.; Jeong, K.-Y.; Kwon, S.-H.; Koshelev, K.; Kivshar, Y.; Park, H.-G. Ultralow-threshold laser using super-bound states in the continuum. *Nature Communications* **2021**, *12*, 4135.

(13) Huang, C.; Zhang, C.; Xiao, S.; Wang, Y.; Fan, Y.; Liu, Y.; Zhang, N.; Qu, G.; Ji, H.; Han, J.; others Ultrafast control of vortex microlasers. *Science* **2020**, *367*, 1018–1021.

(14) Tuz, V. R.; Khardikov, V. V.; Kivshar, Y. S. All-dielectric resonant metasurfaces with a strong toroidal response. *ACS Photonics* **2018**, *5*, 1871–1876.

(15) Kivshar, Y. All-dielectric meta-optics and non-linear nanophotonics. *National Science Review* **2018**, *5*, 144–158.

(16) Kruk, S.; Kivshar, Y. Functional meta-optics and nanophotonics governed by Mie resonances. *Acs Photonics* **2017**, *4*, 2638–2649.

(17) Zograf, G.; Zalogina, A.; Koshelev, K.; Choi, D.-Y.; Korolev, V.; Hollinger, R.; Kartashov, D.; Zürch, M.; Spielmann, C.; Makarov, S.; others High-harmonic generation in dielectric metasurfaces empowered by bound states in the continuum. 2020 Conference on Lasers and Electro-Optics (CLEO). 2020; pp 1–2.

(18) Shcherbakov, M. R.; Liu, S.; Zubyuk, V. V.; Vaskin, A.; Vabishchevich, P. P.; Keeler, G.; Pertsch, T.; Dolgova, T. V.; Staude, I.; Brener, I.; others Ultrafast all-optical tuning of direct-gap semiconductor metasurfaces. *Nature communications* **2017**, *8*, 1–6.

(19) Koshelev, K.; Kruk, S.; Melik-Gaykazyan, E.; Choi, J.-H.; Bogdanov, A.; Park, H.-G.; Kivshar, Y. Subwavelength dielectric resonators for nonlinear nanophotonics. *Science* **2020**, *367*, 288–292.

(20) Bohn, J.; Bucher, T.; Chong, K. E.; Komar, A.; Choi, D.-Y.; Neshev, D. N.; Kivshar, Y. S.; Pertsch, T.; Staude, I. Active tuning of spontaneous emission by Mie-resonant dielectric metasurfaces. *Nano letters* **2018**, *18*, 3461–3465.

(21) Forouzmand, A.; Mosallaei, H. Dynamic beam control via Mie-resonance based phase-change metasurface: a theoretical investigation. *Optics express* **2018**, *26*, 17948–17963.

(22) Vaskin, A.; Mashhadi, S.; Steinert, M.; Chong, K. E.; Keene, D.; Nanz, S.; Abass, A.; Rusak, E.; Choi, D.-Y.; Fernandez-Corbaton, I.; others Manipulation of magnetic dipole emission from Eu3+ with Mie-resonant dielectric metasurfaces. *Nano letters* **2019**, *19*, 1015–1022.

(23) Reshef, O.; De Leon, I.; Alam, M. Z.; Boyd, R. W. Nonlinear optical effects in epsilon-near-zero media. *Nature Reviews Materials* **2019**, *4*, 535–551.

(24) Alam, M. Z.; De Leon, I.; Boyd, R. W. Large optical nonlinearity of indium tin oxide in its epsilon-near-zero region. *Science* **2016**, *352*, 795–797.

(25) Vezzoli, S.; Bruno, V.; DeVault, C.; Roger, T.; Shalaev, V. M.; Boltasseva, A.; Ferrera, M.; Clerici, M.; Dubietis, A.; Faccio, D. Optical time reversal from time-dependent epsilon-near-zero media. *Physical review letters* **2018**, *120*, 043902.

(26) Vassant, S.; Hugonin, J.-P.; Marquier, F.; Greffet, J.-J. Berreman mode and epsilon near zero mode. *Optics express* **2012**, *20*, 23971–23977.

(27) Campione, S.; Wendt, J. R.; Keeler, G. A.; Luk, T. S. Near-infrared strong coupling between metamaterials and epsilon-near-zero modes in degenerately doped semiconductor nanolayers. *Acs Photonics* **2016**, *3*, 293–297.

(28) Schulz, S. A.; Tahir, A. A.; Alam, M. Z.; Upham, J.; De Leon, I.; Boyd, R. W. Optical response of dipole antennas on an epsilon-near-zero substrate. *Physical Review A* **2016**, *93*, 063846.

(29) Jun, Y. C.; Reno, J.; Ribaudo, T.; Shaner, E.; Greffet, J.-J.; Vassant, S.; Marquier, F.; Sinclair, M.; Brener, I. Epsilon-near-zero strong coupling in metamaterial-semiconductor hybrid structures. *Nano letters* **2013**, *13*, 5391–5396.

(30) Passler, N. C.; Gubbin, C. R.; Folland, T. G.; Razdolski, I.; Katzer, D. S.; Storm, D. F.; Wolf, M.; De Liberato, S.; Caldwell, J. D.; Paarmann, A. Strong coupling of epsilon-near-zero phonon polaritons in polar dielectric heterostructures. *Nano letters* **2018**, *18*, 4285–4292.

(31) Tong, J.; Suo, F.; Tobing, L. Y.; Yao, N.; Zhang, D.; Huang, Z.; Zhang, D. H. High order magnetic and electric resonant modes of split ring resonator metasurface arrays for strong enhancement of mid-infrared photodetection. *ACS applied materials & interfaces* **2020**, *12*, 8835–8844.

(32) Shalaev, M. I.; Sun, J.; Tsukernik, A.; Pandey, A.; Nikolskiy, K.; Litchinitser, N. M. High-efficiency all-dielectric metasurfaces for ultracompact beam manipulation in transmission mode. *Nano letters* **2015**, *15*, 6261–6266.

(33) Alam, M. Z.; Schulz, S. A.; Upham, J.; De Leon, I.; Boyd, R. W. Large optical nonlinearity of nanoantennas coupled to an epsilon-near-zero material. *Nature Photonics* **2018**, *12*, 79–83.

(34) Alaee, R.; Vaddi, Y.; Boyd, R. W. Dynamic coherent perfect absorption in nonlinear metasurfaces. *Optics Letters* **2020**, *45*, 6414–6417.

(35) Novotny, L. Strong coupling, energy splitting, and level crossings: A classical perspective. *American Journal of Physics* **2010**, *78*, 1199–1202.

(36) Bruno, V.; DeVault, C.; Vezzoli, S.; Kudyshev, Z.; Huq, T.; Mignuzzi, S.; Jacassi, A.; Saha, S.; Shah, Y. D.; Maier, S. A.; others Negative refraction in time-varying strongly coupled plasmonic-antenna–epsilon-near-zero systems. *Physical review letters* **2020**, *124*, 043902.

(37) Karimi, M.; Alam, M. Z.; Upham, J.; Reshef, O.; Boyd, R. W. Time-varying gradient metasurface with applications in all-optical beam steering. *Nanophotonics* **2023**, *12*, 1733–1740.

(38) Zhou, Y.; Guo, S.; Overvig, A. C.; Alù, A. Multiresonant Nonlocal Metasurfaces. *Nano Letters* **2023**, *23*, 6768–6875.

(39) Almeida, V. R.; Barrios, C. A.; Panepucci, R. R.; Lipson, M. All-optical control of light on a silicon chip. *Nature* **2004**, *431*, 1081–1084.

(40) Upham, J.; Tanaka, Y.; Asano, T.; Noda, S. On-the-fly wavelength conversion of photons by dynamic control of photonic waveguides. *Applied physics express* **2010**, *3*, 062001.

(41) Wang, K.; Liu, A.-Y.; Hsiao, H.-H.; Genet, C.; Ebbesen, T. Large Optical Nonlinearity of Dielectric Nanocavity-Assisted Mie Resonances Strongly Coupled to an Epsilon-near-Zero Mode. *Nano Letters* **2022**, *22*, 702–709.

Chapter 5

Superscattering, Superabsorption, and Nonreciprocity in Nonlinear Antennas

Contribution Statement

Rasoul Alaei and I had several discussions about the nonlinear response of indium-tin-oxide (ITO) and various ways of simulating this nonlinear response in Comsol Multiphysics and Lumerical FDTD. The challenge is that both environments are inherently designed for solving linear equations; Comsol solves the linear wave equation using the finite element method (FEM), and Lumerical solves the Maxwell Curl equations using the finite difference time domain (FDTD) method. As a result, to include the nonlinear response of the materials in our electromagnetic modeling, we have to use some recurrence method depending on the type of nonlinear response we want to include. In the case of ITO, we used a recurrence method to solve the linear wave equation in Comsol in several steps, where the effective refractive index of ITO in each step is dependent on the electromagnetic field intensity within ITO derived from the step before. Rasoul Alaei wrote the first version of the Comsol code for a slab of ITO based on the discussion above. As the next step, we decided to use this method for nanoantennas made of ITO and to compare their scattering pattern in the linear and nonlinear regimes. As I was working on two other projects at that time, Lin Cheng, a visitor to our group working under the supervision of Akbar Safari and familiar with Lumerical, continued the project. I actively continued to be part of the project to help Lin to remake the Comsol model in Lumerical and complete the simulations, as I was involved in the discussions of nonlinear simulations from the beginning. Also, I was the only group member at that time with expertise in both Comsol and Lumerical.

My contributions to the paper were as follows:

- Conception of the project (Second to Rasoul Alaei, alongside Akbar Safari)

- Rebuilding the model in Lumerical based on the model in Comsol (main contributor, alongside Lin Cheng)
- Analysing the simulation results and deciding on the next steps (third to Rasoul Alaei and Lin Cheng, alongside Akbar Safari)

pubs.acs.org/journal/apchd5

Article

Superscattering, Superabsorption, and Nonreciprocity in Nonlinear Antennas

Lin Cheng,[∥] Rasoul Alaee,[*,∥] Akbar Safari, Mohammad Karimi, Lei Zhang, and Robert W. Boyd

Cite This: *ACS Photonics* 2021, 8, 585−591

Read Online

ABSTRACT: We propose tunable nonlinear antennas based on an epsilon-near-zero material with a large optical nonlinearity. We show that the absorption and scattering cross sections of the antennas can be controlled dynamically from a nearly superscatterer to a nearly superabsorber by changing the intensity of the laser. Moreover, we demonstrate that a hybrid nonlinear antenna, composed of epsilon-near-zero and dielectric materials, exhibits nonreciprocal radiation patterns because of broken spatial inversion symmetry and large optical nonlinearity of the epsilon-near-zero material. By changing the intensity of the laser, the radiation pattern of the antenna can be tuned between a bidirectional and a unidirectional emission known as a Huygens source. Our study provides a novel approach toward ultrafast dynamical control of metamaterials, for applications such as beam steering and optical limiting.

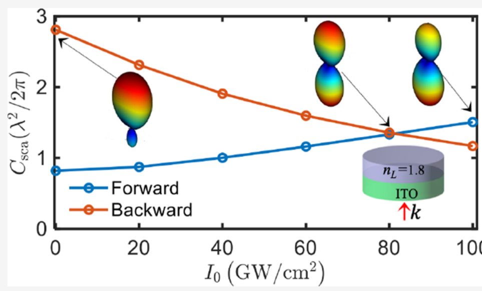

KEYWORDS: *superscattering, superabsorption, nonreciprocity, epsilon-near-zero (ENZ) materials, Kerker effect, optical antennas*

Optical antennas as fundamental building blocks in nanophotonics and metamaterials allow us to manipulate and control optical fields on the nanometer scale.[1] By localizing the energy of a propagating wave, optical antennas provide enhanced control on light−matter interactions for applications such as microscopy[2] and nonlinear optics.[3] Scattering and absorption cross sections are the most important quantities to describe how strong an antenna interacts with the incident light. These cross sections depend on the induced electric and magnetic multipole moments[4] and can be tailored by engineering either the geometry or the material properties of the optical antennas. Considering their wide applications in photonics, various optical antennas have been proposed to achieve fascinating scattering phenomena, including directional emissions known as the Kerker effects,[5−7] superscattering,[8,9] superabsorption,[10−13] optical cloaking,[14] and nonradiating scattering states.[15,16]

In order to realize a versatile control of electromagnetic radiation, it is highly desirable to modulate the optical properties of the antennas dynamically. Recently, epsilon-near-zero (ENZ) materials have been shown to exhibit an exceptionally large intensity-dependent refractive index (see Figure 1a).[17] Therefore, ENZ materials provide a new platform to optically tune the response of the material within a subpicosecond time scale.[17] Specifically, negative refraction, tunable metasurfaces, optical switches, tunable cavities, and coherent perfect absorbers have been achieved using indium tin oxide (ITO) and aluminum-doped zinc oxide (AZO) as ENZ materials.[17−31,31−36]

In this work, we theoretically study the optical response of nonlinear antennas composed of epsilon-near-zero and dielectric materials. Previously, nonlinear antennas have been realized theoretically and experimentally to enhance nonlinear responses such as second-harmonic and third-harmonic generation.[37−42] However, the Kerr-type nonlinearity has not been strong enough to significantly modify the scattering response of the antennas at the fundamental wavelength. In our work, the large Kerr-type nonlinearity of the ENZ material plays a crucial role in changing the induced multipole moments and, thus, drastically modifying the scattering, absorption, and extinction cross sections as well as the radiation pattern of the antennas. In particular, we can optically switch the antennas' response from a nearly superscattering to a nearly superabsorbing state. By employing the multipole expansion of the induced intensity-dependent polarization current, we show that the radiation pattern of the antennas can be tuned from a nondirective to a nearly Huygens source by changing the intensity of the laser. In this work, the terms "scatterers" and "antennas" can be used interchangeably.

NONLINEAR ANTENNAS BASED ON ENZ MATERIALS

Let us consider a nonlinear antenna made of indium tin oxide (ITO; see the inset of Figure 1b). The antenna is illuminated

Received: October 22, 2020
Published: February 1, 2021

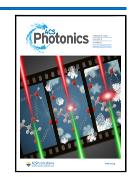

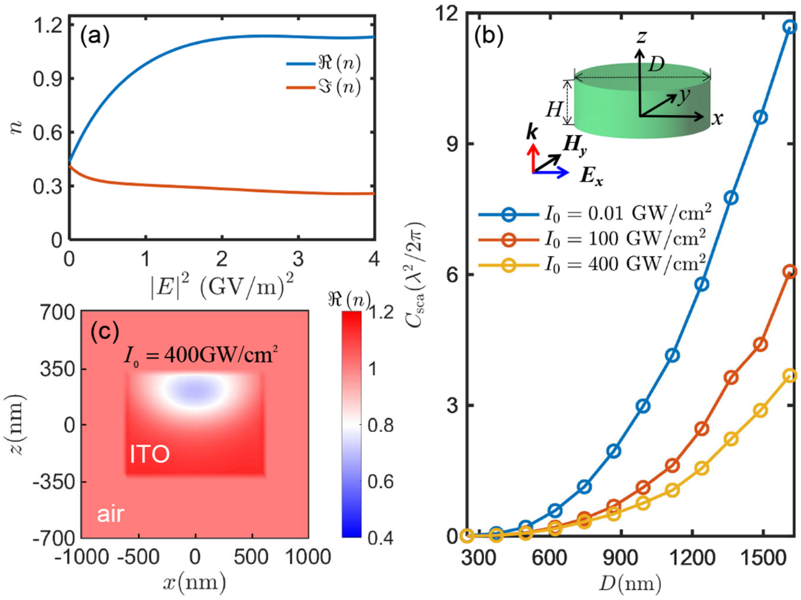

Figure 1. Nonlinear antenna based on epsilon-near-zero (ENZ) material: (a) The real and imaginary parts of the intensity-dependent refractive index of ITO at the ENZ wavelength λ_{ENZ} = 1240 nm (see ref 21). (b) Scattering cross section (normalized to $\lambda^2/2\pi$) of the ITO antenna at the ENZ wavelength as a function of the diameter of the antenna D for different intensities. Note that the lowest intensity, that is, I_0 = 0.01 GW/cm^2, corresponds to the linear response of the antenna. Inset shows a schematic of the ITO disk with height H and diameter D. The ITO antenna is illuminated by an x-polarized plane wave propagating in the z direction. (c) The real part of refractive index in the xz-plane (at y = 0) at the highest intensity, that is, I_0 = 400 GW/cm^2. We assume that the height of the ITO antenna is $H = D/2$ and the surrounding medium is air.

by an x-polarized time-harmonic plane wave with electric field $\mathbf{E}_{inc}(t) = (E_0/2)e^{i(\mathbf{k}\cdot\mathbf{r}-\omega t)}\mathbf{e}_x$ + c.c., where $|\mathbf{k}| = 2\pi/\lambda$ is the wavenumber, ω is the angular frequency, E_0 is the amplitude of incident field, and c.c. means complex conjugate. $I_0 = \frac{1}{2}c\varepsilon_0|E_0|^2$ is the free-space intensity of the incident plane wave. The intensity-dependent refractive index of ITO is $n_{NL}(\mathbf{r}, \omega) = \sqrt{\varepsilon_{NL}(\mathbf{r}, \omega)}$, where $\varepsilon_{NL}(\mathbf{r},\omega)$ is given by[21,43]

$$\varepsilon_{NL}(\mathbf{r}, \omega) \approx \varepsilon_L + \sum_{j=1}^{3} c_{2j+1}\chi^{(2j+1)}(\omega)\left|\frac{\mathbf{E}(\mathbf{r}, \omega)}{2}\right|^{2j} \tag{1}$$

and where $\chi^{(3)}(\omega)$, $\chi^{(5)}(\omega)$, and $\chi^{(7)}(\omega)$ are the third-order, fifth-order, and seventh-order nonlinear susceptibilities (see Table 1 in ref 21) of ITO, respectively. $c_3 = 3$, $c_5 = 10$, and $c_7 = 35$ are the degeneracy factors,[43] and $\mathbf{E}(\mathbf{r},\omega)$ is the electric field amplitude inside ITO.

The real part of the permittivity of ITO is zero at λ_{ENZ} = 1240 nm, which is called the ENZ wavelength. It has been shown that ITO exhibits a large nonlinear refractive index around its ENZ wavelength.[17,20,21] Figure 1a plots the real and imaginary parts of the intensity-dependent refractive index of the ITO film at λ_{ENZ}.[17,21] Note that the change in the real part of the refractive index by intensity is approximately 0.72, which is even larger than the linear refractive index of ITO, which is 0.4. In the following, we incorporate this large nonlinear response of ITO at the ENZ wavelength and perform our simulations using a Maxwell's equations numerical solver combined with an iterative method to solve for an intensity-dependent refractive index inside the antenna.

In order to understand the optical response of the proposed nonlinear antennas, we employ multipole expansion of the induced nonlinear (intensity-dependent) polarization current $\mathbf{J}_{NL}(\mathbf{r},\omega) = -i\omega[\varepsilon_{NL}(\mathbf{r},\omega) - \varepsilon_0]\mathbf{E}(\mathbf{r},\omega)$.[4,44] Through use of the induced multipole moments, the total scattering cross section of the nonlinear ITO antenna can be calculated by[4,44]

$$C_{sca} = \frac{k^4}{6\pi\varepsilon_0^2|E_0|^2}\left[\sum_{\alpha}\left(|p_\alpha|^2 + \left|\frac{m_\alpha}{c}\right|^2\right) + \sum_{\alpha,\beta}\left(\left|kQ^e_{\alpha\beta}\right|^2 + \left|\frac{kQ^m_{\alpha\beta}}{c}\right|^2\right)\right] \tag{2}$$

as a sum of contribution of each multipole moment to the total scattering cross section. $\alpha,\beta = x,y,z$, and p_α, m_α, $Q^e_{\alpha\beta}$, and $Q^m_{\alpha\beta}$ are the electric dipole (ED), magnetic dipole (MD), electric quadrupole (EQ), and magnetic quadrupole (MQ) moments.

Figure 1b shows the scattering cross section (normalized to $\lambda^2/2\pi$) of the ITO disk as a function of its diameter D for three different intensities. It can be seen that the scattering cross section gradually increases as D increases. At high intensities, for example, I_0 = 400 GW/cm^2, the scattering cross section is approximately 4× smaller than the linear response, that is, I_0 = 0.01 GW/cm^2 (see Supporting Information). At high intensities, the refractive index of ITO is close to the refractive index of the surrounding medium (air), and thus, scattering becomes smaller than that of low intensities (Figure 1a,c). These results can also be understood in terms of the induced electric and magnetic multipole moments (see Supporting Information for details). In Figure 1c, we plot the real part of the refractive index of the ITO antenna in the xz-plane. The refractive index depends on position $\mathbf{r}$ because of the induced nonuniform electric field distribution inside the antenna, that is, $\mathbf{E}(\mathbf{r})$ (see also eq 1).

Figure 2a shows the total scattering cross section and contributions of the electric and magnetic multipole moments as a function of intensity. Although the contribution of the ED moment is significantly larger than any other modes, the antenna radiates mainly in the forward direction because of the presence of higher order moments (Figure 2a,b). The

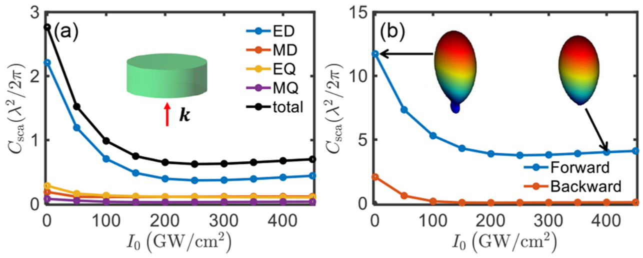

Figure 2. Intensity-dependent response of a nonlinear antenna: (a) Total scattering cross section (normalized to $\lambda^2/2\pi$) and contribution of different electric and magnetic multipole moments as a function of the input intensity for the ITO antenna. Contribution of different multipoles are labeled by ED (electric dipole), MD (magnetic dipole), EQ (electric quadrupole), and MQ (magnetic quadrupole). The geometrical parameters of the ITO antenna are $D = 0.8\lambda_{ENZ}$ and $H = D/2$. (b) Normalized forward and backward scattering cross sections calculated from eq 3. The insets illustrate normalized far-field radiation patterns of the ITO antenna for low and high intensities.

normalized forward C^{F}_{sca} and backward C^{B}_{sca} scattering cross sections are plotted in Figure 2b, which are calculated from[7]

$$C^{F/B}_{sca} = C_{norm}\left|p_x \pm \frac{m_y}{c} \mp \frac{ikQ^{e}_{xz}}{6} - \frac{ikQ^{m}_{yz}}{6c}\right|^2 \qquad (3)$$

where $C_{norm} = k^4/(4\pi\varepsilon_0^2|E_0|^2)$. In eq 3, the forward and backward scattering cross sections are calculated at $\phi_{F/B} = 0$ and $\theta_{F/B} = 0,\pi$. Note that the ED (and similarly MQ) moment exhibits in-phase forward and backward scattered electric fields, whereas the MD (and similarly EQ) moment shows out-of-phase fields (see $\pm$ in eq 3). As the intensity of the laser increases, the contribution of different multipoles changes. Consequently, the antenna radiates solely in the forward direction at high intensities, which is clearly evident from the inset of Figure 2b.

SUPERABSORPTION AND SUPERSCATTERING IN NONLINEAR ANTENNAS

The maximum scattering cross section (for each multipolar order) of an isotropic nanoparticle with multipolar response is $C^{max}_{sca,j} = (2j + 1)\lambda^2/2\pi$, where j is the order of the multipole; for example, $j = 1$, 2, and 3, for dipoles, quadrupoles, and octupoles, respectively.[8,9,11,13,45,46] For each multipolar order, the maximum scattering occurs at the resonance for a particle with negligible Ohmic losses compared to the radiation loss (this condition is known as overcoupling).[8,9,11,13,45−48] By engineering subwavelength nanoparticles, it is possible to achieve a much larger scattering cross section compared to a dipolar one, that is, $C^{max}_{sca,1} = 3\lambda^2/2\pi$. This phenomenon is known as superscattering and is achieved by overlapping resonant frequencies of different multipoles.[8,9,12,13] It has also been shown that the maximum absorption cross section of a nanoparticle with multipolar response is limited to $C^{max}_{abs,j} = C^{max}_{sca,j}/4 = (2j + 1)\lambda^2/8\pi$.[11−13,46] The enhanced absorption can be achieved for particles that operate at critical coupling (i.e., nonradiative or Ohmic loss is equal to the radiation loss) and by aligning the resonance frequencies of different multipoles. This enhanced absorption cross section is known as superabsorption.[8,9]

Here, we show that scattering and absorption cross sections of an ITO antenna can be tuned between nearly superscattering and nearly superabsorbing states by simply changing the input laser intensity. Figure 3a,b shows scattering and absorption cross sections of our ITO antenna as a function of

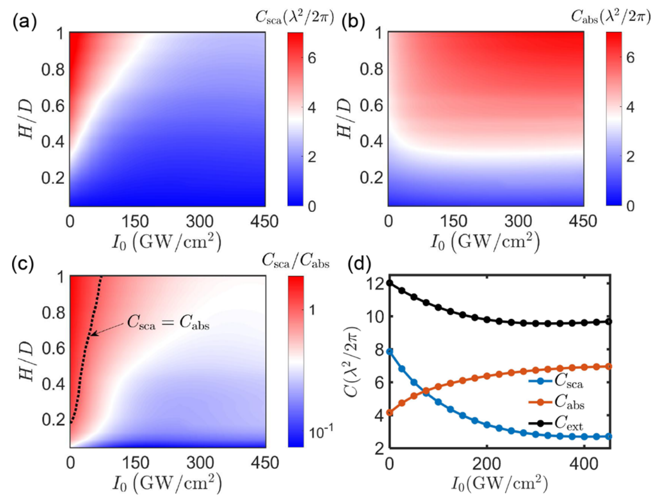

Figure 3. Tunable superabsorption and superscattering based on an ITO antenna: (a) Total scattering cross section C_{sca} (normalized to $\lambda^2/2\pi$) of the ITO antenna (see the inset of Figure 1b) as a function of height-to-diameter ratios, H/D, and the laser intensity I_0, where the diameter of the antenna $D = 1200$ nm. (b) Same as (a) for the absorption cross section, that is, C_{abs}. (c) The ratio between the scattering and absorption cross sections shown in logarithmic scale. The black dashed line indicates the condition that the scattering and absorption cross sections are equal, that is, $C_{sca} = C_{abs}$. (d) Scattering, absorption, and extinction cross sections as functions of intensity I_0 for $H = D = 1200$ nm.

the laser intensity for different height-to-diameter ratios, H/D. For low intensities and $H/D = 1$, the scattering cross section is $C_{sca} \approx 2.7 \times 3\lambda^2/2\pi$, which is 2.7× larger than the maximum scattering of a dipole. By increasing the laser intensity, the absorption cross section increases and reaches to $C_{abs} \approx 9.3 \times 3\lambda^2/8\pi$, which is significantly larger than that of a dipolar scatterer. Therefore, the ITO antenna behaves as a superscatterer at low intensities and as a superabsorber at high intensities. This behavior can be seen clearly from Figure 3d, which plots the scattering, absorption, and extinction cross sections as a function of intensity for $H = D = 1200$ nm. The ratio of the scattering to the absorption cross section is depicted in Figure 3c (the induced electric and magnetic multipole moments of the antenna are shown in Supporting Information). Three distinct coupling regimes are evident: (i) a large scattering cross section compared to absorption, that is, $C_{sca} > C_{abs}$, the area to the left of the black dashed line, (ii) scattering is identical to absorption cross section, that is, $C_{sca} = C_{abs}$, as indicated by the black dashed line in Figure 3c, and (iii) a large absorption cross section compared to scattering, that is, $C_{abs} > C_{sca}$, the area to the right of the black dashed line.

HYBRID NONRECIPROCAL NONLINEAR ANTENNAS

Dielectric antennas support strong electric and magnetic responses with large scattering cross sections.[45,49,50] Thus, to achieve an even greater control on the scattering properties of ITO antennas, one can devise a nonlinear antenna composed of ENZ and lossless dielectric materials. In the following, we consider a hybrid nonlinear antenna made of an ITO and a lossless linear dielectric material with refractive index n_L, as shown in the inset of Figure 4a. Due to the broken inversion symmetry, the hybrid antenna exhibits magneto−electric coupling or the so-called bianisotropic response.[51−53]

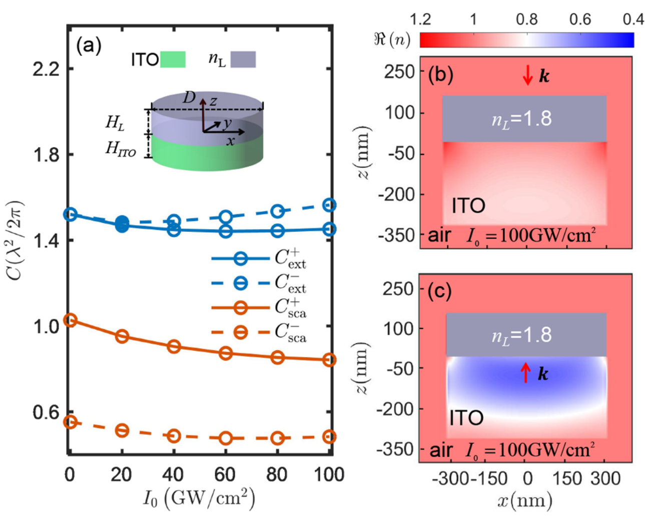

Figure 4. Hybrid nonlinear antenna composed of ITO and a lossless linear dielectric material with refractive index n_L = 1.8: (a) Total extinction ($C^{\pm}_{ext}$) and scattering ($C^{\pm}_{sca}$) cross sections (normalized to $\lambda^2/2\pi$) of the hybrid antenna as a function of the laser intensity when illuminated by an x-polarized plane wave propagating in two opposite directions, that is, $\mathbf{k} = \pm k_0\mathbf{e}_z$. Inset shows the schematic of the hybrid nonlinear antenna. (b, c) The real part of refractive index in xz-plane (at y = 0) at intensity I_0 = 100 GW/cm^2 for top ($\mathbf{k} = -k_0\mathbf{e}_z$) and bottom ($\mathbf{k} = +k_0\mathbf{e}_z$) illuminations, respectively. The surrounding medium is air. The geometrical parameters of the hybrid nonlinear antenna are $D_{ITO} = D_L = D$ = 620 nm, $H_{ITO} = D_{ITO}/2$, and H_L = 150 nm.

According to the optical theorem and the Lorentz reciprocity, the extinction cross section of an arbitrarily shaped antenna made of reciprocal materials is the same for two opposite illumination directions.[52,54−56] However, the scattering and absorption cross sections of the reciprocal antenna depend on the illumination direction due to absorption (Ohmic) losses which are related to the induced bianisotropic response.[52,56] In Figure 4a we plot the extinction and scattering cross sections of the hybrid antenna when illuminated from opposite directions ($\mathbf{k} = \pm k_0\mathbf{e}_z$). In the linear regime (low intensities), the antenna is reciprocal. Therefore, the extinction cross section for top and bottom illuminations are identical, that is, $C^+_{ext} = C^-_{ext}$.[52,56] However, the scattering (and also the absorption) cross sections of the antenna are different, $C^+_{sca} \neq C^-_{sca}$.

At high laser intensities, the hybrid antenna is nonreciprocal and two conditions to break the Lorentz reciprocity are simultaneously satisfied, that is, the large optical nonlinearity and lack of inversion symmetry.[57] Thus, as shown in Figure 4a, the extinction cross sections of the antenna are not the same for the two opposite illuminations at high intensities. Figure 4b,c shows the real part of the refractive index in the xz-plane for I_0 = 100 GW/cm^2 and indicate a position-dependent refractive index. Clearly, the refractive indices are different for opposite illuminations: $n^+_{NL}(\mathbf{r}) \neq n^-_{NL}(\mathbf{r})$. The different distribution of the refractive indices (Figure 4b,c) leads to a magneto-electric coupling (see ref 52 for a magneto−electric coupling in a reciprocal antenna). To understand the underlying physics of the asymmetric nonreciprocal response and magneto-electric coupling, we compute the induced multipole moments using the exact multipole expansion for the opposite illuminations (see Figure 5a,b). The induced

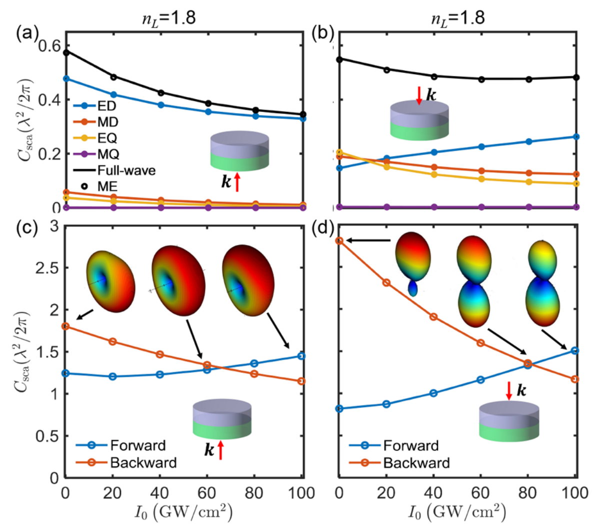

Figure 5. Scattering and radiation patterns of hybrid nonlinear antennas: (a) Total scattering cross section (normalized to $\lambda^2/2\pi$) and contribution of different electric and magnetic multipole moments of the hybrid antenna as a function of the laser intensity for the bottom illumination direction, that is, $\mathbf{k} = +k_0\mathbf{e}_z$. (c) Normalized forward (blue line) and backward (red line) scattering cross sections calculated from eq 3 for the bottom illumination direction. Insets illustrate far-field radiation patterns of hybrid nonlinear antenna in three intensities for the bottom illumination direction, that is, $\mathbf{k} = +k_0\mathbf{e}_z$. (b, d) Same as (a) and (c) for the top illumination direction, that is, $\mathbf{k} = -k_0\mathbf{e}_z$.

multipole moments are significantly different for the top and bottom illuminations which lead to intensity-dependent magneto-electric coupling. Note that the scattering cross sections calculated using full-wave simulation as well as multipole expansion (ME) are in perfect agreement (see the black solid line and circles in Figure 5a,b). Therefore, our proposed nonlinear scatterer can be fully characterized by using the dipole and quadrupole moments.

When the hybrid antenna is illuminated from the bottom, the antenna exhibits mainly an electric dipole (ED) moment, as can be seen in Figure 5a. Therefore, the radiation pattern of hybrid antenna is nearly omnidirectional (see the inset of Figure 5c). The contribution of other multipole moments to the forward and backward cross sections are small compared to the ED moment and thus slightly modify the radiation patterns.

When the hybrid antenna is illuminated from the top, compared to the bottom illumination, different multipole moments contribute to the scattering (compare Figure 5a and b). However, similar to the bottom illumination, the backward (forward) scattering decreases (increases) with the intensity, as shown in Figure 5d. In the linear regime (low intensities), the induced ED, MD, and EQ moments interfere constructively (destructively) in the backward (forward) direction. Consequently, the antenna exhibits a nearly unidirectional radiation pattern with a very small forward scattering (see Figure 5d). At $I_0 \approx$ 80 GW/cm^2, the forward and backward scattering become identical. In the Supporting Information, we show that a hybrid antenna with n_L = 3.5 exhibits a unidirectional radiation pattern with nearly zero backward scattering. This phenomena is known as the generalized Kerker effect.[7,58] Large tunability of the induced multipole moments of the hybrid antenna by an intense pump laser allows to control the radiation patterns from a bidirectional to a unidirectional pattern (compare three radiation patterns in the inset of Figure 5d). Therefore, by employing an ultrafast optical pump,[17] the radiation pattern of the hybrid antenna can be switched from a nondirective radiation to a directive one within a subpicosecond time scale. Moreover, the hybrid antenna exhibits nonreciprocal radiation patterns because of nonreciprocal magneto-electric coupling.

In summary, we have theoretically studied nonlinear antennas based on ENZ materials with tunable absorption and scattering cross sections, as well as radiation patterns. We incorporated the extremely large and ultrafast nonlinear response of ENZ materials, in particular, ITO. We showed that while the radiation pattern of a single ITO antenna remains insensitive to the laser intensity, its absorption, scattering, and extinction cross sections can be modulated dynamically. Therefore, the antenna can be tuned between superabsorbing and superscattering states by controlling the intensity of the laser. Furthermore, we proposed a hybrid antenna (composed of ITO and a dielectric material) with a radiation pattern that can be tuned between bidirectional and unidirectional emission under ultrafast optical pumping. Moreover, we found that the hybrid nanoantenna exhibits tunable nonreciprocal radiation patterns when illuminated from opposite directions because of the broken spatial inversion symmetry and large optical nonlinearity of ITO. We explained our findings based on the interference among the induced intensity-dependent electric and magnetic multipole moments. Considering the fast response-time of ITO, a typical 100 fs pulsed laser can be used to achieve the required intensities experimentally.[17,26] The proposed tunable hybrid antenna with magneto-electric response can be used as a building block to design ultrafast switchable nonreciprocal electric and magnetic mirrors,[57,59] metalens,[57] metaabsorbers,[48,60] metagrating,[61] and photonic topological insulators.[62] In addition, our work provides a novel approach for designing tunable nanoantennas based on ENZ materials with a large optical nonlinearity.

■ ASSOCIATED CONTENT

Supporting Information

The Supporting Information is available free of charge at https://pubs.acs.org/doi/10.1021/acsphotonics.0c01637.

> We present expressions for the exact induced multipole moments in Cartesian coordinates, the corresponding scattering cross sections, and the intensity-dependent refractive index, and the multipole moments for the superabsorption and superscattering states (PDF)

■ AUTHOR INFORMATION

Corresponding Author

Rasoul Alaee − *Department of Physics, University of Ottawa,*

Authors

Lin Cheng − *Department of Physics, University of Ottawa, Ottawa, Ontario K1N 6N5, Canada; Key Laboratory of Physical Electronics and Devices of Ministry of Education, School of Electronic Science and Engineering, Xi'an Jiaotong University, Xi'an 710049, China*

Akbar Safari − *Department of Physics, University of Ottawa, Ottawa, Ontario K1N 6N5, Canada*

Mohammad Karimi − *Department of Physics, University of Ottawa, Ottawa, Ontario K1N 6N5, Canada*

Lei Zhang − *Key Laboratory of Physical Electronics and Devices of Ministry of Education, School of Electronic Science and Engineering, Xi'an Jiaotong University, Xi'an 710049, China;* orcid.org/0000-0002-5113-1786

Robert W. Boyd − *Department of Physics, University of Ottawa, Ottawa, Ontario K1N 6N5, Canada; The Institute of Optics, University of Rochester, Rochester, New York 14627, United States;* orcid.org/0000-0002-1234-2265

Complete contact information is available at: https://pubs.acs.org/10.1021/acsphotonics.0c01637

Author Contributions

‖These authors contributed equally to this work.

Notes

The authors declare no competing financial interest.

■ ACKNOWLEDGMENTS

R.A. acknowledges the support of the Alexander von Humboldt Foundation through the Feodor Lynen Fellowship. L.C. acknowledges the support of China Scholarship Council. L.C., R.A., A.S., M.K., and R.W.B. are grateful to M. Zahirul Alam, Orad Reshef, Boris Braverman, and Jeremy Upham for helpful discussions and acknowledge support through the Natural Sciences and Engineering Research Council of Canada, the Canada Research Chairs program, and the Canada First Research Excellence Fund. R.W.B. also acknowledges support from the U.S. Army Research Office and the U.S. Defense Advanced Research Projects Administration. R.A. would like to thank Orad Reshef for providing data for Figure 1a.

■ REFERENCES

(1) Bharadwaj, P.; Deutsch, B.; Novotny, L. Optical antennas. *Adv. Opt. Photonics* **2009**, *1*, 438−483.

(2) Taylor, R. W.; Sandoghdar, V. *Label-Free Super-Resolution Microscopy*; Springer, 2019; pp 25−65.

(3) Krasnok, A.; Tymchenko, M.; Alù, A. Nonlinear metasurfaces: a paradigm shift in nonlinear optics. *Mater. Today* **2018**, *21*, 8−21.

(4) Alaee, R.; Rockstuhl, C.; Fernandez-Corbaton, I. Exact multipolar decompositions with applications in nanophotonics. *Adv. Opt. Mater.* **2019**, *7*, 1800783.

(5) Kerker, M.; Wang, D.-S.; Giles, C. Electromagnetic scattering by magnetic spheres. *J. Opt. Soc. Am.* **1983**, *73*, 765−767.

(6) Zambrana-Puyalto, X.; Fernandez-Corbaton, I.; Juan, M.; Vidal, X.; Molina-Terriza, G. Duality symmetry and Kerker conditions. *Opt. Lett.* **2013**, *38*, 1857−1859.

(7) Alaee, R.; Filter, R.; Lehr, D.; Lederer, F.; Rockstuhl, C. A generalized Kerker condition for highly directive nanoantennas. *Opt. Lett.* **2015**, *40*, 2645−2648.

(8) Ruan, Z.; Fan, S. Superscattering of light from subwavelength nanostructures. *Phys. Rev. Lett.* **2010**, *105*, No. 013901.

(9) Ruan, Z.; Fan, S. Design of subwavelength superscattering nanospheres. *Appl. Phys. Lett.* **2011**, *98*, 043101.

(10) Ng, J.; Chen, H.; Chan, C. T. Metamaterial frequency-selective superabsorber. *Opt. Lett.* **2009**, *34*, 644−646.

(11) Miroshnichenko, A. E.; Tribelsky, M. I. Ultimate absorption in light scattering by a finite obstacle. *Phys. Rev. Lett.* **2018**, *120*, No. 033902.

(12) Estakhri, N. M.; Alu, A. Minimum-scattering superabsorbers. *Phys. Rev. B: Condens. Matter Mater. Phys.* **2014**, *89*, 121416.
(13) Rahimzadegan, A.; Alaee, R.; Fernandez-Corbaton, I.; Rockstuhl, C. Fundamental limits of optical force and torque. *Phys. Rev. B: Condens. Matter Mater. Phys.* **2017**, *95*, No. 035106.
(14) Alù, A.; Engheta, N. Multifrequency Optical Invisibility Cloak with Layered Plasmonic Shells. *Phys. Rev. Lett.* **2008**, *100*, 113901.
(15) Devaney, A. J.; Wolf, E. Radiating and Nonradiating Classical Current Distributions and the Fields They Generate. *Phys. Rev. D: Part. Fields* **1973**, *8*, 1044−1047.
(16) Hsu, C. W.; DeLacy, B. G.; Johnson, S. G.; Joannopoulos, J. D.; Soljacic, M. Theoretical criteria for scattering dark states in nanostructured particles. *Nano Lett.* **2014**, *14*, 2783−2788.
(17) Alam, M. Z.; De Leon, I.; Boyd, R. W. Large optical nonlinearity of indium tin oxide in its epsilon-near-zero region. *Science* **2016**, *352*, 795−797.
(18) Argyropoulos, C.; Chen, P.-Y.; D'Aguanno, G.; Engheta, N.; Alù, A. Boosting optical nonlinearities in ϵ-near-zero plasmonic channels. *Phys. Rev. B: Condens. Matter Mater. Phys.* **2012**, *85*, No. 045129.
(19) Kinsey, N.; DeVault, C.; Kim, J.; Ferrera, M.; Shalaev, V.; Boltasseva, A. Epsilon-near-zero Al-doped ZnO for ultrafast switching at telecom wavelengths. *Optica* **2015**, *2*, 616−622.
(20) Caspani, L.; Kaipurath, R. P. M.; Clerici, M.; Ferrera, M.; Roger, T.; Kim, J.; Kinsey, N.; Pietrzyk, M.; Di Falco, A.; Shalaev, V. M.; Boltasseva, A.; Faccio, D. Enhanced Nonlinear Refractive Index in ϵ-Near-Zero Materials. *Phys. Rev. Lett.* **2016**, *116*, 233901.
(21) Reshef, O.; Giese, E.; Alam, M. Z.; De Leon, I.; Upham, J.; Boyd, R. W. Beyond the perturbative description of the nonlinear optical response of low-index materials. *Opt. Lett.* **2017**, *42*, 3225−3228.
(22) Liberal, I.; Engheta, N. Near-zero refractive index photonics. *Nat. Photonics* **2017**, *11*, 149.
(23) Clerici, M.; Kinsey, N.; DeVault, C.; Kim, J.; Carnemolla, E. G.; Caspani, L.; Shaltout, A.; Faccio, D.; Shalaev, V.; Boltasseva, A.; Ferrera, M. Controlling hybrid nonlinearities in transparent conducting oxides via two-colour excitation. *Nat. Commun.* **2017**, *8*, 1−7.
(24) Ferrera, M.; Kinsey, N.; Shaltout, A.; DeVault, C.; Shalaev, V.; Boltasseva, A. Dynamic nanophotonics. *J. Opt. Soc. Am. B* **2017**, *34*, 95−103.
(25) Liberal, I.; Engheta, N. The rise of near-zero-index technologies. *Science* **2017**, *358*, 1540−1541.
(26) Alam, M. Z.; Schulz, S. A.; Upham, J.; De Leon, I.; Boyd, R. W. Large optical nonlinearity of nanoantennas coupled to an epsilon-near-zero material. *Nat. Photonics* **2018**, *12*, 79.
(27) Vezzoli, S.; Bruno, V.; DeVault, C.; Roger, T.; Shalaev, V. M.; Boltasseva, A.; Ferrera, M.; Clerici, M.; Dubietis, A.; Faccio, D. Optical time reversal from time-dependent Epsilon-Near-Zero media. *Phys. Rev. Lett.* **2018**, *120*, No. 043902.
(28) Kim, J.; Carnemolla, E. G.; DeVault, C.; Shaltout, A. M.; Faccio, D.; Shalaev, V. M.; Kildishev, A. V.; Ferrera, M.; Boltasseva, A. Dynamic control of nanocavities with tunable metal oxides. *Nano Lett.* **2018**, *18*, 740−746.
(29) Niu, X.; Hu, X.; Chu, S.; Gong, Q. Epsilon-Near-Zero Photonics: A New Platform for Integrated Devices. *Adv. Opt. Mater.* **2018**, *6*, 1701292.
(30) Reshef, O.; De Leon, I.; Alam, M. Z.; Boyd, R. W. Nonlinear optical effects in epsilon-near-zero media. *Nature Reviews Materials* **2019**, *4*, 535−551.
(31) Kinsey, N.; DeVault, C.; Boltasseva, A.; Shalaev, V. M. Near-zero-index materials for photonics. *Nature Reviews Materials* **2019**, *4*, 742−760.
(32) Alaee, R.; Vaddi, Y.; Boyd, R. W. Dynamic coherent perfect absorption in nonlinear metasurfaces. *Opt. Lett.* **2020**, *45*, 6414−6417.
(33) Bruno, V.; et al. Negative Refraction in Time-Varying Strongly Coupled Plasmonic-Antenna−Epsilon-Near-Zero Systems. *Phys. Rev. Lett.* **2020**, *124*, No. 043902.
(34) Paul, J.; Miscuglio, M.; Gui, Y.; Sorger, V.; Wahlstrand, J. Two-beam coupling by a hot electron nonlinearity. *Opt. Lett.* **2021**, *46*, 428.
(35) Bruno, V.; Vezzoli, S.; DeVault, C.; Roger, T.; Ferrera, M.; Boltasseva, A.; Shalaev, V. M.; Faccio, D. Dynamical control of broadband coherent absorption in ENZ films. *Micromachines* **2020**, *11*, 110.
(36) Bruno, V.; Vezzoli, S.; DeVault, C.; Carnemolla, E.; Ferrera, M.; Boltasseva, A.; Shalaev, V. M.; Faccio, D.; Clerici, M. Broad frequency shift of parametric processes in epsilon-near-zero time-varying media. *Appl. Sci.* **2020**, *10*, 1318.
(37) Lapshina, N.; Noskov, R.; Kivshar, Y. S. Nonlinear nano-antenna with self-tunable scattering pattern. *JETP Lett.* **2013**, *96*, 759−764.
(38) Smirnova, D.; Kivshar, Y. S. Multipolar nonlinear nano-photonics. *Optica* **2016**, *3*, 1241−1255.
(39) Camacho-Morales, R.; Rahmani, M.; Kruk, S.; Wang, L.; Xu, L.; Smirnova, D. A.; Solntsev, A. S.; Miroshnichenko, A.; Tan, H. H.; Karouta, F.; et al. Nonlinear generation of vector beams from AlGaAs nanoantennas. *Nano Lett.* **2016**, *16*, 7191−7197.
(40) Smirnova, D.; Kruk, S.; Leykam, D.; Melik-Gaykazyan, E.; Choi, D.-Y.; Kivshar, Y. Third-Harmonic Generation in Photonic Topological Metasurfaces. *Phys. Rev. Lett.* **2019**, *123*, 103901.
(41) Smirnova, D.; Smirnov, A. I.; Kivshar, Y. S. Multipolar second-harmonic generation by Mie-resonant dielectric nanoparticles. *Phys. Rev. A: At., Mol., Opt. Phys.* **2018**, *97*, No. 013807.
(42) Carletti, L.; Koshelev, K.; De Angelis, C.; Kivshar, Y. Giant Nonlinear Response at the Nanoscale Driven by Bound States in the Continuum. *Phys. Rev. Lett.* **2018**, *121*, No. 033903.
(43) Boyd, R. W. *Nonlinear Optics*; Academic Press, 2019.
(44) Alaee, R.; Rockstuhl, C.; Fernandez-Corbaton, I. An electro-magnetic multipole expansion beyond the long-wavelength approx-imation. *Opt. Commun.* **2018**, *407*, 17−21.
(45) Bohren, C. F.; Huffman, D. R. *Absorption and Scattering of Light by Small Particles*; John Wiley & Sons, 2008.
(46) Tribelsky, M. I.; Luk'yanchuk, B. S. Anomalous light scattering by small particles. *Phys. Rev. Lett.* **2006**, *97*, 263902.
(47) Tribelskii, M. Resonant scattering of light by small particles. *Sov. Phys. JETP* **1984**, *59*, 534−536.
(48) Alaee, R.; Albooyeh, M.; Rockstuhl, C. Theory of metasurface based perfect absorbers. *J. Phys. D: Appl. Phys.* **2017**, *50*, 503002.
(49) Evlyukhin, A. B.; Novikov, S. M.; Zywietz, U.; Eriksen, R. L.; Reinhardt, C.; Bozhevolnyi, S. I.; Chichkov, B. N. Demonstration of magnetic dipole resonances of dielectric nanospheres in the visible region. *Nano Lett.* **2012**, *12*, 3749−3755.
(50) Kuznetsov, A. I.; Miroshnichenko, A. E.; Fu, Y. H.; Zhang, J.; Luk'Yanchuk, B. Magnetic light. *Sci. Rep.* **2012**, *2*, 492.
(51) Tretyakov, S. *Analytical Modeling in Applied Electromagnetics*; Artech House, 2003.
(52) Alaee, R.; Albooyeh, M.; Rahimzadegan, A.; Mirmoosa, M. S.; Kivshar, Y. S.; Rockstuhl, C. All-dielectric reciprocal bianisotropic nanoparticles. *Phys. Rev. B: Condens. Matter Mater. Phys.* **2015**, *92*, 245130.
(53) Asadchy, V. S.; Díaz-Rubio, A.; Tretyakov, S. A. Bianisotropic metasurfaces: physics and applications. *Nanophotonics* **2018**, *7*, 1069−1094.
(54) Newton, R. G. Optical theorem and beyond. *Am. J. Phys.* **1976**, *44*, 639−642.
(55) Harrington, R. F. *Time-Harmonic Electromagnetic Fields*; IEEE, 2001; pp 168−171,
(56) Sounas, D. L.; Alù, A. Extinction symmetry for reciprocal objects and its implications on cloaking and scattering manipulation. *Opt. Lett.* **2014**, *39*, 4053−4056.
(57) Asadchy, V. S.; Mirmoosa, M. S.; Díaz-Rubio, A.; Fan, S.; Tretyakov, S. A. Tutorial on Electromagnetic Nonreciprocity and Its Origins. *Proc. IEEE* **2020**, *108*, 1684−1727.
(58) Liu, W.; Kivshar, Y. S. Generalized Kerker effects in nanophotonics and meta-optics. *Opt. Express* **2018**, *26*, 13085−13105.

(59) Asadchy, V. S.; Ra'di, Y.; Vehmas, J.; Tretyakov, S. A. Functional Metamirrors Using Bianisotropic Elements. *Phys. Rev. Lett.* **2015**, *114*, No. 095503.
(60) Ra'di, Y.; Simovski, C.; Tretyakov, S. Thin perfect absorbers for electromagnetic waves: theory, design, and realizations. *Phys. Rev. Appl.* **2015**, *3*, No. 037001.
(61) Ra'di, Y.; Sounas, D. L.; Alù, A. Metagratings: Beyond the limits of graded metasurfaces for wave front control. *Phys. Rev. Lett.* **2017**, *119*, No. 067404.
(62) Slobozhanyuk, A.; Mousavi, S. H.; Ni, X.; Smirnova, D.; Kivshar, Y. S.; Khanikaev, A. B. Three-dimensional all-dielectric photonic topological insulator. *Nat. Photonics* **2017**, *11*, 130−136.

Chapter 6

Conclusion

Throughout this thesis, we investigated the nature and applications of the large and fast nonlinear response of indium-tin-oxide (ITO) around the epsilon-near-zero (ENZ) wavelength of this material, where the real part of permittivity vanishes. In the introduction section, we first elaborated on the importance of the research in nonlinear optics in general and the nonlinear Kerr effect in particular. We mentioned how the small magnitude of the nonlinear refractive index, which parametrizes the Kerr effect strength, limits the application of Kerr nonlinear materials in many applications. We then discussed the critical role of time-varying optical systems in the development of new technologies and how materials with faster response times are required to push the boundaries of such technologies. After elaborating on the importance of highly nonlinear materials with fast response times, we gave a background on the nonlinear response of ITO and how the refractive index of this material can be modified by an amount as large as the linear refractive index in a sub-picosecond time scale in response to a strong enough pump pulse.

The first project we investigated in Chapter 2 was how to use this large fast nonlinear effect for adiabatic wavelength conversion. We triggered the nonlinear response in a 620-nm layer of ITO with a pump pulse of duration 100 femtosecond (fs) with a wavelength around the ENZ point in the infra-red range while a degenerate probe beam of much lower power was witnessing the nonlinear response. We expected that the large modification of the refractive index of the ITO layer in a sub-picosecond time scale would lead to a large time refraction, which, consequently, leads to a considerable conversion of the wavelength of the probe. We showed experimentally that the probe beam goes under a record-breaking amount of conversion in wavelength due to the large slope of the refractive index with respect to time.

The adiabatic wavelength conversion project can be followed up in many ways. It is intuitive to think that by increasing the interaction time between the beam and the triggered ITO, the amount of wavelength conversion increases. We can demand the interaction time of the beam with the material to increase by putting it in a cavity. A simple version of a cavity can be created by adding back-reflecting planes with simple metals or layered brag reflectors at each side of the ITO layer. A more complicated cavity can be made using metasurfaces with high Q factors, although the non-negligible imaginary part of the permittivity of ITO at the ENZ region makes the design of such a metasurface a challenge. Moreover, Studying the impact of refractive index changes on wavelength conversion through varying excitation pulse durations adds value, as it enables exploration of how the rate of modifications to the refractive index influences the extent of wavelength conversion.

In Chapter 3, we designed, fabricated, and tested a gradient metasurface on ITO to make a scheme for spatiotemporal manipulation of light. We demonstrated that the scheme can be used for all-optical beam steering by combining the adiabatic wavelength conversion of ITO and the diffraction pattern of the gradient metasurface. We characterized the samples in a pump-probe experimental set-up where an intense pump beam of light triggers the nonlinear response of ITO, and a probe beam diffracts from the metasurface while sensing the fast modulation of the refractive index. As a result, the wavelength of the probe beam converts, and the new wavelengths diffract to new angles. The device was a proof of principle, and there are ways to improve the efficiency of diffraction and the amount of steering. One way that may make both of these improvements simultaneously is to add a back reflecting plane beneath the ITO or over the grating. The additional mode that can be excited in the space between the backplane and the metasurface helps to improve the phase ramp over each unit cell of the metasurface, which improves the diffraction efficiency. It can also make a simple cavity that increases the interaction time between the beam and the sample, which leads to larger wavelength conversion and, consequently, a larger steering angle. The asymmetric nonlinear response of the diffraction orders is another fact that can be investigated further regarding that project.

In Chapter 4, we studied the interaction of the ENZ mode in a thin layer of ITO with the Mie modes of a dielectric metasurface over ITO. We showed how the electric dipole and magnetic dipole resonances are strongly coupled to the ENZ mode through simulations, analysis, and experiments. When strong coupling happens in a system with various modes, it means that the modes start to transfer energy between each other, and the rate of energy transfer is higher than the decay rate of each mode. One of the most detectable consequences of strong coupling is that the resonances related to modes before the coupling happens split into two hybrid modes, one at lower and one at higher energies. This consequence of strong coupling was the one we used to detect and analyze the effect in our samples. The coupling strength and also the strength of the hybrid modes can be improved by increasing the thickness of ITO to some extent. Note that by increasing the thickness of ITO, surface plasmon modes start to kick in at some point and make the system even more complex as the coupling may happen between any of the modes. Similar research on higher-order Mie modes, such as electric and magnetic quadrupoles, is also interesting.

At the end of Chapter 4, we discussed the experimental results of the nonlinear response of our dielectric metasurfaces. We tested the samples in a pump-probe set-up similar to the ones explained in Chapters 2 and 3, with the difference that we only studied the transmittance of the probe beam. We showed a large ultra-fast modulation of the transmittance of the probe in response to the pump, up to around 80 times larger than the modulation magnitude of a bare ITO sample. The response was highly wideband for both samples, specifically the MDR sample, where we could observe a diverse response with increasing and decreasing modulations at different incident wavelengths.

The dielectric on ITO samples can be used for studying other types of nonlinear responses. Our initial experimental investigations have shown more than five times improvement in the four-wave mixing signal of the sample compared to a bare 23-nm ITO sample. We also expect larger second-harmonic and third-harmonic generations in the samples. It is also expected that the samples can be used for adiabatic wavelength conversion, similar to Chapter 2.

In chapters 3 and 4, we studied the interaction of arrays of different types of nanoantennas with ITO. On the other hand, in Chapter 5, we numerically study the response of nanoantennas made of ITO as the potential building blocks of time-varying highly nonlinear metasurfaces. We first proposed a method based on recurrent equations to include the large nonlinear refractive index of ITO in inherently linear simulation environments of Lumerical FDTD. We then used the method to study the scattering pattern of nano-antennas made of ITO in linear and nonlinear regimes and investigated the applications of such nanoantennas. Our method for including the large nonlinear refractive index in numerical analysis can be used for any material with a large nonlinear Kerr effect. We are also interested in the fabrication and experimental characterizations of the samples investigated in Chapter 5.

In addition to these main projects, I also had the chance to contribute to other interesting projects related to the behavior of ENZ materials. These projects are presented in Appendix 3 of the thesis. In the first project, we made an artificial ENZ medium using a multi-stack made of thin subsequent layers of silver and SiO2. We studied the nonlinear response of that medium using the Z-scan technique. The last project in the appendix is to study the strong coupling effect between the ENZ mode of ITO and the surface plasmon mode related to a layer of gold deposited on ITO.

Overall, we showed how the large and fast nonlinear response of ENZ materials, specifically ITO, can make this group of materials a perfect candidate for all-optical time-varying systems. We also showed how the coupled system of ITO and plasmonic or dielectric metasurfaces could make schemes for ultrafast spatiotemporal manipulation of light. Each of the projects presented in this thesis can open a gate in the fields of science and technology that benefit from the all-optical nonlinear systems.

Appendix I

Supplementary Information

Broadband frequency translation through time refraction in an epsilon-near-zero material

Zhou *et al*.

Supplementary Information

Yiyu Zhou[1,†,*], M. Zahirul Alam[2, †], Mohammad Karimi[2], Jeremy Upham[2], Orad Reshef[2], Cong Liu[3], Alan E. Willner[3] and Robert W. Boyd[1,2]

[1]The Institute of Optics, University of Rochester, Rochester, New York 14627, USA

[2]Department of Physics, University of Ottawa, Ottawa, Ontario K1N 6N5, Canada

[3]Department of Electrical Engineering, University of Southern California, Los Angeles, California, 90089, USA

[†]These authors contributed equally

Supplementary Note 1: Experimental setup

We use a wavelength-tunable optical parametric amplifier (TOPAS prime, Spectra Physics) pumped by an amplified Ti:sapphire laser (Mai Tai, Spectra Physics) as the ultrafast pulse source. A 45:55 pellicle beamsplitter (BP245B3, Thorlabs) is used to split the input beam, and a high-precision translation stage (DDSM100, Thorlabs) is used to tune the delay time between pump and probe pulses. We use a thin film polarizer mounted on a rotation stage and a Glan-Taylor polarizing beam splitter to control the pulse intensity while keeping the polarization to be p-polarized. We use a multimode fiber with 50 µm core diameter to collect the probe pulse after the sample and use an optical spectrum analyzer to record the spectra of the probe.

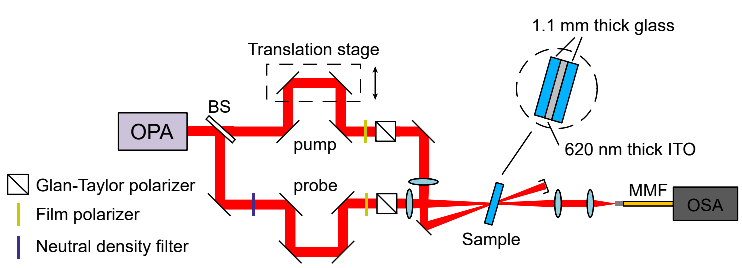

Supplementary Figure 1. The schematic of the experimental setup. In the pump beam arm, we rotate the first polarizer to control the peak pump intensity. BS, pellicle beamsplitter. OPA, optical parametric amplifier. OSA, optical spectrum analyzer. MMF, multimode fiber.

Supplementary Note 2: Numerical simulation

We use a split-step Fourier method to solve the nonlinear Schrödinger equation (NLSE)[1] to model the nonlinear interactions between the pump and the probe beam pulses propagating through the ITO sample. We ignore all nonlinear optical effects higher than the third-order effects[2]. The propagation of the probe pulse through the time-varying ITO can be described as[3]

$$\frac{\partial A}{\partial z}+\beta_1\frac{\partial A}{\partial t}+\mathrm{i}\frac{\beta_2}{2}\frac{\partial^2 A}{\partial t^2}=\mathrm{i}\frac{\omega_0}{c}\Delta n_{\mathrm{eff}}(t-t_{\mathrm{d}},I_{\mathrm{pump}}(t))A, \tag{1}$$

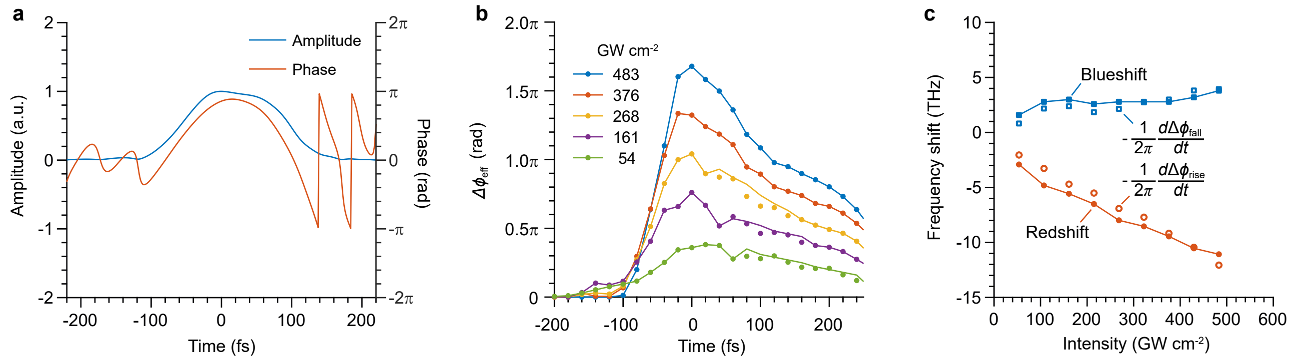

Supplementary Figure 2. **a**, Amplitude and phase of the optical pulses at 1235 nm retrieved by frequency-resolved optical gating. **b**, Numerically retrieved nonlinear phase variations $\Delta\phi_{\mathrm{eff}}(t)$ at different pump intensities. The dots represent the numerical results and the solid lines connecting the dots are to facilitate visualization. **c**, The experimentally measured redshifts and blueshifts as a function of pump intensity are represented by the solid lines, and the calculated maximum local frequency shifts are represented by hollow circles.

where $A(z,t)$ is the slowly varying envelope of the probe pulse, $\beta_1 \equiv (1/v_{\mathrm{g}})$ is the inverse of the group velocity, $\beta_2 \equiv \frac{\partial}{\partial\omega}(1/v_{\mathrm{g}})$ is the group velocity dispersion, c is the speed of light in vacuum, t_{d} is the pump-probe delay time, and ω_0 is the angular frequency of the light beams. The effective time-dependent refractive index index $\Delta n_{\mathrm{eff}}(t, I_{\mathrm{pump}})$ on the right-hand side is a function of pump intensity and the delay time between the pump and the probe. This term acts as the driving term for the nonlinear pulse propagation and is responsible for the frequency translation. The relative permittivity of ITO around its epsilon-near-zero spectral range can be modeled by a Drude function as[4]

$$\varepsilon(\omega) = \varepsilon_\infty - \omega_{\mathrm{p}}^2/(\omega^2 + \mathrm{i}\gamma\omega), \tag{2}$$

where $\varepsilon_\infty = 3.80$, $\omega = 2\pi c/\lambda$ is the frequency of light, $\omega_{\mathrm{p}} = 2\pi\cdot 473$ THz is the plasma frequency, and $\gamma = 0.0468\cdot 2\pi\cdot 473$ THz is the damping rate. The refractive index of ITO can thus be expressed as $n(\omega) = \sqrt{\varepsilon(\omega)}$. The dispersion coefficients can be calculated as $\beta_m = \left(\frac{d^m\beta}{d\omega^m}\right)_{\omega=\omega_0}$, where $\beta(\omega) = \mathrm{Re}(n(\omega))\omega/c$. At $\lambda = 1235$ nm we have $\beta_1 = 1.53\times 10^7$ fs m^{-1} and $\beta_2 = 1.10\times 10^8$ fs^2 m^{-1}. The dispersion length is found to be $L_{\mathrm{D}} = T_0^2/\beta_2 = 47.1$ µm, where $2\sqrt{\ln(2)}T_0 = 120$ fs is the FWHM pulse width. Since the dispersion length is two orders of magnitude larger than the ITO thickness of 0.62 µm, we neglect higher-order dispersion terms.

For the numerical simulation we ignore the changes in $\Delta n_{\mathrm{eff}}(t)$ that occur at the time scale of the oscillation of the carrier waves of the pump pulse. We only take into account the pump-envelope-dependent changes in the refractive index. Thus, in our simulation we approximate $\Delta n_{\mathrm{eff}}(t)$ as a function of the envelope of the pump pulse only. We use an iterative least squares curve fitting algorithm to extract an approximate shape of pump-intensity-dependent $\Delta n_{\mathrm{eff}}(t)$ that results in the experimentally obtained output probe spectra for a fixed pump intensity as follows: (1) We begin with an initial guess $\Delta n_{\mathrm{eff}}^1(t)$. For j-th iteration, the corresponding index change is denoted as $\Delta n_{\mathrm{eff}}^j(t)$. (2) For the index change $\Delta n_{\mathrm{eff}}^j(t)$ and a specific pump-probe delay time t'_{d}, we use $\Delta n_{\mathrm{eff}}^j(t - t'_{\mathrm{d}})$ in Supplementary Eq. (1) and perform the split-step Fourier method to generate an output pulse $A^j(z_1, t; t'_{\mathrm{d}})$, where $z_1 = 620$ nm. The output spectrum can be calculated via Fourier transform as $S^j(f,t'_\mathrm{d}) = |\int A^j(z_1,t;t'_\mathrm{d})\exp(-\mathrm{i}2\pi ft)\,dt|^2$. We repeat this procedure for different delay times and therefore obtain the two-dimensional spectrogram $S^j(f,t_\mathrm{d})$ with -200 fs $\leq t_\mathrm{d} \leq 200$ fs. (3) We use a fitting algorithm (lsqcurvefit, MATLAB) to fit $S^j(f,t_\mathrm{d})$ to the experimental data $S^{\mathrm{exp}}(f,t_\mathrm{d})$ by adjusting $\Delta n^j_{\mathrm{eff}}(t)$. In other words, $\Delta n^j_{\mathrm{eff}}(t)$ is the parameter to be tuned iteratively. The final results of $S^j(f,t_\mathrm{d})$ at different pump intensities are presented in Fig. 3(d-f) in the manuscript.

In order to obtain the temporal amplitude and phase of the input probe pulses at the wavelengths of interest, i.e. $A(z=0,t)$, we performed a series of frequency-resolved optical gating (FROG) measurements[5]. In our simulation we always assume a homogeneous index change throughout the entire ITO film for simplification. We also ignore the time difference of the index change between the front and the back ends of the sample since the transit time through the sample is roughly two-orders of magnitude smaller than the temporal width of the pump pulse. We also ignore the Fresnel-reflection- and absorption-induced change in the pump intensity inside the sample for simplification. In addition, we also ignore nonlinear change in dispersion. The experimentally measured temporal amplitude and phase of the input probe pulse at 1235 nm is shown in Supplementary Fig. 2a.

An alternative way to understand the effect of index change is to use the concept of a local frequency shift. The local frequency shift can be used as an approximate estimation of spectral shift and can be expressed as[6]

$$\Delta f(t) = \frac{1}{2\pi}\Delta\omega(t) = -\frac{1}{2\pi}\frac{d\Delta\phi_{\mathrm{eff}}(t)}{dt}, \tag{3}$$

where the nonlinear phase variation induced by Δn_{eff} is $\Delta\phi_{\mathrm{eff}}(t) = k \cdot L \cdot \Delta n_{\mathrm{eff}}(t)$, where $k = 2\pi/\lambda$ is the wavenumber, and $L = 620$ nm is the ITO thickness. The retrieved phase variation $\Delta\phi_{\mathrm{eff}}$ is displayed for different peak pump intensities in Supplementary Fig. 2b. For a given $\Delta\phi_{\mathrm{eff}}$, the maximum local frequency redshift is determined by the rising edge of the nonlinear phase change as $\Delta f_{\mathrm{red}} = \min(\Delta f(t)) = -\frac{1}{2\pi}\frac{d\Delta\phi_{\mathrm{rise}}}{dt}$, while the maximum local frequency blueshift is determined by the falling edge as $\Delta f_{\mathrm{blue}} = \max(\Delta f(t)) = -\frac{1}{2\pi}\frac{d\Delta\phi_{\mathrm{fall}}}{dt}$. The numerically retrieved maximum local frequency shifts at different pump intensities are shown in Supplementary Fig. 2c. The retrieved maximum local frequency shifts are in good agreement with the experimentally measured frequency shifts.

Supplementary Note 3: Additional time refraction effects and unnormalized spectra

Since the focus of this work is on frequency translation, we presented spectral data with normalized amplitude in the main text. However, time refraction also affects the amplitude of the frequency-translated pulse[7]. Let us consider the simplest time-refraction model — a Gaussian pulse with carrier frequency ω_0 and pulse width T_0 is travelling through a medium whose refractive index changes from n_1 to n_2. We assume that the longitudinal length of the medium is larger than the longitudinal length of the pulse. In such an idealized case the input (E_{in}) and output (E_{out}) pulses can be expressed as[8]

$$E_{\text{in}} = E_0 \exp(-\frac{t^2}{2T_0^2}) \exp(-\mathrm{i}\omega_0 t), \qquad E_{\text{out}} = (\frac{n_1}{n_2} E_0)\ \exp(-\frac{t^2}{2(T_0 n_2/n_1)^2})\ \exp(-\mathrm{i}\frac{n_1}{n_2}\omega_0 t). \tag{4}$$

The above simple model shows that the time refraction effect can modify amplitude, temporal width (by Fourier relation the spectral width), and the central frequency. Therefore, the relative changes in spectral amplitude may also be of interest. Below we present the spectral data for five different probe wavelengths for various pump-probe delays in Supplementary Fig. 3-7, where the spectral peak magnitude in the absence of pump pulse is normalized to unity. However, it should be noted that in addition to time refraction there are several other competing effects in ITO that can significantly modulate the transmittance of the probe pulse. Since the ITO has a small linear index and exhibits a large nonlinear index change, the Fresnel reflection coefficients exhibit strong time-dependent variations. In addition, due to saturable absorption, the imaginary part of the refractive index and, consequently, the loss in ITO can drop significantly in the presence of a pump pulse. Thus the spectral amplitude of the probe for a given pump-probe delay and pump intensity depends on time-refraction effects, nonlinear changes in Fresnel reflection coefficient, and changes in absorption. Therefore a sophisticated model is required to isolate these three effects to accurately quantify the effect of time refraction on the amplitude, which is beyond the scope of this work. Nevertheless, it can be noticed that for all wavelengths of interest, the transmittance of the probe beam significantly increases when the probe is blueshifted.

We also note that the absorption loss in ITO in the ENZ spectral range is large compared to standard dielectric materials. We note that a fair figure of merit for such a medium should be the magnitude of nonlinear change over one absorption length. Clearly ITO cannot be used to make optical fibre or nanophotonics waveguides of hundreds of microns in length. The crucial advantage of these ENZ materials over other conventional materials is that one needs to propagate over only a sub-micron distance in a nonlinear ENZ material for a comparable effect that is achieved by a hundreds of microns long nanophotonic waveguide made of a conventional photonics material. It should be noted that for this work we are using a commercially available sample that has never been optimized for the purpose of this work. In addition, there are still many opportunities to further enhance the performance of ENZ materials. A few promising routes are: i) use an ENZ material with higher electron mobility, ii) nanostructure the ENZ material or include plasmonic systems to achieve higher effective index change within reduced thickness and loss, iii) integrate ENZ material with optical waveguides as the cladding, etc. We also note that in the presence of strong pump the transmittance of the probe can actually increase due to the increased refractive index and reduced loss. Finally, we note that the use of optical amplifiers to boost a weak signal is a standard system protocol. Furthermore, the recent advancement in short pulse amplification might also be of interest for particular applications[9].

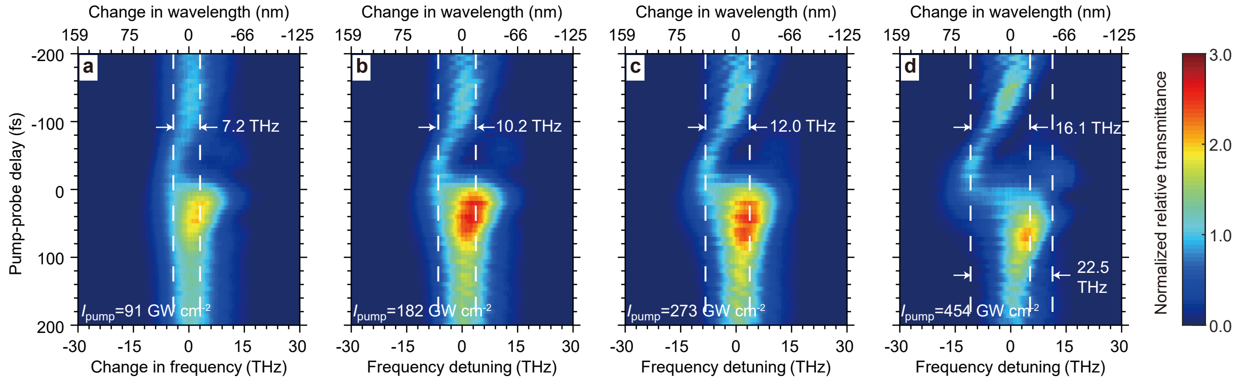

Supplementary Figure 3. **a-d**, The experimentally measured spectra of 1184 nm probe pulse at different pump intensities. The spectral peak of the probe beam in the absence of pump beam is normalized to unity.

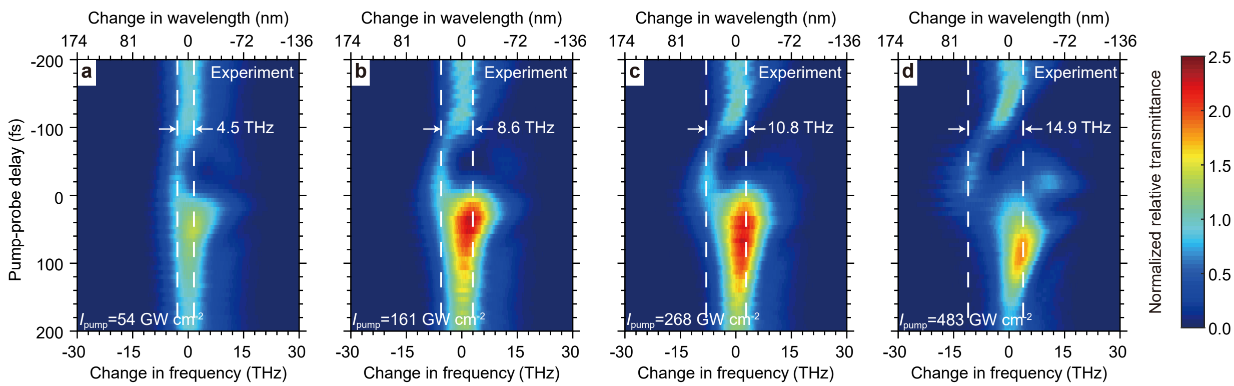

Supplementary Figure 4. **a-d**, The experimentally measured spectra of 1235 nm probe pulse at different pump intensities. The spectral peak of the probe beam in the absence of pump beam is normalized to unity.

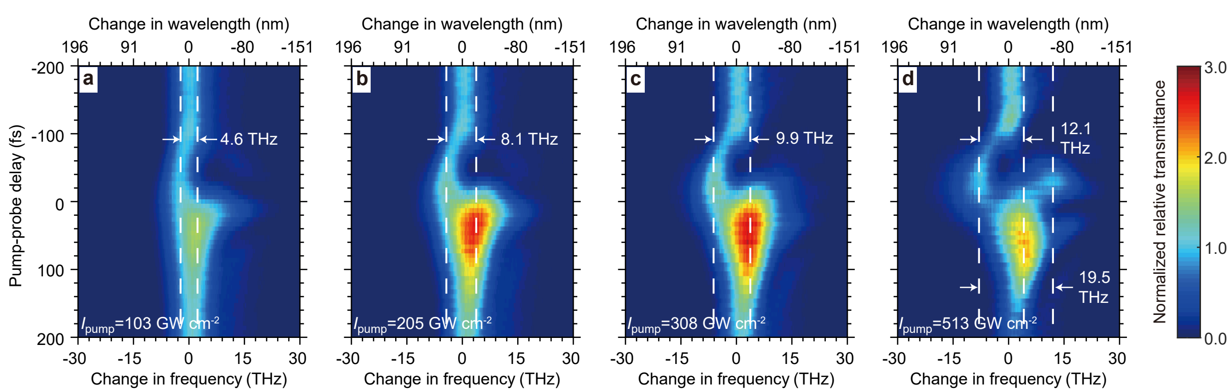

Supplementary Figure 5. **a-d**, The experimentally measured spectra of 1305 nm probe pulse at different pump intensities. The spectral peak of the probe beam in the absence of pump beam is normalized to unity.

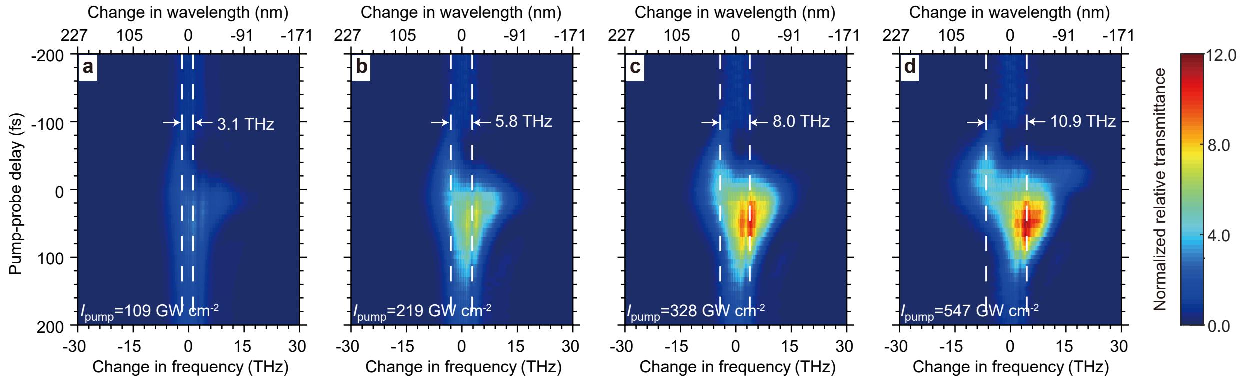

Supplementary Figure 6. **a-d**, The experimentally measured spectra of 1398 nm probe pulse at different pump intensities. The spectral peak of the probe beam in the absence of pump beam is normalized to unity.

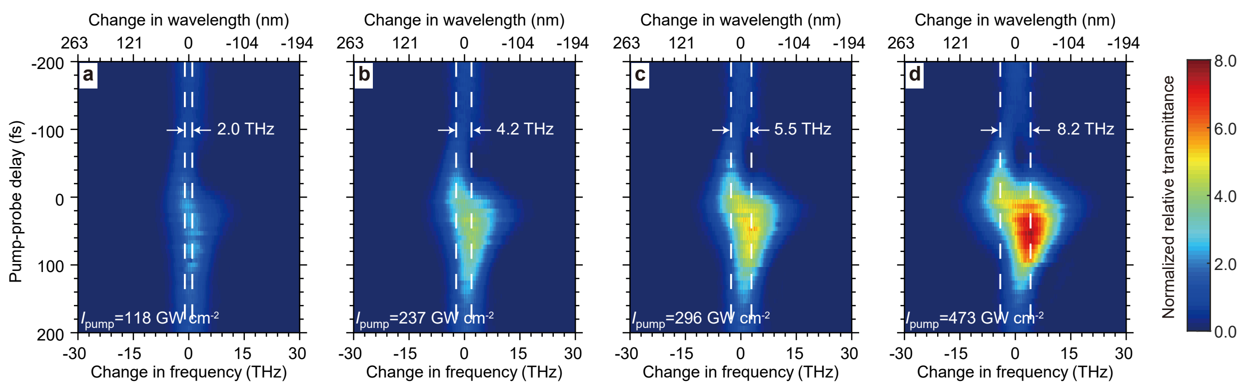

Supplementary Figure 7. **a-d**, The experimentally measured spectra of 1495 nm probe pulse at different pump intensities. The spectral peak of the probe beam in the absence of pump beam is normalized to unity.

Supplementary Note 4: Effects of fifth-order nonlinearity

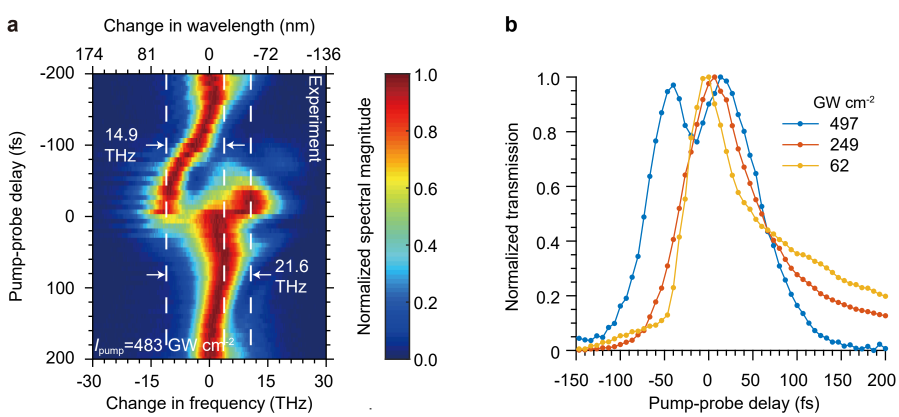

Supplementary Figure 8. **a**, The experimentally measured probe spectrogram at the peak pump intensity of 483 GW cm^{-2}. **b**, The experimentally measured probe transmission at different pump intensities as a function of pump-probe delay time.

At a high pump intensity of greater than 450 GW cm^{-2} close to the zero permittivity wavelength we observe onsets of higher-order nonlinear optical effects. For example, at $\lambda_0 = 1235$ nm at a pump intensity of 480 GW cm^{-2} we observe a relatively large blueshifted peak as shown in Supplementary Fig. 8a due to an effective fifth-order nonlinear optical process. In a pump-probe transmission measurement this effective fifth-order process leads to a sudden drop in the transmission of the probe Supplementary Fig. 8b. From these results we conclude that the effective fifth-order process has an opposite sign to that of the effective third-order process and that the relevant time scales for the fifth-order-nonlinearity-induced blue shift is much shorter compared to the effective third-order-nonlinearity-induced blue shift at lower intensities.

Supplementary Note 5: Normalized spectra at other wavelengths

Here, we provide the detailed measurement results for pump-probe wavelengths ranging from $\lambda = 1000$ nm to 1500 nm in Supplementary Fig. 9-14.

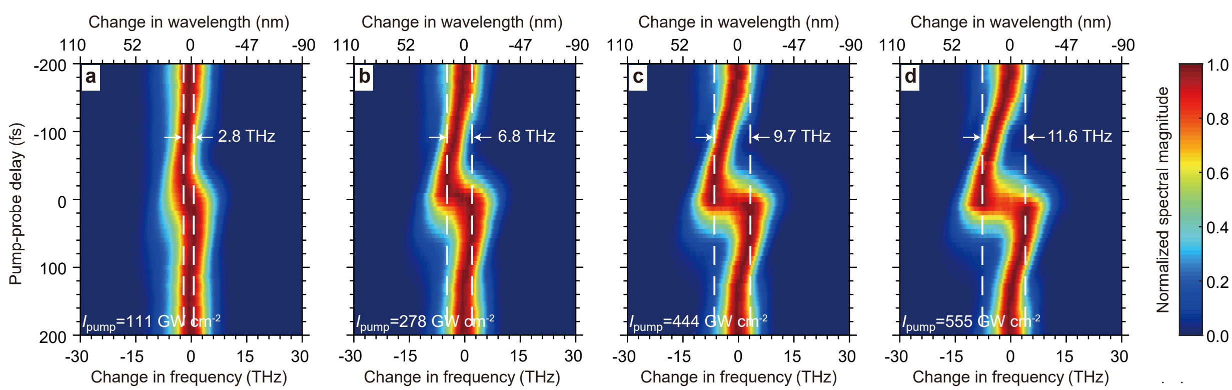

Supplementary Figure 9. **a-d**, The experimentally measured spectra of 1000 nm probe pulse at different pump intensities. The magnitudes of the measured maximum redshift and blueshift are denoted by the corresponding white dashed lines.

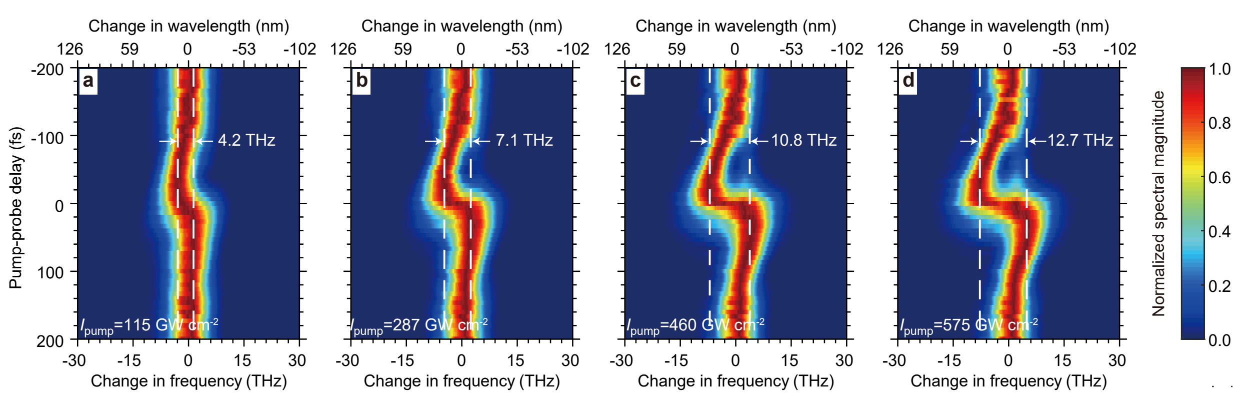

Supplementary Figure 10. **a-d**, The experimentally measured spectra of 1060 nm probe pulse at different pump intensities. The magnitudes of the measured maximum redshift and blueshift are denoted by the corresponding white dashed lines.

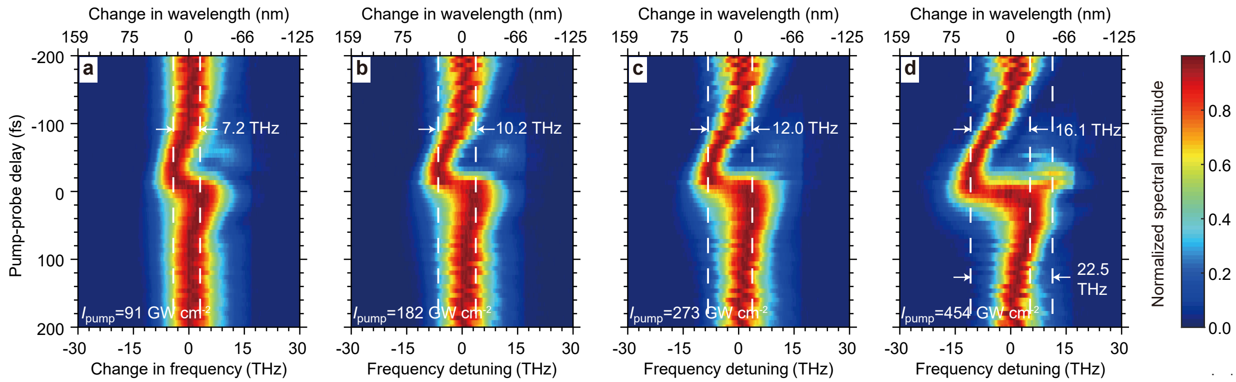

Supplementary Figure 11. **a-d**, The experimentally measured spectra of 1184 nm probe pulse at different pump intensities. The magnitudes of the measured maximum redshift and blueshift are denoted by the corresponding white dashed lines. The subpanel **d** also shows the an additional blueshifted peak (6.4 THz) due to the effective fifth-order nonlinear process.

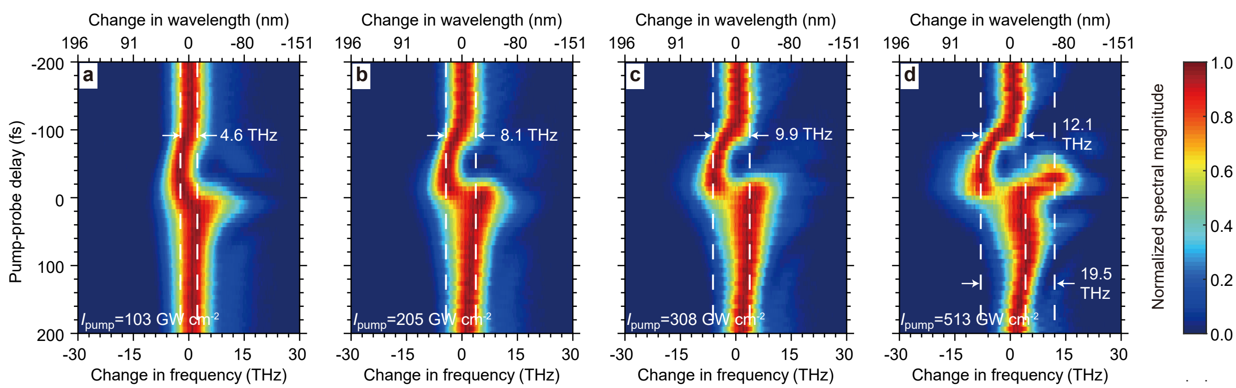

Supplementary Figure 12. **a-d**, The experimentally measured spectra of 1305 nm probe pulse at different pump intensities. The magnitudes of the measured maximum redshift and blueshift are denoted by the corresponding white dashed lines.The subpanel **d** also shows the an additional blueshifted peak (7.4 THz) due to the effective fifth-order nonlinear process.

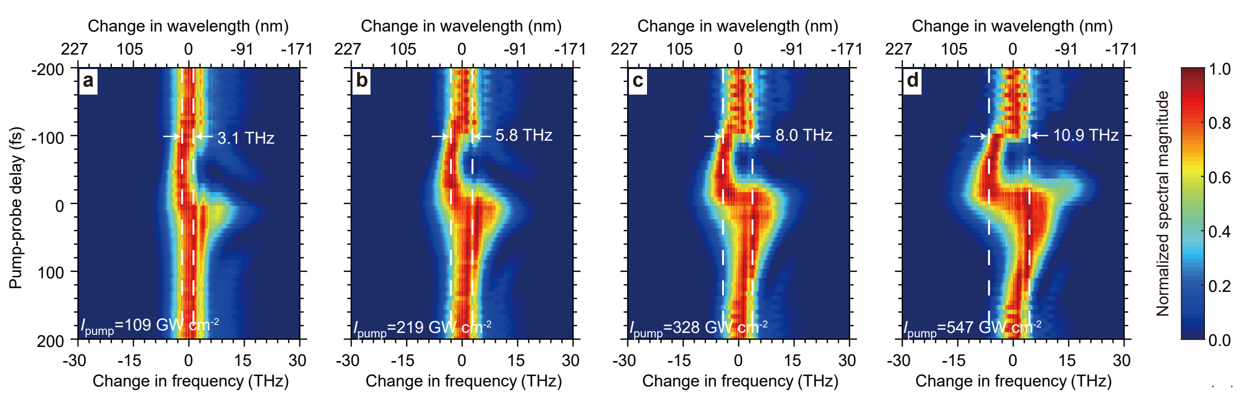

Supplementary Figure 13. **a-d**, The experimentally measured spectra of 1398 nm probe pulse at different pump intensities. The magnitudes of the measured maximum redshift and blueshift are denoted by the corresponding white dashed lines.

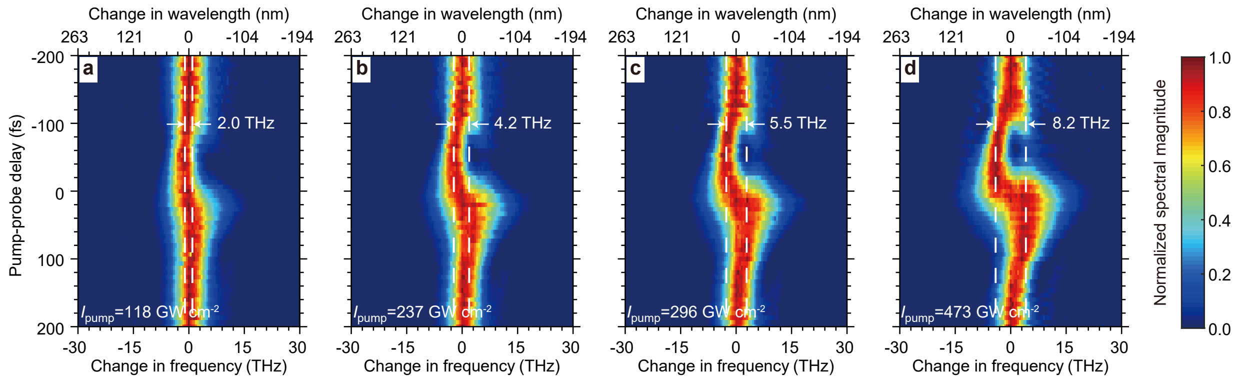

Supplementary Figure 14. a-d, The experimentally measured spectra of 1495 nm probe pulse at different pump intensities. The magnitudes of the measured maximum redshift and blueshift are denoted by the corresponding white dashed lines.

Supplementary Note 6: Analysis of the air gap between ITO films

In our experiment, we form a 620-nm-thick medium by sandwiching two commercially available 310-nm-thick ITO films deposited on 1.1-mm-thick glass. However, a white-light interferometric measurement reveals that there remains an air gap between two layers of the ITO thin films. We measure the air gap to be roughly 2200 nm thick. Air has a higher refractive index than ITO at the wavelengths of interest (e.g. $n_{\mathrm{ITO}} = 0.42 + 0.42\mathrm{i}$ at $\lambda_0 = 1240$ nm) and the air gap has a thickness slightly larger than the free-space wavelength. Thus one may expect that there is an unintended weak cavity effect due to thin film interference effects for our structure. However we posit that this unintended air gap affects our results minimally for two reasons. First, compared to ITO the nonlinear response of the air gap at the pump intensities relevant for this experiment is negligible. Second, the effective third-order nonlinear response of ITO leads to an increase in refractive index at all wavelengths of interest in this work. Thus at high pump intensities for which the frequency translation of the probe pulses are the largest, the thin-film interference effects effectively disappears.

Supplementary References

1. Agrawal, G. P. *Nonlinear fiber optics* (Springer, 2000).

2. Boyd, R. W. *Nonlinear optics* (Elsevier, 2003).

3. Plansinis, B. W., Donaldson, W. R. & Agrawal, G. P. What is the temporal analog of reflection and refraction of optical beams? *Phys. Rev. Lett.* **115**, 183901 (2015).

4. Alam, M. Z., De Leon, I. & Boyd, R. W. Large optical nonlinearity of indium tin oxide in its epsilon-near-zero region. *Science* **352**, 795–797 (2016).

5. Trebino, R. et al. Measuring ultrashort laser pulses in the time-frequency domain using frequency-resolved optical gating. *Rev. Sci. Instrum.* **68**, 3277–3295 (1997).

6. Dekker, R. et al. Ultrafast kerr-induced all-optical wavelength conversion in silicon waveguides using 1.55 μm femtosecond pulses. *Opt. Express* **14**, 8336–8346 (2006).

7. Xiao, Y., Maywar, D. N. & Agrawal, G. P. Reflection and transmission of electromagnetic waves at a temporal boundary. *Opt. Lett.* **39**, 574–577 (2014).

8. Xiao, Y. *Propagation of optical pulses in dynamic media: a time transformation method* (PhD thesis, University of Rochester, 2014).

9. Vampa, G. et al. Light amplification by seeded kerr instability. *Science* **359**, 673–675 (2018).

Appendix II

Supplementary Information

Time-varying gradient metasurface with applications in all-optical beam steering

M. Karimi *et al*.

Research Article

Mohammad Karimi*, M. Zahirul Alam, Jeremy Upham, Orad Reshef, and Robert W. Boyd

Supplementary Material: Time-varying gradient metasurface with applications in all-optical beam steering

https://doi.org/10.1515/sample-YYYY-XXXX
Received Month DD, YYYY; revised Month DD, YYYY; accepted Month DD, YYYY

Abstract: This document contains supplementary information for the paper entitled "Time-varying gradient metasurface with applications in all-optical beam steering". In Section 1 we provide the ellipsometry data for the wavelength-dependent permittivity of the ITO sample we used around the ENZ point. Section 2 shows the angular distribution of the reflected diffraction orders from the surface alongside the phase that is accumulated by the reflected diffraction orders. Finally, Section 3 shows the schematic of the set-ups that used for testing the device.

Keywords: Nonlinear Optics, Epsilon-Near-Zero (ENZ), Metasurface

1 The permittivity of the ITO sample

The permittivity of ITO in the infrared region follows the Drude model as in figure S1. The relation between the permittivity and the frequency in the Drude model can be represented as

$$\epsilon(\omega) = \epsilon_\infty + \frac{\omega_p^2}{\omega(\omega + i\gamma\omega_p)} \tag{1}$$

where $\epsilon_\infty = 3.69$, $\omega_p = 2.67e^{15} rad/s$ and $\gamma = 0.045\omega_p$ for our ITO sample.

2 Electric field enhancement

In order to investigate the enhancement of the field within ITO, induced by the nanoantennas, we plot the electric field enhancement at the central wavelength of 1300 nm in figure S2. The data was taken from the simulation of the structure in Lumerical FDTD. We observe that each antenna is resonating differently at this specific wavelength and so we have different field enhancement around each antenna.

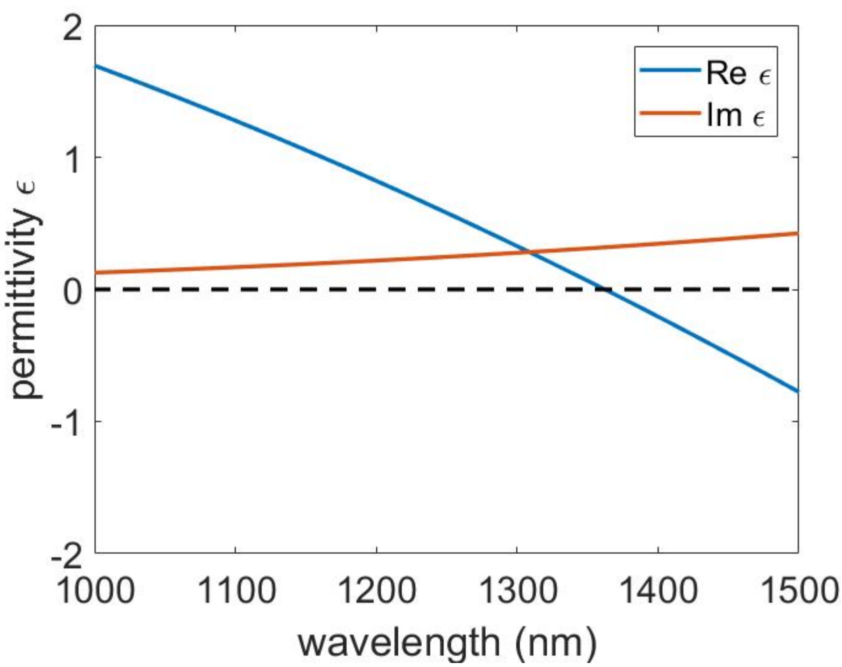

Fig. S1: The permittivity of the ITO sample with a thickness of 65 nm used in our experiment extracted from ellipsometry and fit using the Drude model.

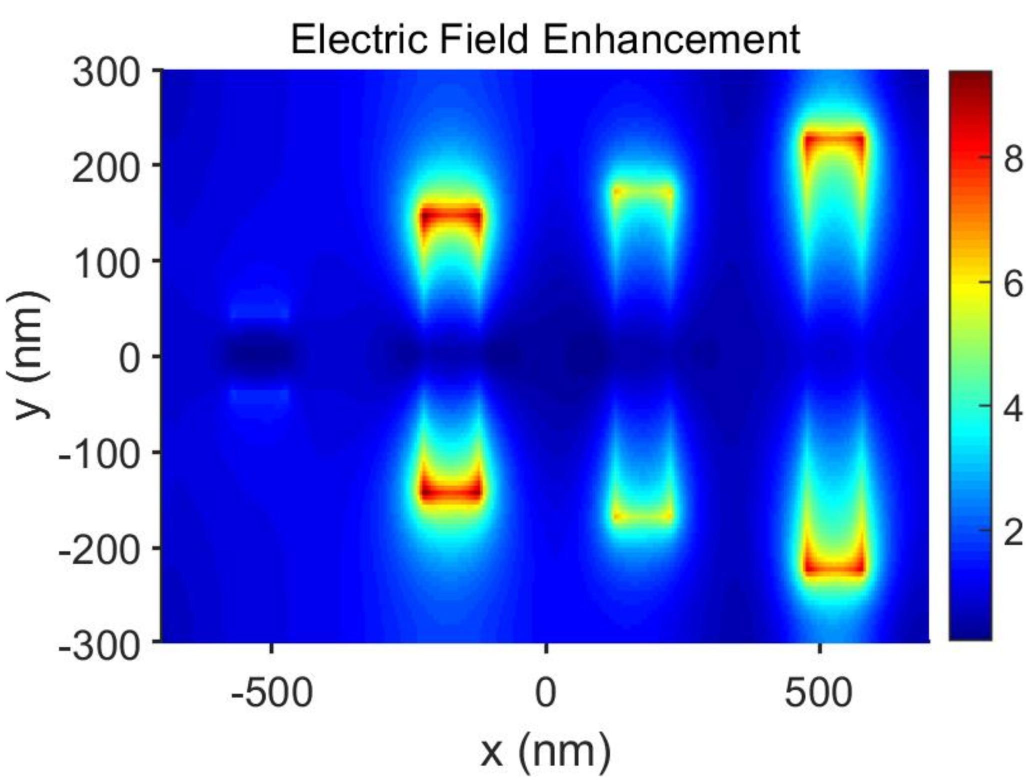

Fig. S2: The enhancement of the electric field in ITO adjacent to the nanoantennas in a single cell at wavelength = 1300 nm. The simulation was done in Lumerical FDTD.

3 The angular distribution of the diffraction orders

3.1 effect of ITO on the angular distribution

Due to the non-negligible imaginary part of the ITO permittivity, the presence of ITO will introduce more loss to the system. It also affects the effective refractive index of the system that leads to the manipulation of the power distribution between different DOs. Figure S3 compares the angular distribution of the DOs in the absence and the presence of 65-nm layer of ITO.

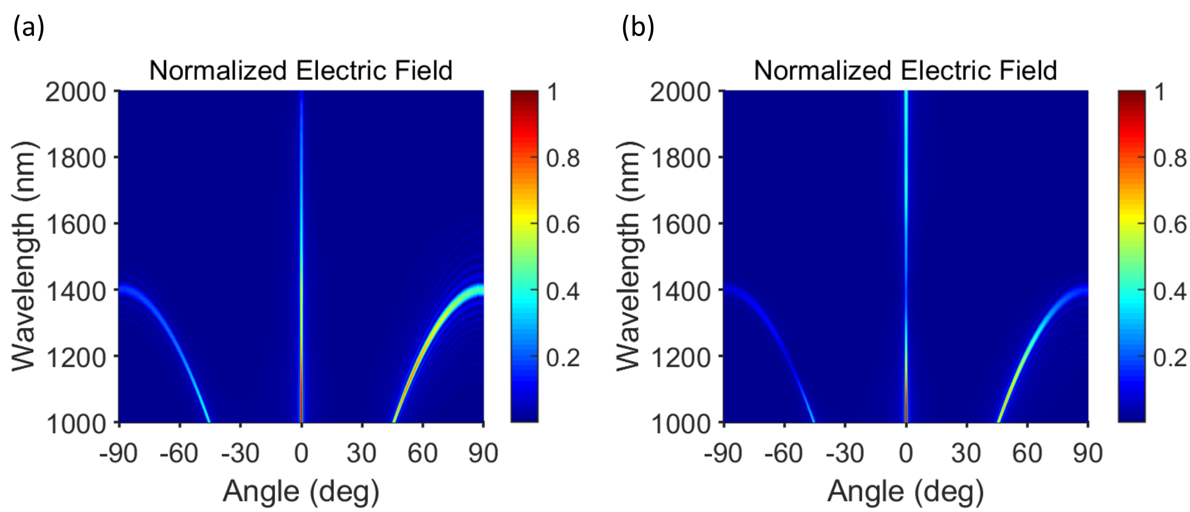

Fig. S3: The distribution of the norm of electric field to different angles and at different wavelengths in reflection. (a) is in the absence of the ITO substrate and (b) is in the presence of the ITO substrate

3.2 Total reflectance at different angles of incidence

In order to give an insight on how the beams are interacting with the material at larger angles we simulated the structure under different angles of incidence. Figure S4 shows the total reflectance of the beam as a function of incident angle inside the glass. We see that the reflectance goes up at larger angles of incidence which affects the portion of light that interacts with the system.

3.3 Spectral response of diffraction orders

To investigate the portion of the incident power that couples into each diffraction order (DO), we performed some linear simulations and experimental characterizations. Figure S5 shows the coupling efficiency of different diffraction orders in (a) reflection and (b) transmission for our sample. The solid lines are the simulation results using COMSOL Multiphysics and the dots with error bars are the experimental results. It is also important to study the phase of the reflected DOs accumulated over the metasurface to get an

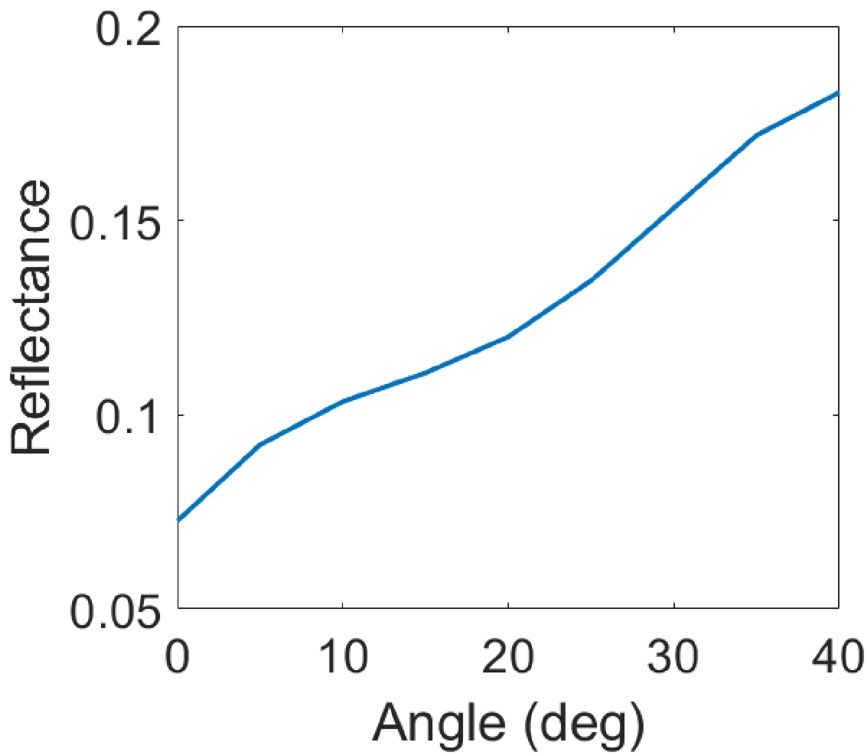

Fig. S4: The total reflectance of the beam from the sample at different angles of incidence within the glass

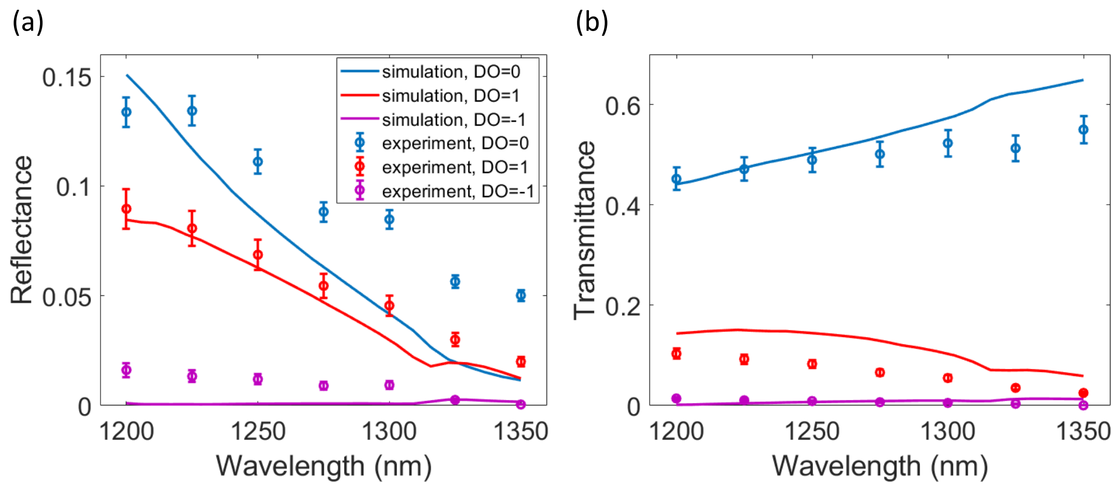

Fig. S5: The linear characterization of the sample in reflection (a) and transmission (b), and in simulation (solid lines) and experiment (error bar dots) for diffraction orders DO=0,±1. The vertical axis in both plots shows the portion of the incident light that has coupled to the diffraction orders.

estimation of the interaction times of each DO with the medium. Figure S6 shows the accumulated phase for the reflected DOs. The phase plotted in this figure is extracted from the simulation of the device in Comsol Multiphysics after the subtraction of the accumulated phase from the port to the surface and vice versa. It suggests that the phase acquired by DO=-1 after interacting with the medium is almost twice larger than that of DO=+1 which can be translated into a longer interaction time of the former DO with the time-varying medium. These results can, at least qualitatively, approve our explanation for the asymmetric nonlinear response of the device demonstrated in figures 2, 3, and 4 of the paper. Note that this phase accumulation result is performed in a linear regime and is not expected to explain all the results that we observed in the nonlinear regime quantitatively as it has to be superimposed by the nonlinear response of ITO/plasmonic metasurface system at different wavelengths to give us a complete insight on the performance of the device.

Figure S7 (a) shows that how the periodic gradient metasurface can be modeled as a blazed grating. When the designed metasurface is illuminated at normal incidence, two diffraction orders of DO=+1 and DO=-1 are diffracted to two angles symmetric around the normal of the surface. Figure S7 (b) shows how the power is distributed between different angles at different wavelengths for the linear case. Figure S7 (d) shows the same results with the plasma frequency of ITO in the Drude model shifted by 10 %. This amount of shift in plasma frequency has been found to be a good approximation to model the change in the permittivity due to nonlinear responses with our pump intensity [1, 2]. The results in this figure show how the distribution of power between different wavelengths and angles can change due to time-independent nonlinear effects such as the modification of the phase ramp over each unit cell of the metasurface. We see that the time-independent effects are small enough to be ignored in comparison to adiabatic wavelength conversion (AWC).

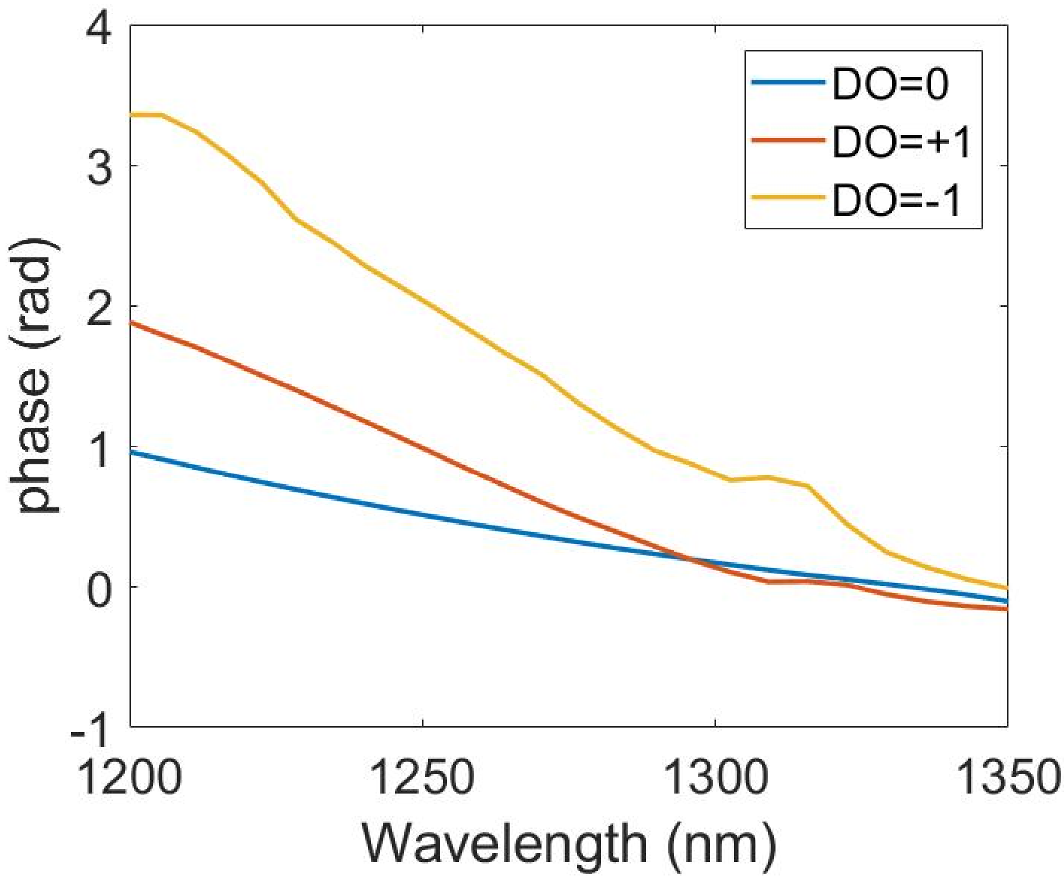

Fig. S6: The phase gained by each reflected diffraction order from the metasurface simulated using Comsol Multiphysics.

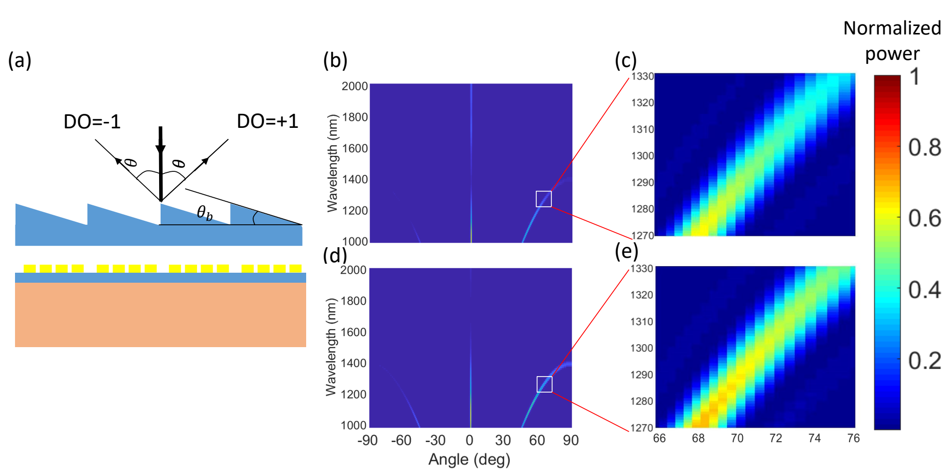

Fig. S7: (a) The schematic of a blazed grating as a model to our gradient metasurface. DO=+1 and DO=-1 are the first diffraction orders. (b) and (c) The angular distribution of DO=+1 for the linear and static nonlinear cases respectively.

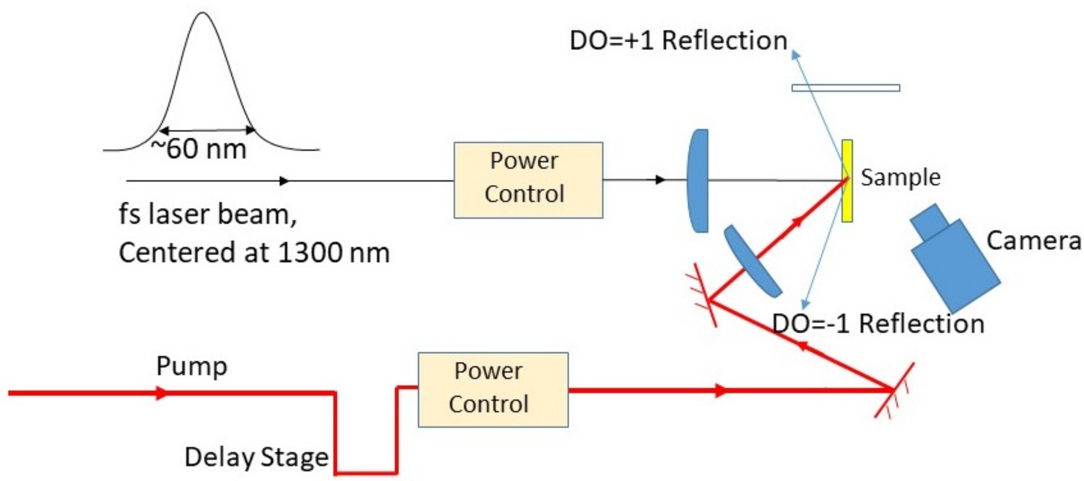

Fig. S8: The schematic of the set-up for measuring the angle distribution of the power for different diffraction orders.

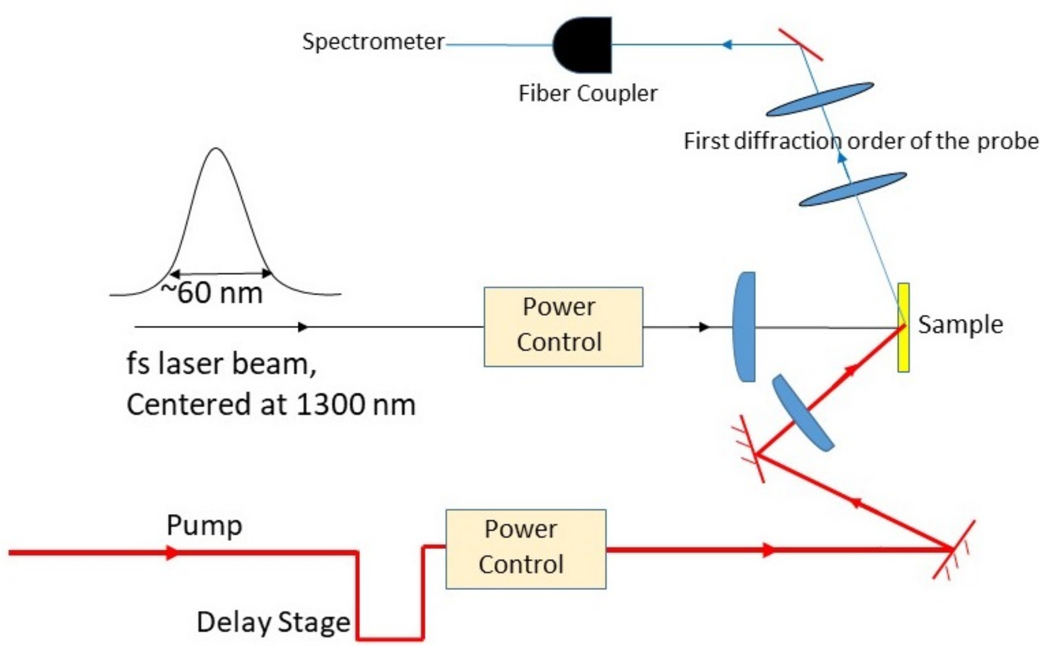

Fig. S9: The schematic of the set-up for measuring the angle-dependent spectrum of different diffraction orders.

4 Measurement set-ups

We used a standard degenerate pump-probe set-up to characterize the sample. The duration of our pulse has been measured to be around 120 fs. The spectral width of our beam is around 60 nm at a central wavelength of 1300 nm. A delay line has been inserted in the pump path to finely control the time delay between the pump and the probe beams. The probe is illuminating the sample at normal incidence and the incident angle of the pump has been set to 5 degrees. Figure S8 shows the schematic of the set-up used to measure the angular distribution of power using a screen and an infrared camera. Figure S9 shows the scheme of the set-up used for measuring the spectrum of the diffraction orders at different angles.

References

[1] M. Z. Alam, I. De Leon, and R. W. Boyd, "Large optical nonlinearity of indium tin oxide in its epsilon-near-zero region," *Science*, vol. 352, no. 6287, pp. 795–797, 2016.

[2] M. Z. Alam, S. A. Schulz, J. Upham, I. De Leon, and R. W. Boyd, "Large optical nonlinearity of nanoantennas coupled to an epsilon-near-zero material," *Nature Photonics*, vol. 12, no. 2, pp. 79–83, 2018.

Appendix III
Additional Projects

Contribution Statement

Aside from the projects that make the main body of my paper, I have contributed to other projects related to the behavior of light under the epsilon-near-zero (ENZ) conditions. Here, I elucidate my contribution to each of these projects:

multi-layer stack ENZ medium

We made an artificial ENZ medium by stacking layers of SiO2 and silver. The effective permittivity of such a medium, when all layers are much thinner than the wavelength, is a weighted average of the permittivities of the single layers. As a result, we can satisfy the ENZ conditions in the visible range of light. The goal here was to measure the nonlinear refraction and absorption of light using the Z-scan technique. I briefly contributed to making the set-up and also did the automation of the set-up. I also briefly contributed to analyzing the data.

Strongly Coupled Plasmon Polaritons in Gold and ENZ Bifilms

The coupling between the ENZ mode in a thin layer of ITO and the surface plasmon modes in a simple junction of ITO and unstructured gold was the goal of this project. My contribution was to fabricate the samples.

ACS Photonics
pubs.acs.org/journal/apchd5
Letter

Enhanced Nonlinear Optical Responses of Layered Epsilon-near-Zero Metamaterials at Visible Frequencies

Sisira Suresh, Orad Reshef,* M. Zahirul Alam, Jeremy Upham, Mohammad Karimi, and Robert W. Boyd

Cite This: *ACS Photonics* 2021, 8, 125−129 Read Online

ACCESS | Metrics & More | Article Recommendations | Supporting Information

ABSTRACT: Optical materials with vanishing dielectric permittivity, known as epsilon-near-zero (ENZ) materials, have been shown to possess enhanced nonlinear optical responses in their ENZ region. These strong nonlinear optical properties have been firmly established in homogeneous materials; however, it is as of yet unclear whether metamaterials with *effective* optical parameters can exhibit a similar enhancement. Here, we probe an optical ENZ metamaterial composed of a subwavelength periodic stack of alternating Ag and SiO_2 layers and measure a nonlinear refractive index $n_2 = (1.2 \pm 0.1) \times 10^{-12}\ m^2/W$ and nonlinear absorption coefficient $\beta = (-1.5 \pm 0.2) \times 10^{-5}$ m/W at its effective zero-permittivity wavelength. The measured n_2 is 10^7 times larger than n_2 of fused silica and 4 times larger than the n_2 of silver. We observe that the nonlinear enhancement in n_2 scales as $1/(n_0\mathrm{Re}[n_0])$, where n_0 is the linear effective refractive index. As opposed to homogeneous ENZ materials, whose optical properties are dictated by their intrinsic material properties and hence are not widely tunable, the zero-permittivity wavelength of the demonstrated metamaterials may be chosen to lie anywhere within the visible spectrum by selecting the right thicknesses of the subwavelength layers. Consequently, our results offer the promise of a means to design metamaterials with large nonlinearities for applications in nanophotonics at any specified optical wavelength.

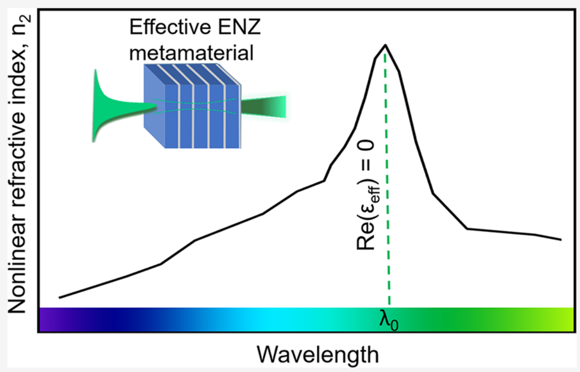

KEYWORDS: *epsilon-near-zero, metamaterials, nonlinear optics, multilayer stack, nanophotonics*

In recent years, much attention has been given to a class of materials with vanishing dielectric permittivity.[1−3] This class of materials, known as epsilon-near-zero (ENZ) materials, has become a topic of interest because of its intriguing optical properties including tunneling of light through arbitrary bends,[1] the ability to tailor radiation patterns,[4] and its enhanced nonlinear optical response.[5−8] The ENZ condition can be found in naturally occurring materials near their bulk plasma and phonon resonances. Most noble metals exhibit a zero-permittivity behavior in the UV region, near their respective plasma frequencies.[9] Transition metal nitrides such as titanium nitride[10] and zirconium nitride[11] display their ENZ regime in the visible spectral region. In the near-infrared (NIR) region, doped semiconducting oxides such as tin-doped indium oxide[12] and aluminum-doped zinc oxide[13] behave as ENZ materials. An ENZ condition is also found in silicon carbide,[14] the perovskite strontium titanate,[15] gallium nitride,[16] and fused silica (SiO_2)[17] in the mid-IR range due to phononic resonances. The zero-permittivity wavelength of a given material is dictated by its intrinsic material properties and hence cannot be used for applications that require that the ENZ condition occurs at some specified wavelength. To address this concern, ENZ metamaterials have been developed for use in the microwave,[18] IR,[2,19] and visible[20,21] spectral regions. In homogeneous Drude materials, the nonlinear enhancement of n_2 and β has been thoroughly examined as a function of wavelength in the ENZ region.[8] Although some work has been done exploring the nonlinear response of ENZ metamaterials,[22−24] its dependence as a function of wavelength has yet to be fully characterized. Doing this allows us to implicitly infer n_2 as a function of ϵ and, thus, interpret the ENZ condition's real contribution to the optical nonlinearity. Here, we examine the nonlinear optical response of an ENZ metamaterial that is straightforward to fabricate and for which the ENZ condition can be flexibly set to any targeted wavelength region. Although the nonlinear enhancement in homogeneous ENZ materials has been well established, it is not clear whether such an enhancement occurs in metamaterials when the *effective* permittivity vanishes. In homogeneous materials such as tin-doped indium oxide, the nonlinear enhancement can be explained by a shift in the plasma frequency by intense laser excitation, which changes the

Received: July 27, 2020
Published: December 11, 2020

permittivity.[12] The refractive index then changes according to $\Delta n = \Delta\epsilon/2\sqrt{\epsilon}$, which has its maximum value at the zero-permittivity wavelength. It has yet to be established whether Δn is maximally changed at the effective zero-permittivity wavelength of a metamaterial. Our work confirms that a metamaterial indeed does exhibit a nonlinear enhancement in its ENZ region, and therefore, ENZ nonlinear enhancement can be placed at any predefined wavelength. We also develop a simple analytic model to explain these results.

Our metamaterial is composed of alternating subwavelength-thick layers of metal and dielectric materials. A schematic diagram of the metamaterial geometry is shown in Figure 1(a).

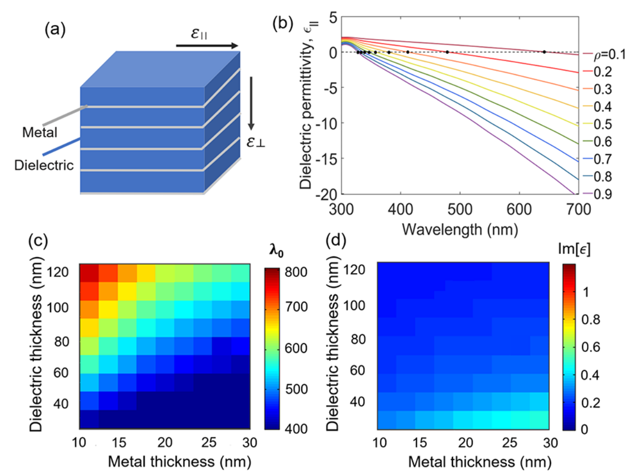

Figure 1. (a) Schematic diagram of a metal–dielectric multilayer stack. (b) Effective parallel permittivities at normal incidence predicted from EMT for different metallic fill fractions (the black circles denote the zero-crossing wavelength for each fill fraction). (c) The zero-permittivity wavelength and (d) the loss of a five-bilayer Ag-SiO_2 multilayer stack calculated using TMM as a function of the thicknesses of the Ag and SiO_2 layers. Note that the zero-permittivity wavelength can be placed anywhere in the visible region.

These metamaterials are capable of exhibiting a zero-permittivity wavelength anywhere within the entire visible spectrum by adjusting the respective thicknesses of the constituent materials.[20,25−27] Provided that the inhomogeneity scale of the composite medium is of subwavelength dimensions, effective medium theory (EMT) predicts that the wavelength, λ_0, at which the permittivity crosses zero can be evaluated from the fill fraction of the constituents in the composite.[25,28] Thus, in the limit of subwavelength layer thickness, the metal–dielectric multilayer stack can be considered as an effective medium with an effective permittivity for an electric field polarized in the plane of the layers given by $\epsilon_{\parallel} = \rho\epsilon_m + (1 - \rho)\epsilon_d$, where ρ is the metallic fill fraction and ϵ_m and ϵ_d are the permittivities of the metal and the dielectric material, respectively.[29] We selected Ag as the metal because of its small damping constant compared to other noble metals,[30] and SiO_2 as the dielectric because of its transparency in the visible spectral region.[31] In Figure 1(b), the fill fraction is varied from $\rho = 0.1$ to 0.9, and we observe a blue shift in the zero-permittivity wavelength as the metallic fill fraction increases. Thus, the dependence of the zero-permittivity wavelength on the metallic fill fraction should enable an ENZ metamaterial design that can be situated anywhere in the entire visible spectrum.

Although effective medium theory can reliably predict the ENZ wavelength under many situations, this method is rigorously valid only under limiting conditions, such as vanishingly small layer thickness and an infinitely thick overall medium.[32] In order to validate our EMT approach, we perform parameter retrieval using the transfer matrix method (TMM) to aid in our design.[33] Using this method, one can solve for the effective refractive index and consequently the complex effective permittivity of a medium. The TMM simulations reveal optimal designs in terms of zero-permittivity wavelength and optical losses (Figure 1(c)). We select a design for the Ag−SiO_2 multilayer stack that has both a desired zero-permittivity wavelength and a small amount of loss, consisting of five bilayers of Ag and SiO_2 with thicknesses of 16 and 65 nm, respectively, for a total thickness of 405 nm. We choose five bilayers because it has been shown that using more than five bilayers produces no appreciable improvement in the nonlinear optical response.[47] Figure 2(a) depicts the dielectric

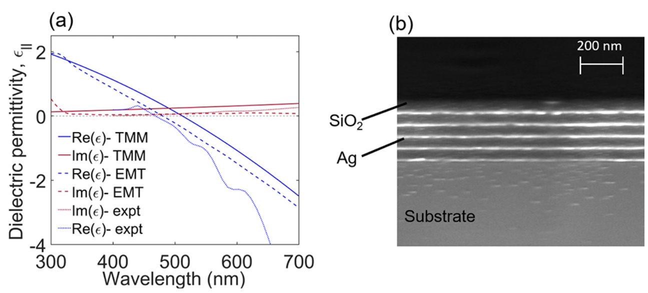

Figure 2. (a) Effective parallel permittivity, $\epsilon_{\parallel}$, at normal incidence calculated using the TMM, EMT, and the measured transmittance for a Ag−SiO_2 multilayer stack with five bilayers of Ag (16 nm) and SiO_2 (65 nm). (b) Cross-sectional image of the fabricated Ag−SiO_2 multilayer stack taken with a scanning electron microscope.

permittivity at normal incidence as a function of wavelength calculated using both the TMM and EMT methods. The optical losses are due to the resistive losses of silver. This geometry corresponds to a metamaterial with an effective zero-permittivity wavelength of 509 nm, with an imaginary part of the dielectric permittivity Im[ϵ] of 0.2.

Having established a preferred design, we fabricated a device for characterization. The Ag and SiO_2 layers were deposited using electron-beam evaporation on a glass substrate. The deposition rates of Ag and SiO_2 layers were kept at a low value of 0.1 nm/s in order to maintain film uniformity. To prevent oxidation, the top layer is the SiO_2 layer. A cross-section of the fabricated sample is shown in Figure 2(b). Our fabricated sample agrees with our design within the usual fabrication tolerances.

■ METHODS

The linear transmittance of the sample was probed using a collimated supercontinuum source covering the visible to NIR spectral range. We compared the measured transmission spectra to those predicted by TMM simulations for various metal and dielectric layer thicknesses. We found the best agreement with the experimental data for a metal−dielectric multilayer stack with thicknesses of 16 nm for Ag and 56 nm for SiO_2 (see Supporting Information for more details). The resulting zero-permittivity wavelength occurs at 470 nm (Figure 2(a)), which is reasonably close to the predicted zero-permittivity wavelength of our device design (509 nm). The small discrepancy between the target zero-crossing wavelength and that determined from these linear characterization measurements could be attributable to fabrication uncertainties, such as layer composition or variations in thickness, or measurement uncertainties in the linear characterization of the device.

We characterized the nonlinear optical properties of our sample using the Z-scan technique.[34] A schematic diagram of the experimental setup is shown in Figure 3(a). We used pump

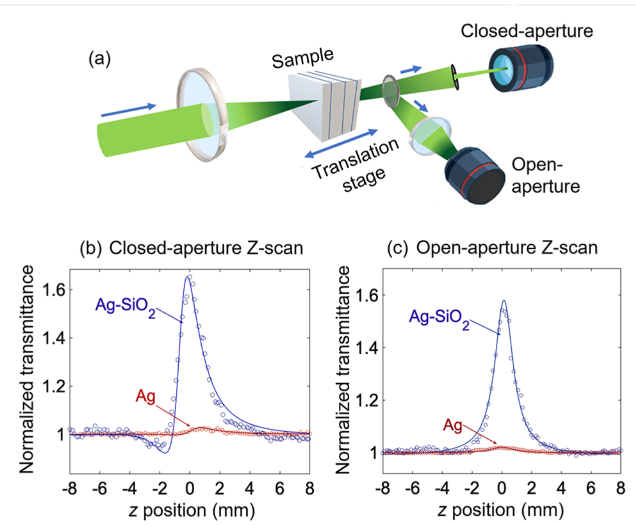

Figure 3. (a) Experimental setup. The Z-scan measurements were performed using 28 ps pulses with a repetition rate of 50 Hz from an optical parametric generator. A spatially filtered Gaussian beam is focused at normal incidence onto the sample by a lens. (b) Closed- and (c) open-aperture Z-scan signals at λ = 500 nm for a Ag−SiO_2 multilayer stack (blue) and a thin-film Ag layer (red) at normal incidence. The solid lines represent theoretical fits to the experimental data.

pulses with a repetition rate of 50 Hz and a pulse duration of 28 ps from an optical parametric generator. Both closed- and open-aperture measurements were performed for wavelengths ranging from 410 to 560 nm. Note that the entire spectral range is in the ENZ region. All the measurements were conducted at normal incidence. As such, we do not expect to excite any surface plasmon polaritons. Figure 3(b) and (c) show, respectively, representative closed-aperture and open-aperture signals from the Ag−SiO_2 multilayer stack at λ = 500 nm. The asymmetry in the closed-aperture signal with respect to the focus is due to the significant nonlinear absorption in the sample.[35,36] We first extracted the imaginary part of the nonlinear phase shift from the open-aperture signal and used this value to calculate the real part of the phase shift from the closed-aperture signal. The extracted values of the real and imaginary nonlinear phase shifts were used in the standard expressions to calculate n_2 and β (see Supporting Information for details).[34] For comparison, Figure 3(b) and (c) also show similar measurements performed under the same conditions for a single 16-nm-thick Ag layer. Near the zero-permittivity wavelength, the accumulated nonlinear phase of the multilayer stack is 22 times larger than that of the 16-nm-thick silver layer, even though the multilayer stack contains only 5 times as much silver.

The nonlinear refractive index n_2 and the nonlinear absorption coefficient β of the Ag−SiO_2 multilayer stack are shown as functions of wavelength in Figure 4(a) and (b). It is

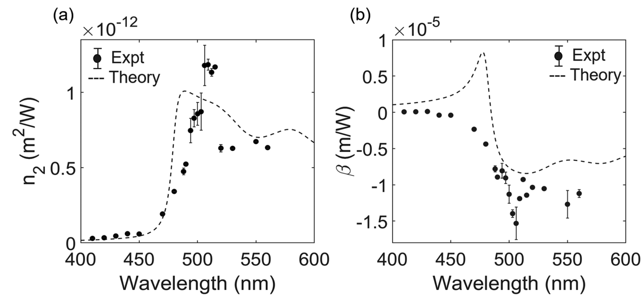

Figure 4. (a) Nonlinear refractive index n_2 and (b) nonlinear absorption coefficient β of the Ag−SiO_2 multilayer stack as a function of wavelength. The dashed lines correspond to predictions from eqs 2 and 3 without any fit parameters.

clear that the nonlinear response is enhanced in the ENZ region of the spectrum, peaking at the zero-permittivity wavelength targeted by this metamaterial design. The maximum measured phase shift at the zero-permittivity wavelength is $0.62\pi \pm 0.05$ rad. For the Ag−SiO_2 multilayer stack, the values of n_2 and β are $(1.2 \pm 0.1) \times 10^{-12}$ m^2/W and $(-1.5 \pm 0.2) \times 10^{-5}$ m/W, respectively. The peak value of the measured n_2 of the Ag−SiO_2 multilayer stack is 10^7 times larger than that of fused silica (3.2×10^{-20} m^2/W)[38] and is 4 times larger than that of an individual 16-nm-thick silver film (3×10^{-13} m^2/W). Due to the noninstantaneous nature of the nonlinearity of metals, we would expect to obtain different values for the nonlinear response for different experimental conditions. For example, we expect that performing the same measurements as reported above with shorter pulses would lead to smaller magnitudes of nonlinearity.[37] However, by performing our measurement with a narrow-band pulse, we are able to measure the nonlinear response across a broad spectral range spanning over the ENZ wavelength for this sample, confirming the existence of clear nonlinear enhancement due to the zero-permittivity wavelength.

RESULTS AND DISCUSSION

We model the nonlinearity of the metamaterial stack using the nonlinear EMT.[39] Here, the effective nonlinear susceptibility of the metamaterial stack is the weighted average of the constituent materials. Since $\chi^{(3)}_{SiO_2}$ is much smaller than $\chi^{(3)}_{Ag}$, according to EMT, the dominant contribution to $\chi^{(3)}_{eff}$ of the metamaterial is from the Ag layers only (e.g., $\chi^{(3)}_{eff} \approx \chi^{(3)}_{Ag} \times \rho$). We assume that $\chi^{(3)}_{Ag}$ is dispersionless over this spectral range. We measured our single silver layer sample at λ = 500 nm and obtained $\chi^{(3)} = (2.42 + 5.15i) \times 10^{-16}$ m^2/V^2, in good agreement with previously measured values.[40,41] The complex nonlinear response $\tilde{n}_2$ of the composite material is given by[38,42,43]

$$\tilde{n}_2 = \frac{3}{4\epsilon_0 c n_0 \mathrm{Re}[n_0]}\chi^{(3)}_{eff} \tag{1}$$

where ϵ_0 is the vacuum permittivity and c is the speed of light in a vacuum. Equation 1 is related to the nonlinear refraction n_2 and the absorption coefficient β by the relations

$$n_2 = \mathrm{Re}[\tilde{n}_2] \tag{2}$$

$$\beta = \frac{4\pi}{\lambda}\mathrm{Im}[\tilde{n}_2] \quad (3)$$

We plot these equations in Figure 4 using the refractive index of our design as calculated by the EMT. The model shows a strong, wavelength-dependent enhancement at the zero-permittivity wavelength that qualitatively resembles the experimental results. It correctly predicts the location and the maximum nonlinear response to within a factor of 2 without the need for any fit parameters or additional factors (e.g., the slow-light factor $S = n_g/n_0$, where n_g is the group index[44,45]). The discrepancies in the breadth and the magnitude of this enhancement at the peak could likely be attributed to dimension variations between the design and the fabricated device, surface effects, imperfections in the constituent layers introduced during deposition, or our assumption that $\chi^{(3)}_{\mathrm{Ag}}$ is dispersionless in our theoretical model. We note that our model predicts an additional peak for β at $\lambda = 475$ nm that we do not reproduce in the measurement and currently cannot account for. The qualitative agreement between such a simple theory and the experimental results suggests that this model may be used to predict and design the nonlinear optical response of other ENZ metamaterials.

In order to study the nature of the enhancement of the nonlinear response, we compare the response of the Ag−SiO_2 multilayer stack directly with that of a single thin film of silver. Given that $\chi^{(3)}_{\mathrm{eff}} \approx \rho \times \chi^{(3)}_{\mathrm{Ag}}$, with $\rho < 1$, any metamaterial stack composed of SiO_2 and Ag layers will exhibit a smaller $\chi^{(3)}$ value than that of silver. However, we found that at its peak the magnitude of n_2 of the metamaterial is 4 times that of silver. This observation implies that the ENZ condition increases n_2 to exceed the value of silver, despite the silver being "diluted" by a material with a lower nonlinearity (i.e., SiO_2). This observation is further validated when comparing n_2 and β of the ENZ metamaterial at its zero-permittivity wavelength ($\lambda = 506$ nm) to these same values when $\epsilon_{\mathrm{eff}} \approx 1$ ($\lambda = 410$ nm; see Figure 2(a)). Here, the magnitudes of n_2 and β are increased in the ENZ region by factors of 40 and 250, respectively. In addition to this ENZ enhancement, at the zero-permittivity wavelength, the metamaterial has a smaller linear loss than silver ($\mathrm{Im}[n_0] = 0.3$ vs 3.1, respectively). Consequently, its effective propagation length can be much longer than that of silver (60 nm vs 9 nm), allowing for a much larger accumulation of nonlinear phase.[46,47] As shown by the peak-to-valley differences in Figure 3(b), in propagating through a five-bilayer Ag−SiO_2 multilayer stack, the beam acquires a nonlinear phase shift that is approximately 22 times larger than that of the individual silver layer (1.53 rad vs 0.068 rad). Therefore, the benefit of using an ENZ metamaterial over a bulk metallic thin film is twofold: due to ENZ enhancement and due to lowered loss.[22,24,46,47]

In conclusion, we have examined the nonlinear optical properties of an ENZ metamaterial realized through the use of a metal−dielectric multilayer stack. This work further confirms that the enhancement of the nonlinear optical response that had previously been observed in homogeneous materials at the zero-permittivity wavelength[12,13] occurs also in metamaterials at the zero of the *effective* permittivity.[22−24] We have observed that these materials produce a large nonlinear optical response and that the dominant mechanism for enhancing this response is the factor $1/(n_0\mathrm{Re}[n_0])$. The ability to obtain strong nonlinearities at designated optical frequencies makes these metamaterials a flexible platform for applications in nonlinear optics.

There exists a broad variety of nonlinear optical phenomena, of which only the Kerr effect and saturable absorption were directly examined in this work. The investigation of other such nonlinear responses[48,49] and their potential enhancement in ENZ metamaterials certainly warrants further study. The fact that this metamaterial geometry is inherently anisotropic could be seen as an advantage for certain future applications and be the topic of future study.

■ ASSOCIATED CONTENT

Supporting Information

The Supporting Information is available free of charge at https://pubs.acs.org/doi/10.1021/acsphotonics.0c01178.

> Linear characterization methods, beam cleaning procedures, retrieval of nonlinear optical coefficients, peculiar features of open- and closed-aperture Z-scan signals, nonlinear phase shift, and additional experimental details (PDF)

■ AUTHOR INFORMATION

Corresponding Author

Orad Reshef − *Department of Physics, University of Ottawa,*

Authors

Sisira Suresh − *Department of Physics, University of Ottawa, Ottawa, ON K1N 6N5, Canada*

M. Zahirul Alam − *Department of Physics, University of Ottawa, Ottawa, ON K1N 6N5, Canada*

Jeremy Upham − *Department of Physics, University of Ottawa, Ottawa, ON K1N 6N5, Canada*

Mohammad Karimi − *School of Electrical Engineering and Computer Science, University of Ottawa, Ottawa, ON K1N 6N5, Canada*

Robert W. Boyd − *Department of Physics, University of Ottawa, Ottawa, ON K1N 6N5, Canada; Institute of Optics and Department of Physics and Astronomy, University of Rochester, Rochester, New York 14627, United States*

Complete contact information is available at: https://pubs.acs.org/10.1021/acsphotonics.0c01178

Notes

The authors declare no competing financial interest.

■ ACKNOWLEDGMENTS

This work was supported in part by the Canada First Research Excellence Fund, the Canada Research Chairs Program, and the Natural Sciences and Engineering Research Council of Canada (NSERC [funding reference number RGPIN/2017-06880]). R.W.B. acknowledges support from DARPA (Grant No. W911NF- 18-0369) and ARO (Grant W911NF-18-1-0337). O.R. acknowledges the support of the Banting Postdoctoral Fellowship from NSERC. Fabrication in this work was performed at the Centre for Research in Photonics at the University of Ottawa (CRPuO).

■ REFERENCES

(1) Silveirinha, M.; Engheta, N. Tunneling of electromagnetic energy through subwavelength channels and bends using ϵ-near-zero materials. *Phys. Rev. Lett.* **2006**, *97*, 157403.

(2) Adams, D. C.; et al. Funneling Light through a Subwavelength Aperture with Epsilon-Near-Zero Materials. *Phys. Rev. Lett.* **2011**, *107*, 133901.

(3) Prain, A.; Vezzoli, S.; Westerberg, N.; Roger, T.; Faccio, D. Spontaneous Photon Production in Time-Dependent Epsilon-Near-Zero Materials. *Phys. Rev. Lett.* **2017**, *118*, 133904.

(4) Alù, A.; Silveirinha, M.; Salandrino, A.; Engheta, N. Epsilon-near-zero metamaterials and electromagnetic sources: Tailoring the radiation phase pattern. *Phys. Rev. B: Condens. Matter Mater. Phys.* **2007**, *75*, 155410.

(5) Ciattoni, A.; Rizza, C.; Palange, E. Transmissivity directional hysteresis of a nonlinear metamaterial slab with very small linear permittivity. *Opt. Lett.* **2010**, *35*, 2130.

(6) Argyropoulos, C.; Chen, P.; D'Aguanno, G.; Engheta, N.; Alù, A. Boosting optical nonlinearities in epsilon-near-zero plasmonic channels. *Phys. Rev. B: Condens. Matter Mater. Phys.* **2012**, *85*, 045129.

(7) Capretti, A.; Wang, Y.; Engheta, N.; Dal Negro, L. Enhanced third-harmonic generation in Si-compatible epsilon-near-zero indium tin oxide nanolayers. *Opt. Lett.* **2015**, *40*, 1500−1503.

(8) Reshef, O.; De Leon, I.; Alam, M. Z.; Boyd, R. W. Nonlinear optical effects in epsilon-near-zero media. *Nature Reviews Materials* **2019**, *4*, 535−551.

(9) Johnson, P. B.; Christy, R. W. Optical Constants of the Noble Metals. *Phys. Rev. B* **1972**, *6*, 4370−4379.

(10) Wen, X.; et al. Doubly Enhanced Second Harmonic Generation through Structural and Epsilon-near-Zero Resonances in TiN Nanostructures. *ACS Photonics* **2018**, *5*, 2087−2093.

(11) Naik, G. V.; Kim, J.; Boltasseva, A. Oxides and nitrides as alternative plasmonic materials in the optical range. *Opt. Mater. Express* **2011**, *1*, 1090−1099.

(12) Alam, M. Z.; De Leon, I.; Boyd, R. W. Large optical nonlinearity of indium tin oxide in its epsilon-near-zero region. *Science* **2016**, *352*, 795−797.

(13) Caspani, L.; et al. Enhanced nonlinear refractive index in epsilon-near-zero materials. *Phys. Rev. Lett.* **2016**, *116*, 233901.

(14) Spitzer, W. G.; Kleinman, D.; Walsh, D. Infrared properties of hexagonal silicon carbide. *Phys. Rev.* **1959**, *113*, 127−132.

(15) Kehr, S. C.; et al. Near-field examination of perovskite-based superlenses and superlens-enhanced probe-object coupling. *Nat. Commun.* **2011**, *2*, 1−9.

(16) Harima, H.; Sakashita, H.; Nakashima, S. Raman microprobe measurement of under-damped LO-phonon-plasmon coupled mode in n-type GaN. *Mater. Sci. Forum* **1998**, *264*, 1363−1366.

(17) Kischkat, J.; et al. Mid-infrared optical properties of thin films of aluminum oxide, titanium dioxide, silicon dioxide, aluminum nitride, and silicon nitride. *Appl. Opt.* **2012**, *51*, 6789−6798.

(18) Edwards, B.; Alù, A.; Young, M. E.; Silveirinha, M.; Engheta, N. Experimental verification of epsilon-near-zero metamaterial coupling and energy squeezing using a microwave waveguide. *Phys. Rev. Lett.* **2008**, *100*, 033903.

(19) Hu, C.; et al. Experimental demonstration of near-infrared epsilon-near-zero multilayer metamaterial slabs. *Opt. Express* **2013**, *21*, 23631−23639.

(20) Subramania, G.; Fischer, A. J.; Luk, T. S. Optical properties of metal-dielectric based epsilon near zero metamaterials. *Appl. Phys. Lett.* **2012**, *101*, 241107.

(21) Maas, R.; Parsons, J.; Engheta, N.; Polman, A. Experimental realization of an epsilon-near-zero metamaterial at visible wavelengths. *Nat. Photonics* **2013**, *7*, 907912.

(22) Neira, A. D.; et al. Eliminating material constraints for nonlinearity with plasmonic metamaterials. *Nat. Commun.* **2015**, *6*, 7757.

(23) Kaipurath, R. M.; et al. Optically induced metal-to-dielectric transition in Epsilon-Near-Zero metamaterials. *Sci. Rep.* **2016**, *6*, 27700.

(24) Rashed, A. R.; Yildiz, B. C.; Ayyagari, S. R.; Caglayan, H. Hot Electron Dynamics in Ultrafast Multilayer Epsilon-Near-Zero Metamaterial. *Phys. Rev. B: Condens. Matter Mater. Phys.* **2020**, *101*, 165301.

(25) Wenshan, C.; Shalaev, V. *Optical Metamaterials*; Springer: New York, 2010; p 10.

(26) Kidwai, O.; Zhukovsky, S. V.; Sipe, J. E. Effective-medium approach to planar multilayer hyperbolic metamaterials: Strengths and limitations. *Phys. Rev. A: At., Mol., Opt. Phys.* **2012**, *85*, 053842.

(27) Newman, W. D.; et al. Ferrell-berreman modes in plasmonic epsilon-near-zero media. *ACS Photonics* **2015**, *2*, 2−7.

(28) Sihvola, A. H. *Electromagnetic Mixing Formulae and Applications*; IET, 1999; Vol. *47*.

(29) Rytov, S. M. Electromagnetic Properties of a Finely Stratified Medium. *Sov. Phys. Jept* **1956**, *2*, 466−475.

(30) West, P. R.; et al. Searching for better plasmonic materials. *Laser and Photonics Reviews* **2010**, *4*, 795−808.

(31) Palik, E. D. *Handbook of Optical Constants of Solids*; Academic Press, 1998; Vol. *3*.

(32) Papadakis, G. T.; Yeh, P.; Atwater, H. A. Retrieval of material parameters for uniaxial metamaterials. *Phys. Rev. B: Condens. Matter Mater. Phys.* **2015**, *91*, 155406.

(33) Smith, D. R.; Vier, D. C.; Koschny, T.; Soukoulis, C. M. Electromagnetic parameter retrieval from inhomogeneous metamaterials. *Phys. Rev. E* **2005**, *71*, 036617.

(34) Sheik-Bahae, M.; Said, A. A.; Wei, T. H.; Hagan, D. J.; Van Stryland, E. W. Sensitive measurement of optical nonlinearities using a single beam. *IEEE J. Quantum Electron.* **1990**, *26*, 760−769.

(35) Liu, X.; Guo, S.; Wang, H.; Hou, L. Theoretical study on the closed-aperture Z -scan curves in the materials with nonlinear refraction and strong nonlinear absorption. *Opt. Commun.* **2001**, *197*, 431−437.

(36) Tsigaridas, G.; Persephonis, P.; Giannetas, V. Effects of nonlinear absorption on the Z-scan technique through beam dimension measurements. *Mater. Sci. Eng., B* **2009**, *165*, 182−185.

(37) Boyd, R. W.; Shi, Z.; De Leon, I. The third-order nonlinear optical susceptibility of gold. *Opt. Commun.* **2014**, *326*, 74−79.

(38) Boyd, R. W. *Nonlinear Optics*, 4th ed.; Academic Press, 2020.

(39) Boyd, R. W.; Sipe, J. E. Nonlinear optical susceptibilities of layered composite materials. *J. Opt. Soc. Am. B* **1994**, *11*, 297−303.

(40) Ma, G.; Tang, S. H. Ultrafast optical nonlinearity enhancement in metallodielectric multilayer stacks. *Opt. Lett.* **2007**, *32*, 3435−3437.

(41) Yang, G.; Guan, D.; Wang, W.; Wu, W.; Chen, Z. The inherent optical nonlinearities of thin silver films. *Opt. Mater.* **2004**, *25*, 439−443.

(42) Sutherland, R. L. *Handbook of Nonlinear Optics*; CRC Press, 2003.

(43) Del Coso, R.; Solis, J. Relation between nonlinear refractive index and third-order susceptibility in absorbing media. *J. Opt. Soc. Am. B* **2004**, *21*, 640−644.

(44) Monat, C.; De Sterke, M.; Eggleton, B. J. Slow light enhanced nonlinear optics in periodic structures. *J. Opt.* **2010**, *12*, 104003.

(45) Boyd, R. W. Material slow light and structural slow light: similarities and differences for nonlinear optics. *J. Opt. Soc. Am. B* **2011**, *28*, A38−A44.

(46) Bennink, R. S.; Yoon, Y.; Boyd, R. W.; Sipe, J. E. Accessing the optical nonlinearity of metals with metal- dielectric photonic bandgap structures. *Opt. Lett.* **1999**, *24*, 1416−1418.

(47) Lepeshkin, N. N.; Schweinsberg, A.; Piredda, G.; Bennink, R. S.; Boyd, R. W. Enhanced nonlinear optical response of one-dimensional metal-dielectric photonic crystals. *Phys. Rev. Lett.* **2004**, *93*, 123902.

(48) Luk, T. S.; et al. Enhanced third harmonic generation from the epsilon-near-zero modes of ultrathin films. *Appl. Phys. Lett.* **2015**, *106*, 151103.

(49) Yang, Y.; et al. High-harmonic generation from an epsilon-near-zero material. *Nat. Phys.* **2019**, *15*, 1022−1026.

ACS Photonics

pubs.acs.org/journal/apchd5 Article

Strongly Coupled Plasmon Polaritons in Gold and Epsilon-Near-Zero Bifilms

Saumya Choudhary,* Saleem Iqbal, Mohammad Karimi, Orad Reshef, M. Zahirul Alam, and Robert W. Boyd

Cite This: *ACS Photonics* 2023, 10, 162−169 Read Online

ACCESS | Metrics & More | Article Recommendations | Supporting Information

ABSTRACT: Epsilon-near-zero (ENZ) polaritons in a thin transparent conducting-oxide film exhibit a significant electric field enhancement and localization within the film at frequencies close to their plasma frequency, but do not propagate. Meanwhile, plasmon polariton modes in thin metallic films can propagate for several microns, but are more loosely confined in the metal. Here, we propose a strongly coupled bilayered structure of a thin gold film on a thin indium tin oxide (ITO) film that supports hybrid polariton modes. We experimentally characterize the dispersion of these modes and show that they have propagation lengths of 4−8 μm while retaining mode confinement greater than that of the polariton in gold films by nearly an order of magnitude. We study the tunability of this coupling strength by varying the thickness of the ITO film and show that ultrastrong coupling is possible at certain thicknesses. The unusual linear and nonlinear optical properties of ITO at ENZ frequencies make these bifilms useful for the active tuning of strong coupling, ultrafast switching, and enhanced nonlinear interactions at near-infrared frequencies.

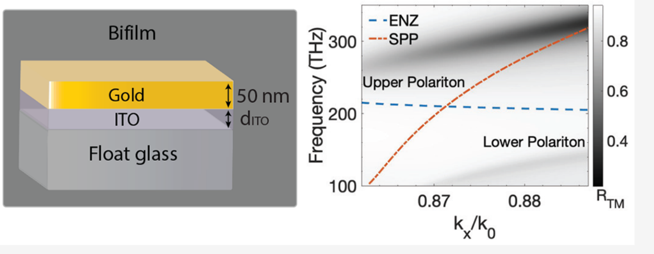

KEYWORDS: *surface plasmon polaritons, epsilon-near-zero, strong coupling, hybridization, field enhancement, nanophotonics*

INTRODUCTION

Two harmonic oscillators become strongly coupled when they exchange energy faster than the rate at which energy decays from the system. The coupled system has eigenstates that are a hybrid of those of the two uncoupled oscillators and which show a characteristic avoided crossing of their dispersion lines around the degeneracy point of the uncoupled oscillators.[1,2] Strong coupling between dipolar oscillators and a cavity has been achieved previously either by reducing the cavity mode volume or by enhancing the oscillator strength.[2−10] Surface plasmon polaritons (SPP) supported by a metal−dielectric interface also have small mode volumes that make them excellent candidates for strong coupling to other localized modes.[2,11,12] SPPs are formed by strong coupling between light and the charge density oscillations in the metal, and they have a large field confinement along the metal−dielectric interface.[13,14] A specific type of SPP mode, called a long-range surface plasmon polariton (LR-SPP), is supported by thin metallic films and can propagate for hundreds of microns.[13−15]

Thin films of transparent conducting oxides (TCO), such as indium tin oxide (ITO), also support polaritons. Close to their plasma frequency, the permittivity of these oxides vanishes, a condition also referred to as "epsilon-near-zero" (ENZ).[16,17] The LR-SPP mode of very thin TCO films is modified such that it has a very large and localized longitudinal field component within the film and, unlike the highly dispersive LR-SPP mode in metallic films, has a flat dispersion line, rendering it non-propagative. This special mode is referred to as the "ENZ" mode.[18] It is a collective excitation of free electrons in the TCO film that is strongly absorptive. There is also considerable recent interest in the unusual linear and nonlinear optical phenomena in the ENZ regime,[17,19] including giant nonlinear optical response[16,20−27] due in part to the relaxation of phase-matching constraints[28,29] and large field enhancements.[20,22] However, the large absorption losses associated with most ENZ materials limit their effective interactions lengths to subwavelength scales. Metamaterial resonators strongly coupled to the ENZ mode of TCO and other doped semiconductor films can enhance the nonlinear response through local field enhancement.[30−33] However, these coupled systems are still limited by their subwavelength interaction lengths. Hence, it is interesting to explore structures that support hybrid modes formed by strong coupling between the ENZ mode and guided modes, such as polaritons. Previous demonstrations of strong coupling between polaritons and the ENZ mode have been performed with phonon polaritons,[34] and with plasmon polaritons[35] at mid-infrared frequencies.

Received: September 7, 2022
Published: January 3, 2023

We propose a bifilm structure consisting of a gold film deposited on a thin ITO film backed by a float glass substrate. This structure supports guided modes at near-infrared (NIR) frequencies. Since the plasma frequency of gold lies in the ultraviolet region, the dispersion lines of the LR-SPP mode in the gold film (the red dot-dashed line in Figure 1(b)) and the ENZ mode in the ITO film (the blue dashed line in Figure 1(b)) cross around the ENZ region of ITO, which occurs at NIR frequencies. When placed in spatial proximity as in the bifilm structure (the inset in Figure 1(c)), these constituent modes couple strongly in this ENZ region with a strength dependent on their spatial overlap. The two hybrid modes thus formed have dispersion lines that show avoided (or anti) crossing, where they have at least an order of magnitude larger confinement in the ITO film than the LR-SPP mode in the gold film. Also, unlike the ENZ mode, they can propagate for several microns because of significantly lower losses. Further, we examine the dependence of coupling strength of the constituent modes on the thickness of the ITO film and show that ultrastrong coupling, wherein their coupling strength becomes comparable to the anticrossing frequency,[36,37] can be achieved at certain thicknesses.

RESULTS AND DISCUSSION

Figure 1(b) shows the reflectance map R_{TM} of TM (or p)-polarized light obtained from transfer matrix method (TMM) simulations of a bifilm made of a 50-nm-thick layer of gold and a 23-nm-thick layer of ITO, whose permittivity (ϵ_{ITO}) spectrum is shown in Figure 1(a). The permittivity of gold determined by Johnson and Christy[38] is used for all the calculations performed here. We use the Kretschmann–Raethar configuration,[13] shown in the inset of Figure 1(c), to excite polaritons along the gold–ITO interface through a high-index N-SF11 prism kept in contact with the gold facet of the sample using an index-matching oil. The dispersion of the coupling prism is excluded in Figure 1(b) by plotting the reflectance spectra in the normalized wavevector (k_x/k_0) and frequency (ν) space. The dispersion lines of the LR-SPP mode (red, dot-dashed) and the ENZ mode (blue, dashed) are obtained from the locus of minima of the reflectance map of a standalone gold film and a standalone ITO film, respectively. The LR-SPP (just called SPP from now on) mode has a strongly wavevector dependent dispersion, while the ENZ mode has a flat dispersion pinned at the ENZ frequency. The two distinct branches of minima in the reflectance map correspond to the two hybrid modes of the bifilm, and they asymptotically approach the dispersion lines of the constituent SPP and ENZ modes away from their avoided crossing point.

We experimentally characterize the dispersion of bifilms through attenuated total reflection spectroscopy measurements. Figure 2(d)−(f) show the measured and Figure 2(a)−(c) the simulated reflectance maps of three bifilm samples A, B, and C, each with a 50-nm-thick gold film and ITO films with thicknesses (d_{ITO}) of 23, 65, and 100 nm, respectively. The three ITO films have similar properties with their ENZ wavelengths at 1.317, 1.363, and 1.357 μm, respectively. See Supplementary Section S1 for their permittivity spectra, and S2 for the experimental details. We observe both the high-frequency (upper) and the low-frequency (lower) polariton branches in the measured (Figure 2(d)) and the simulated (Figure 2(a)) reflectance maps of the thinnest bifilm (A). The simulated maps of bifilms B and C show that the spectral separation between the two polariton branches, henceforth referred to as the "polariton band gap", increases with d_{ITO}.

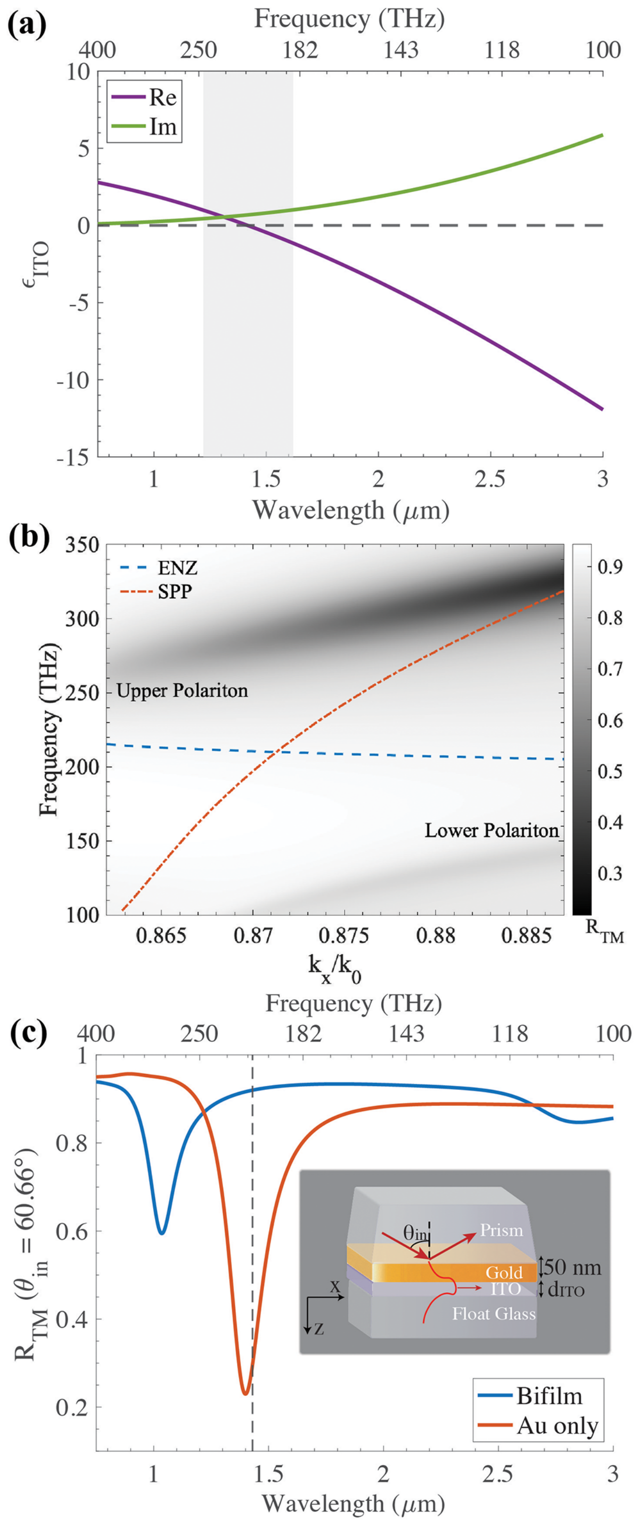

Figure 1. (a) Permittivity spectrum of a representative ITO sample. The grayed region shows the absorption band of the ENZ mode. (b) Simulated reflectance map of TM-polarized light (R_{TM}) for a bifilm (inset in (c)) with a 23-nm-thick film of the same ITO plotted against normalized wavevector ($k_N = k_x/k_0$; k_0 is the propagation constant within the N-SF11 prism used for coupling) and frequency axes. The dispersion lines of the SPP mode (red, solid) and the ENZ mode (dashed, blue) are overlaid. (c) Linecut (blue) of the R_{TM} map in (b) and the R_{TM} spectrum of a standalone gold film (red) at an angle of incidence θ_{in} close to crossing of the SPP and the ENZ dispersion lines.

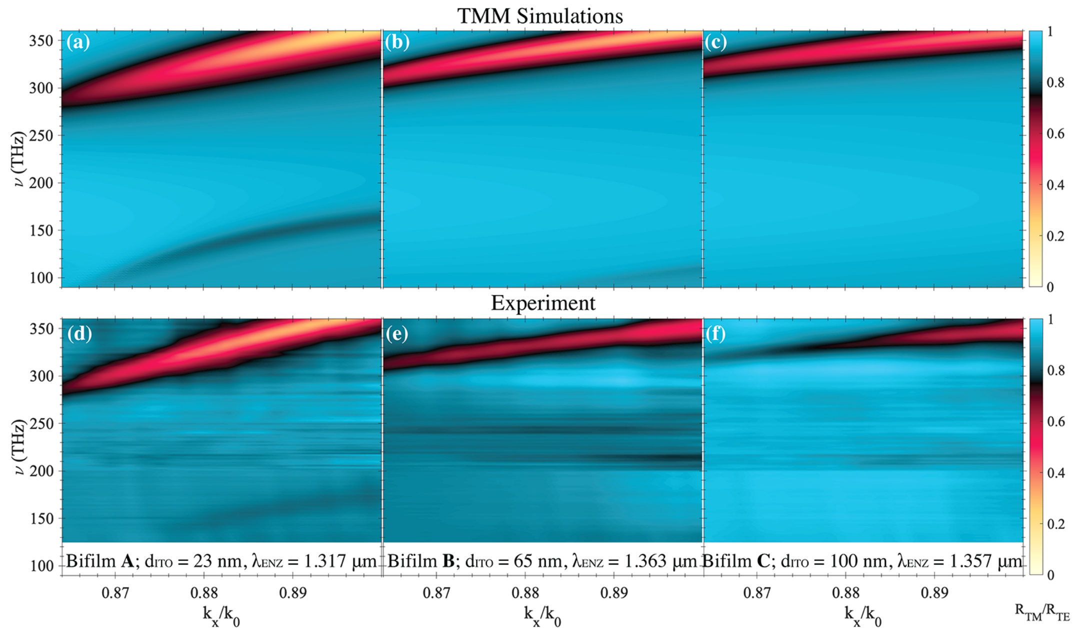

Figure 2. Simulated (top) and measured (bottom) reflectance maps of the three bifilm samples in the $k_x/k_0-\nu$ space. The TM-polarized reflectance spectra R_{TM} are normalized to the TE-polarized spectra R_{TE} at each incident wavevector to exclude measurement artifacts. The range of wavevectors is limited by the critical angle for the prism−substrate interface, and the maximum rotation of the prism−sample assembly is possible without clipping the incoming field.

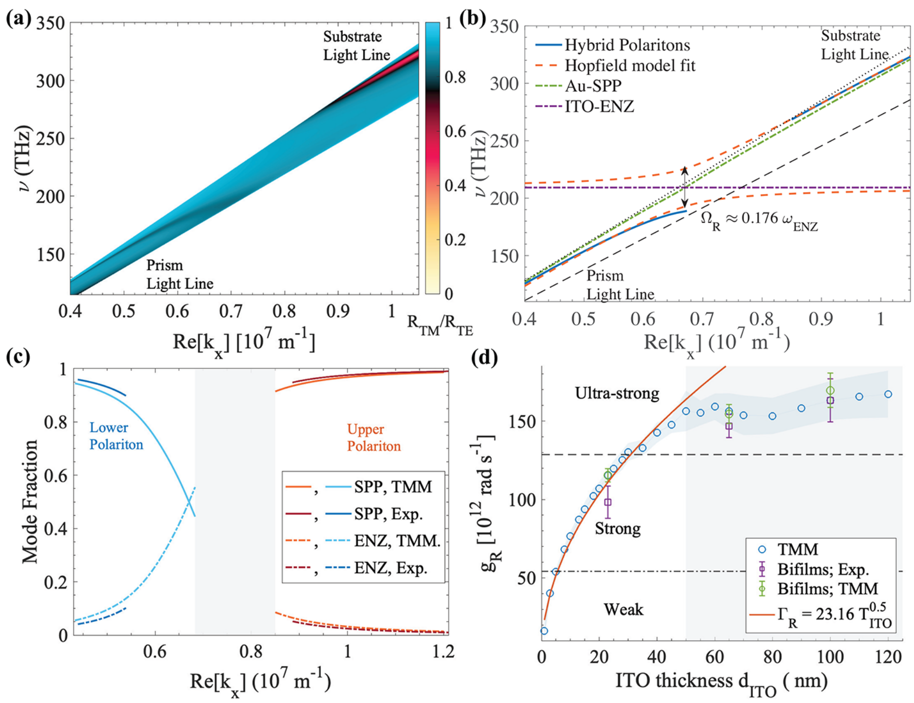

Figure 3. (a) Simulated reflectance map of bifilm A in $k_x-\nu$ space. (b) Dispersion lines of the SPP mode (green, dot-dashed), the ENZ mode (purple, dot-dashed), the hybrid polaritons in bifilm A (blue, solid), and their Hopfield model fits (red, dashed). (c) The SPP (solid) and ENZ (dot-dashed) mode fractions for the upper (red and maroon) and lower (cyan and blue) polaritons. The upper (lower) polariton is formed by a symmetric (antisymmetric) superposition of the constituent modes. (d) g_R for bifilms with various values of d_{ITO} estimated from the simulated (green circles) and measured (purple squares) reflectance maps of bifilms A, B, and C and the simulated reflectance maps of bifilms with ϵ_{ITO} assumed to be the same as in bifilm A (blue circles). The error bars for estimated g_R from simulations for $d_{ITO} < 80$ nm and from measurements for bifilm A are given by the difference in g_R from fitting the upper and the lower polariton dispersion lines. The 95% confidence intervals for g_R estimated from fitting only the upper polariton dispersion line form the error bars for estimated g_R from simulations for $d_{ITO} \geq 80$ nm and from measurements for bifilms B and C. The red line is the parabolic fit to g_R outside the gray region in which the Hopfield model yields large fitting errors.

As an aside, we note that polaritons are said to be critically coupled when the coupling losses are balanced by the absorption losses.[13] The polariton band gap for all three bifilms is large enough that while the upper polariton is coupled efficiently and has a prominent resonance dip, the lower polariton with its comparatively smaller resonance dip is not coupled as efficiently.

This inefficient coupling and large absorption losses of the lower polariton contribute to its visibility being smaller than the upper polariton. For bifilm C, the lower polariton branch is not visible in Figure 2(c). However, it becomes more prominent if the absorption losses within ITO are reduced. See Section S4 in the Supporting Information for more details. The measured reflectance maps of bifilms B and C do not show the lower polariton branch, as we are limited by the spectral range of our spectrometers and white light source. However, the measured and the simulated maps for all three bifilms are in reasonable agreement in the spectral range shown here.

For an insight into the formation of these hybrid polaritons, we analytically model the bifilm as a system of two coupled harmonic oscillators that describe the constituent SPP and ENZ modes. With $\tilde{\omega}_{SPP}(k_x)$ and $\tilde{\omega}_{ENZ}(k_x)$ being the dispersion relations of the two oscillators in the complex angular frequency $\tilde{\omega}$ and real transverse wavevector k_x space, we write the interaction Hamiltonian of the coupled system in the rotating wave approximation as[39,40]

$$\hat{H}(k_x) = \begin{bmatrix} \tilde{\omega}_{SPP}(k_x) & g_R \\ g_R & \tilde{\omega}_{ENZ}(k_x) \end{bmatrix} \tag{1}$$

where g_R is the coupling strength, also known as the vacuum Rabi splitting. The complex frequency $\tilde{\omega}_l(k_x) = \omega_l(k_x) - i\gamma_l(k_x)$, where l = {SPP, ENZ}, ω_l is the resonance frequency of mode l at wavevector k_x and $\gamma_l(k_x)$ is the associated damping. The eigenfrequencies $\tilde{\omega}_{U,L}(k_x)$ of $\hat{H}(k_x)$ (also known as the Hopfield or Hopfield−Bogliubov matrix[34,39]) form the dispersion relations of the hybrid modes and are given by

$$\tilde{\omega}_{U,L} = \frac{\tilde{\omega}_{SPP} + \tilde{\omega}_{ENZ} \pm \sqrt{(\tilde{\omega}_{SPP} - \tilde{\omega}_{ENZ})^2 + 4g_R^2}}{2} \tag{2}$$

where the suffixes U and L denote the upper and lower polaritons, respectively. The eigenvectors of $\hat{H}(k_x)$ are also know as Hopfield coefficients, and their squared modulus denotes the relative mode fractions of the constituent SPP and ENZ modes in the hybrid polaritons at each k_x.

We calculate the dispersion lines $\tilde{\omega}_{U,L}(k_x)$ and $\tilde{\omega}_{SPP}(k_x)$ from their respective reflectance maps in the un-normalized wavevector (k_x) and frequency (ν) space by fitting an "asymmetric" Lorentzian with a frequency-dependent line width (eqs 1 and 2 in the Supporting Information) to the reflectance spectrum at each k_x. The prism dispersion reshapes the reflectance maps in the k_x/k_0−ν space (Figure 2(a) for bifilm A, for example), so as to confine them between the light lines of the prism and the substrate (Figure 3(a) for bifilm A) in the k_x−ν space. The polaritons thus have a positive group velocity.

For the ENZ mode, we assume a flat dispersion line[18] as follows:

$$\tilde{\omega}_{ENZ}(k_x) = \omega_{0,ENZ} - \frac{i}{2}\gamma_{ITO} \tag{3}$$

where $\omega_{0,ENZ}$ is the ENZ mode frequency and γ_{ITO} is the damping in the Drude model of the permittivity of ITO, which is written as

$$\epsilon_{ITO}(\omega) = \epsilon_\infty - \frac{\omega_p^2}{\omega(\omega + i\gamma_{ITO})} \tag{4}$$

Here, ϵ_∞ is the asymptotic value of permittivity for frequencies much larger than the ENZ frequency, ω_p is the plasma frequency, and we have neglected nonlocal contributions to $\epsilon_{ITO}(\omega)$.[41] For the ITO in bifilm A, ϵ_∞ = 3.901, ω_p = 2.8533 × 10^{15} rad s^{-1}, and γ_{ITO} = 2.116 × 10^{14} rad s^{-1}. For the ITO in bifilm B, ϵ_∞ = 3.6914, ω_p = 2.6667 × 10^{15} rad s^{-1}, and γ_{ITO} = 1.193 × 10^{14} rad s^{-1}. And for the ITO in bifilm C, ϵ_∞ = 3.7359, ω_p = 2.6948 × 10^{15} rad s^{-1}, and γ_{ITO} = 1.289 × 10^{14} rad s^{-1}. We calculate g_R by performing a nonlinear least-squares fit of the hybrid polariton dispersion lines to their Hopfield model expressions in eq 2. Since our assumption of a flat $\tilde{\omega}_{ENZ}(k_x)$ pinned at the ENZ frequency of ITO is not accurate for all d_{ITO} considered here, we take $\omega_{0,ENZ}$ to be an adjustable parameter and minimize the difference in g_R obtained from fitting the upper and the lower polariton. See Section S4 in the Supporting Information for details.

Figure 3(b) shows the simulated dispersion lines of the hybrid polaritons of bifilm A (blue, solid), their Hopfield model fits (red, dashed), and the dispersion lines of SPP (green, dot-dashed) and ENZ modes (purple, dot-dashed). The Hopfield fits plotted for all k_x agree reasonably well with the simulated bifilm dispersion, and they clearly show the avoided crossing. The estimated value of g_R for bifilm A from the fits is 115.5 ± 4.3 × 10^{12} rad s^{-1} and, being significantly larger than the average decay rate of the constituent modes γ_{avg} [= $(\gamma_{SPP} + \gamma_{ENZ})/2 \approx 54$ × 10^{12} rad s^{-1}], clearly satisfies the strong coupling criterion. The polariton band gap Ω_R (= $2g_R$) is approximately $0.176\omega_{0,ENZ}$, which is close to the ultrastrong coupling threshold where $\Omega_R \geq 0.2\omega_{0,ENZ}$.[36,37] Above this threshold, depolarization effects within the ITO film and the related counter-rotating terms, which are not included in our calculation of g_R, become significant.[42]

From the Hopfield fit to the upper polariton mode, we note that its avoided crossing is pushed to the left of the substrate light line due to the dispersion of the coupling prism and is therefore not accessible. Hence, only its mostly SPP-like tail lies between the two light lines. The predominantly SPP-like nature of the upper polariton is also evident in its mode composition, which, as shown in Figure 3(c), has an SPP fraction larger than 0.9 throughout. We also note from Figure 3(c) that the ENZ mode contribution for both hybrid polaritons increases closer to the avoided crossing. Comparing the simulated dispersion line of the lower polariton and its Hopfield fit in Figure 3(b), we note that its dispersion line is not well-defined for wavevectors beyond the avoided crossing as a consequence of its largely ENZ-like nature at those wavevectors. Here, both the spectral line width and the wavevector uncertainty of the reflectance dip broaden as the absorption losses increase and the dispersion flattens.[2,3]

Since the spatial overlap between SPP and ENZ modes in the bifilm determines g_R (and Ω_R), it can be varied using the material and geometrical parameters of the ITO film. The SPP mode is confined to the gold−ITO interface with a long evanescent tail extending into the substrate, while the ENZ mode is mostly constant and localized to the ITO film. Hence, as we observe in Figure 2, Ω_R initially increases with d_{ITO}. Figure 3(d) shows the estimated g_R for various values of d_{ITO}. For d_{ITO} smaller than 7 nm, g_R increases almost linearly but remains below the strong coupling threshold. Above this threshold, g_R is proportional to $\sqrt{d_{ITO}}$, as shown by the fitted curve (red, solid), and exceeds the ultrastrong coupling threshold for d_{ITO} larger than 30 nm. The major factor determining this scaling is that the ENZ mode

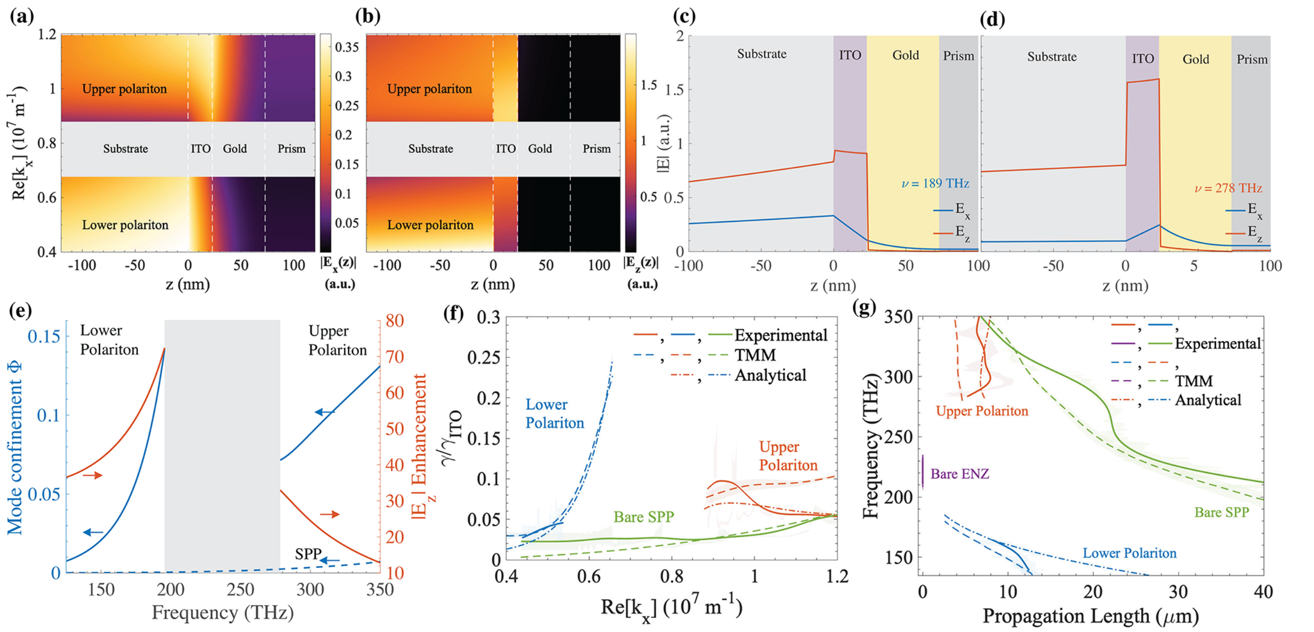

Figure 4. Profiles of (a) $|E_x|$ and (b) $|E_z|$ for bifilm A plotted along the dispersion lines of the hybrid polaritons. The polariton band gap is shown in gray, and the interfaces by the white dashed lines. Field distributions of $|E_x|$ (blue) and $|E_z|$ (red) for the (c) lower and the (d) upper polariton at the edges of the band gap. (e) Mode confinement of the same hybrid polaritons (blue, solid) and the SPP mode (blue, dashed) and their longitudinal field enhancement in ITO with respect to the field in gold at the gold−ITO interface (red). (f) Damping γ normalized to the decay constant in the Drude model of ITO γ_{ITO} and the (g) propagation lengths of the upper (red) and lower (blue) polaritons of bifilm A, the SPP mode in an isolated 50-nm-thick gold film (green), and the ENZ mode in an isolated 23-nm-thick ITO film (purple). In (f) and (g), the dot-dashed lines are the solutions of the analytical dispersion relation, and the solid (experiment) and the dashed (TMM simulations) lines are the line widths of the dips in the respective reflectance maps smoothed over their fitting errors (shaded areas around the lines).

becomes more LR-SPP-like as d_{ITO} increases, and the E_z field within the ITO film is no longer constant.[18] Furthermore, the ENZ mode is a collective excitation of the free electrons within the ITO film with an oscillator strength f_{ENZ} that scales with d_{ITO}. Since g_R is proportional to $\sqrt{f_{ENZ}}$,[2,34] g_R should scale with $\sqrt{d_{ITO}}$. For d_{ITO} larger than 45 nm, g_R saturates and deviates from the $\sqrt{d_{ITO}}$ dependence as the ENZ mode transforms into an LR-SPP mode at these thicknesses, and its dispersion can no longer be approximated by a flat line given by eq 3. We have identified this range of d_{ITO} by a shaded gray region in Figure 3(d), and the values of g_R extracted from the analytical model in this region are not accurate, which is also reflected in the large fitting errors (blue shaded area) in this region. For d_{ITO} larger than 65 nm, the fields at the two interfaces of the ITO film also start to decouple, and the hybrid polaritons morph into polaritonic modes confined at these interfaces.[34] Thus, $d_{ITO} \leq$ 45 nm provides an upper limit to g_R that can be achieved with modes that inherit the desirable features of both the ENZ mode and the SPP mode. See Sections S5 and S7 in the Supporting Information for further discussion.

The relevance of these hybrid polaritons to photonic applications can be examined through parameters such as their mode confinement, field enhancement, propagation lengths, and decay rates. Following the method described in appendix B of ref 43 we first develop an analytical dispersion model for the polaritons and then use its solutions to calculate their field profiles, mode confinement, and field enhancement. See Sections S6 and S7 in the Supporting Information for details on these calculations. We restrict our discussion from now on to bifilm A. Section S9 in the Supporting Information has details on the polaritons in bifilms B and C. Figure 4(a) and (b) show the transverse $|E_x|$ and the longitudinal $|E_z|$ electric field profiles, respectively, of the polaritons in bifilm A plotted at various k_x along their dispersion lines. From the continuity of the longitudinal component of the electric flux density D_z at the gold−ITO interface, we have $E_{z,ITO} = (\epsilon_{Au}/\epsilon_{ITO})E_{z,Au}$, where $E_{z,ITO}$ ($E_{z,Au}$) is the longitudinal electric field inside ITO (gold) at the interface and ϵ_{ITO} (ϵ_{Au}) is its permittivity. As ϵ_{ITO} vanishes close to the avoided crossing, E_z is significantly enhanced within the ITO film and relayed from the gold−ITO interface to the substrate while maintaining its large amplitude.[18,44,45] Away from the avoided crossing, both polaritons become more SPP-like with a smaller E_z in ITO and E_x confined along the ITO−substrate (gold−ITO) interface for the lower (upper) polariton. Figure 4(c) and (d) show the mode profiles of $|E_x|$ (blue) and $|E_z|$ (red) of the upper and the lower polariton, respectively, at the edges of the band gap (the gray region in Figure 4(a) and (b)). The hybrid nature of the modes is evident in the large amplitude of $|E_z|$ within ITO and an enhanced $|E_x|$ at the edges of the ITO film.

Figure 4(e) shows the enhancement in E_z for the hybrid polaritons in bifilm A, which is defined as $|E_z|$ at the center of the ITO film normalized to the $|E_z|$ in gold near the gold−ITO interface (red, solid). We note that the lower (upper) polariton can have a field enhancement as large as 75× (32×) close to the avoided crossing. We now define the mode confinement Φ as follows:[46]

$$\Phi = \frac{\int_d |E_z(z)H_y(z)|dz}{\int_{-\infty}^{\infty} |E_z(z)H_y(z)|dz} \tag{5}$$

where[43] $H_y(z) = (\omega\epsilon(z))/(\mu_0 c k_x)E_z(z)$ is the magnetic field and d denotes the integration range of z. For the bifilm, we calculate

Φ only within the ITO layer, whereas we calculate Φ within the gold layer for the standalone SPP mode and within the ITO layer for the standalone ENZ mode. Figure 4(e) shows the variation of Φ for the polaritons in bifilm A (blue, solid) and the SPP mode in the standalone gold film (blue, dashed). We observe that although Φ for both hybrid polaritons is lower than the bare ENZ mode ($\approx$0.3, not shown here), they substantially outperform the bare SPP mode throughout the spectral region of interest with values of Φ approaching 0.14 (0.075), close to avoided crossing for the lower (upper) polariton. This relaxation in mode confinement makes the hybrid polaritons less lossy compared to the ENZ mode, which is reflected in their reduced damping and enhanced propagation lengths.

Figure 4(f) shows the damping γ ($= |\mathrm{Im}[\tilde{\omega}]|$), and Figure 4(g) the propagation lengths ($= 1/(2\mathrm{Im}[k_x])$) of the upper (red) and the lower (blue) polaritons of bifilm A, the SPP mode in the standalone gold film (green), and the ENZ mode in the standalone ITO film (purple). Asymmetric Lorentzians fitted to the spectral dips at each $\mathrm{Re}[k_x]$ in the experimental (solid) and the simulated (dashed) reflectance maps yield γ, while the fits to the wavevector scans at each frequency yield $\mathrm{Im}[k_x]$. See Sections S5 and S8 in the Supporting Information for details on these fits. The values of γ and $\mathrm{Im}[k_x]$ in the analytical dispersion model (dot-dashed) are given by the imaginary part of the complex frequency and the complex wavevector solutions to the dispersion relation for each $\mathrm{Re}[k_x]$ and $\mathrm{Re}[\tilde{\omega}]$, respectively. The estimated damping and propagation lengths in both the simulated and the experimental data sets have a reasonable agreement in the presence of fitting errors and differences between the simulated and experimental optical constants. The results from the analytical model exclude the radiative losses into the coupling prism.[13] The hybrid polaritons have a significantly lower damping throughout compared to the ENZ mode, which has a constant damping of $0.5\gamma_{\mathrm{ITO}}$ (not shown in Figure 4(f)).[18] Additionally, the lower (upper) polariton has a propagation length between 2 and 15 μm (4−8 μm) for bifilm A, which is significantly larger than the propagation length of the ENZ mode ($\approx$ 0.08 μm for the 23-nm-thick ITO film). The damping (propagation length) of the lower polariton is maximized (minimized) close to the avoided crossing and approaches the values for the SPP mode away from it.

CONCLUSION

To summarize, we have proposed a bifilm structure consisting of a 50-nm-thick gold film deposited on a thin ITO film backed by a float glass substrate that supports hybrid polaritons formed by strong coupling between the SPP mode in the gold film and the ENZ mode in the ITO film at NIR frequencies. These polaritons have a much tighter mode confinement than the bare SPP mode, along with a propagation length of several microns in contrast to the nonpropagating ENZ mode. The large mode confinement of these polaritons is accompanied by a significant enhancement in the longitudinal component of the electric field within the ITO film. The coupling between the constituent modes can be tuned through the thickness of the ITO layer and can even approach the ultrastrong coupling regime at certain thicknesses.

A propagation length of several microns implies an interaction length of several wavelengths at these NIR frequencies. This large interaction length along with the tight mode confinement and the large sub-picosecond nonlinear response of ITO in its ENZ region[16] make our device an ideal platform for electro-optical control of strong coupling,[47] ultrafast switching,[48] and studying giant ultrafast nonlinearities that do not rely on lossy optical resonances or require sophisticated fabrication techniques. The use of a prism for coupling to the polaritons can also be done away with through the use of appropriate grating couplers.[49] The ultrafast response of ITO should also allow for the observation of effects due to time refraction and adiabatic frequency conversion[50−52] and exotic effects related to ultrastrong coupling phenomena, such as the dynamic Casimir effect.[53]

METHODS

Sample Fabrication. The bifilm samples were fabricated by depositing a 50-nm-thick layer of gold on commercially available ITO films on a float glass substrate through thermal evaporation. First, the ITO films were cleaned through the use of acetone + extreme sonication followed by IPA + extreme sonication to remove most of the contamination over the surface that could lead to the undesired scattering of the surface waves. A thermal source was then used to evaporate the gold at a constant rate until a 50 nm layer of Au accumulated over the samples under a high vacuum. No adhesion layer was used between the gold layer and the substrate. Attenuated total reflection spectroscopy in a Kretschmann configuration was used to characterize the dispersion of the fabricated samples by measuring their reflectance maps. The schematic of the setup used for measurements is shown in Figure S2 in Section S2 of the Supporting Information along with the measurement details.

Simulations and Analytical Modeling. The TMM simulations were performed using our home-built MATLAB code. The dispersion of gold, ITO, float glass, and prism were included by using their respective frequency-dependent permittivities. We used the data from Johnson and Christy for the permittivity of gold.[38] The permittivity spectra of the ITO samples used in the three bifilms are shown in Figure S1(a)−(c) in the Supporting Information. The permittivity of Schott N-BK7 was used for the float glass substrate.

The dispersion of the hybrid polaritons in the bifilms was analytically modeled through use of the method described in Appendix B of ref 43. The electric field in each layer was given by a coherent sum of evanescent wave-like forward and backward propagating guided solutions. The field continuity relations at each interface of the structure yielded a set of eight linear homogeneous equations for the field coefficients in each layer, which could be written in the matrix form. The analytical dispersion was obtained by minimizing the determinant of this coefficient matrix in either the complex frequency and real wavevector space or the real frequency and complex wavevector space using the Nelder−Mead method. The field coefficients were obtained through singular value decomposition of the coefficient matrix at each solution in the complex frequency and real wavevector space obtained from the analytical dispersion model. The mode profiles were then calculated by substituting the field coefficients in the aforementioned expressions for the electric field distributions in each layer. See Sections S6 and S7 in the Supporting Information for more details on the analytical model.

ASSOCIATED CONTENT

Supporting Information

The Supporting Information is available free of charge at https://pubs.acs.org/doi/10.1021/acsphotonics.2c01412.

Permittivity spectra of ITO used in the bifilm samples; setup diagram and measurement details; simulated and measured reflectance maps of standalone gold and standalone ITO films; discussion on the relatively smaller visibility of the lower polariton branch; description of the procedure to estimate the coupling strength g_R; details of the analytical dispersion model used to calculate the field profiles of the polaritons; description of the procedure to calculate the field profiles and discussion of the field profiles of bifilms B and C; description of the model used to estimate propagation lengths of the polaritons from their reflectance maps (PDF)

AUTHOR INFORMATION

Corresponding Author

Saumya Choudhary — *Institute of Optics, University of*

Authors

Saleem Iqbal — *Institute of Optics, University of Rochester, Rochester, New York 14627, United States*

Mohammad Karimi — *Department of Physics, University of Ottawa, Ottawa, Ontario K1N 6N5, Canada*

Orad Reshef — *Department of Physics, University of Ottawa, Ottawa, Ontario K1N 6N5, Canada*; orcid.org/0000-0001-9818-8491

M. Zahirul Alam — *Department of Physics, University of Ottawa, Ottawa, Ontario K1N 6N5, Canada*

Robert W. Boyd — *Institute of Optics, University of Rochester, Rochester, New York 14627, United States; Department of Physics, University of Ottawa, Ottawa, Ontario K1N 6N5, Canada*; orcid.org/0000-0002-1234-2265

Complete contact information is available at:
https://pubs.acs.org/10.1021/acsphotonics.2c01412

Funding

The portion of the work performed at the University of Rochester was supported by the US Defense Advanced Research Projects Agency award W911NF-18-1-0369, US Army Research Office award W911NF-18-1-0337, the US Office of Naval Research MURI award N00014-20-1-2558, the US National Science Foundation Award 2138174, and the Department of Energy award FWP 76295. The portion of the work performed at the University of Ottawa was supported by the Canada First Research Excellence Fund Award 072623, the Canada Research Chairs program award 950-231657, the Banting Postdoctoral Fellowships program, and the Natural Sciences and Engineering Research Council of Canada under Discovery Grant RGPIN/2017-06880.

Notes

The authors declare no competing financial interest.

ACKNOWLEDGMENTS

The authors thank A. N. Black, J. W. Kuper, Y. Zhou, and B. Braverman for helpful discussions.

REFERENCES

(1) Novotny, L. Strong coupling, energy splitting, and level crossings: A classical perspective. *Am. J. Phys.* **2010**, *78*, 1199−1202.

(2) Törmä, P.; Barnes, W. L. Strong coupling between surface plasmon polaritons and emitters: a review. *Rep. Prog. Phys.* **2015**, *78*, 013901.

(3) Agranovich, V. M.; Litinskaia, M.; Lidzey, D. G. Cavity polaritons in microcavities containing disordered organic semiconductors. *Phys. Rev. B* **2003**, *67*, 085311.

(4) Yoshie, T.; Scherer, A.; Hendrickson, J.; Khitrova, G.; Gibbs, H.; Rupper, G.; Ell, C.; Shchekin, O.; Deppe, D. Vacuum Rabi splitting with a single quantum dot in a photonic crystal nanocavity. *Nature* **2004**, *432*, 200−203.

(5) Reithmaier, J. P.; Sek, G.; Löffler, A.; Hofmann, C.; Kuhn, S.; Reitzenstein, S.; Keldysh, L.; Kulakovskii, V.; Reinecke, T.; Forchel, A. Strong coupling in a single quantum dot−semiconductor microcavity system. *Nature* **2004**, *432*, 197−200.

(6) Ameling, R.; Giessen, H. Cavity plasmonics: large normal mode splitting of electric and magnetic particle plasmons induced by a photonic microcavity. *Nano Lett.* **2010**, *10*, 4394−4398.

(7) Shelton, D. J.; Brener, I.; Ginn, J. C.; Sinclair, M. B.; Peters, D. W.; Coffey, K. R.; Boreman, G. D. Strong coupling between nanoscale metamaterials and phonons. *Nano Lett.* **2011**, *11*, 2104−2108.

(8) Askenazi, B.; Vasanelli, A.; Delteil, A.; Todorov, Y.; Andreani, L.; Beaudoin, G.; Sagnes, I.; Sirtori, C. Ultra-strong light−matter coupling for designer Reststrahlen band. *New J. Phys.* **2014**, *16*, 043029.

(9) Yoo, D.; de León-Pérez, F.; Pelton, M.; Lee, I. H.; Mohr, D. A.; Raschke, M. B.; Caldwell, J. D.; Martín-Moreno, L.; Oh, S. H. Ultrastrong plasmon−phonon coupling via epsilon-near-zero nanocavities. *Nat. Phot.* **2021**, *15*, 125.

(10) Baranov, D. G.; Munkhbat, B.; Zhukova, E.; Bisht, A.; Canales, A.; Rousseaux, B.; Johansson, G.; Antosiewicz, T. J.; Shegai, T.Ultrastrong coupling between nanoparticle plasmons and cavity photons at ambient conditions. *Nat. Commun.***2020**, *11*, DOI: 10.1038/s41467-020-16524-x.

(11) Santhosh, K.; Bitton, O.; Chuntonov, L.; Haran, G. Vacuum Rabi splitting in a plasmonic cavity at the single quantum emitter limit. *Nat. Commun.* **2016**, *7*, 1−5.

(12) Leng, H.; Szychowski, B.; Daniel, M.-C.; Pelton, M. Strong coupling and induced transparency at room temperature with single quantum dots and gap plasmons. *Nat. Commun.* **2018**, *9*, 1−7.

(13) Novotny, L.; Hecht, B.*Principles of Nano-optics*; Cambridge University Press, 2012; pp 369−388.

(14) Maier, S. A. Plasmonic field enhancement and SERS in the effective mode volume picture. *Opt. Exp.* **2006**, *14*, 1957.

(15) Berini, P.Plasmon-polariton waves guided by thin lossy metal films of finite width: Bound modes of asymmetric structures. *Phys. Rev. B***2001**, *63*, DOI: 10.1103/PhysRevB.63.125417.

(16) Alam, M. Z.; Alam, M. Z.; Leon, I. D.; Boyd, R. W. Large optical nonlinearity of indium tin oxide in its epsilon-near-zero region. *Science* **2016**, *0330*, 0−5.

(17) Reshef, O.; De Leon, I.; Alam, M. Z.; Boyd, R. W. Nonlinear optical effects in epsilon-near-zero media. *Nat. Rev. Mater.* **2019**, *4*, 535−551.

(18) Campione, S.; Brener, I.; Marquier, F. Theory of epsilon-near-zero modes in ultrathin films. *Phys. Rev. B* **2015**, *91*, 121408.

(19) Liberal, I.; Engheta, N. Near-zero refractive index photonics. *Nat. Phot.* **2017**, *11*, 149−158.

(20) Caspani, L.; Kaipurath, R.; Clerici, M.; Ferrera, M.; Roger, T.; Kim, J.; Kinsey, N.; Pietrzyk, M.; Di Falco, A.; Shalaev, V. M.; et al. Enhanced nonlinear refractive index in ϵ-near-zero materials. *Phys. Rev. Lett.* **2016**, *116*, 233901.

(21) Wang, W.; Xu, J.; Liu, X.; Jiang, Y.; Wang, G.; Lu, X. Second harmonic generation investigation of indium tin oxide thin films. *Thin Solid Films* **2000**, *365*, 116−118.

(22) Capretti, A.; Wang, Y.; Engheta, N.; Dal Negro, L. Comparative Study of Second-Harmonic Generation from Epsilon-Near-Zero Indium Tin Oxide and Titanium Nitride Nanolayers Excited in the Near-Infrared Spectral Range. *ACS Photonics* **2015**, *2*, 1584−1591.

(23) Luk, T. S.; De Ceglia, D.; Liu, S.; Keeler, G. A.; Prasankumar, R. P.; Vincenti, M. A.; Scalora, M.; Sinclair, M. B.; Campione, S. Enhanced third harmonic generation from the epsilon-near-zero modes of ultrathin films. *Appl. Phys. Lett.* **2015**, *106*, 151103.

(24) Yang, Y.; Lu, J.; Manjavacas, A.; Luk, T. S.; Liu, H.; Kelley, K.; Maria, J.-P.; Runnerstrom, E. L.; Sinclair, M. B.; Ghimire, S.; et al. High-

harmonic generation from an epsilon-near-zero material. *Nat. Phys.* **2019**, *15*, 1022−1026.
(25) Suresh, S.; Reshef, O.; Alam, M. Z.; Upham, J.; Karimi, M.; Boyd, R. W. Enhanced nonlinear optical responses of layered epsilon-near-zero metamaterials at visible frequencies. *ACS Photonics* **2021**, *8*, 125−129.
(26) Sarma, R.; Nookala, N.; Reilly, K. J.; Liu, S.; de Ceglia, D.; Carletti, L.; Goldflam, M. D.; Campione, S.; Sapkota, K.; Green, H.; et al. Strong Coupling in All-Dielectric Intersubband Polaritonic Metasurfaces. *Nano Lett.* **2021**, *21*, 367.
(27) Deng, J.; Tang, Y.; Chen, S.; Li, K.; Zayats, A. V.; Li, G. Giant enhancement of second-order nonlinearity of epsilon-near-zero medium by a plasmonic metasurface. *Nano Lett.* **2020**, *20*, 5421−5427.
(28) Suchowski, H.; O'Brien, K.; Wong, Z. J.; Salandrino, A.; Yin, X.; Zhang, X. Phase mismatch−free nonlinear propagation in optical zero-index materials. *Science* **2013**, *342*, 1223−1226.
(29) Gagnon, J. R.; Reshef, O.; Espinosa, D. H.; Alam, M. Z.; Vulis, D. I.; Knall, E. N.; Upham, J.; Li, Y.; Dolgaleva, K.; Mazur, E.; et al. Relaxed phase-matching constraints in zero-index waveguides. *Phys. Rev. Lett.* **2022**, *128*, 203902.
(30) Jun, Y. C.; Reno, J.; Ribaudo, T.; Shaner, E.; Greffet, J. J.; Vassant, S.; Marquier, F.; Sinclair, M.; Brener, I. Epsilon-near-zero strong coupling in metamaterial-semiconductor hybrid structures. *Nano Lett.* **2013**, *13*, 5391−5396.
(31) Campione, S.; Wendt, J. R.; Keeler, G. A.; Luk, T. S. Near-infrared strong coupling between metamaterials and epsilon-near-zero modes in degenerately doped semiconductor nanolayers. *ACS Photonics* **2016**, *3*, 293−297.
(32) Alam, M. Z.; Schulz, S. A.; Upham, J.; De Leon, I.; Boyd, R. W.Large optical nonlinearity of nanoantennas coupled to an epsilon-near-zero material. *Nat. Phot.***2018**, *12*, 79,.
(33) Wang, K.; Liu, A.-Y.; Hsiao, H.-H.; Genet, C.; Ebbesen, T. Large Optical Nonlinearity of Dielectric Nanocavity-Assisted Mie Resonances Strongly Coupled to an Epsilon-near-Zero Mode. *Nano Lett.* **2022**, *22*, 702−709.
(34) Passler, N. C.; Gubbin, C. R.; Folland, T. G.; Razdolski, I.; Katzer, D. S.; Storm, D. F.; Wolf, M.; De Liberato, S.; Caldwell, J. D.; Paarmann, A. Strong Coupling of Epsilon-Near-Zero Phonon Polaritons in Polar Dielectric Heterostructures. *Nano Lett.* **2018**, *18*, 4285−4292.
(35) Runnerstrom, E. L.; Kelley, K. P.; Folland, T. G.; Nolen, J. R.; Engheta, N.; Caldwell, J. D.; Maria, J.-P. Polaritonic Hybrid-Epsilon-near-Zero Modes: Beating the Plasmonic Confinement vs Propagation-Length Trade-Off with Doped Cadmium Oxide Bilayers. *Nano Lett.* **2019**, *19*, 948−957.
(36) Forn-Díaz, P.; Lamata, L.; Rico, E.; Kono, J.; Solano, E.Ultrastrong coupling regimes of light-matter interaction. *Rev. Mod. Phys.***2019**, *91*, DOI: 10.1103/RevModPhys.91.025005.
(37) Frisk Kockum, A.; Miranowicz, A.; De Liberato, S.; Savasta, S.; Nori, F. Ultrastrong coupling between light and matter. *Nat. Rev. Phys.* **2019**, *1*, 19−40.
(38) Johnson, P. B.; Christy, R.-W. Optical constants of the noble metals. *Phys. Rev. B* **1972**, *6*, 4370.
(39) Hopfield, J. J. Theory of the contribution of excitons to the complex dielectric constant of crystals. *Phys. Rev.* **1958**, *112*, 1555−1567.
(40) Passler, N. C.; Razdolski, I.; Katzer, D. S.; Storm, D. F.; Caldwell, J. D.; Wolf, M.; Paarmann, A. Second Harmonic Generation from Phononic Epsilon-Near-Zero Berreman Modes in Ultrathin Polar Crystal Films. *ACS Photonics* **2019**, *6*, 1365−1371.
(41) De Ceglia, D.; Scalora, M.; Vincenti, M. A.; Campione, S.; Kelley, K.; Runnerstrom, E. L.; Maria, J.-P.; Keeler, G. A.; Luk, T. S. Viscoelastic optical nonlocality of low-loss epsilon-near-zero nanofilms. *Sci. Rep.* **2018**, *8*, 1−11.
(42) Todorov, Y.; Andrews, A. M.; Colombelli, R.; De Liberato, S.; Ciuti, C.; Klang, P.; Strasser, G.; Sirtori, C. Ultrastrong light-matter coupling regime with polariton dots. *Phys. Rev. Lett.* **2010**, *105*, 196402.
(43) Dionne, J. A.*Flatland photonics: circumventing diffraction with planar plasmonic architectures*. Ph.D. thesis, California Institute of Technology, 2009; pp 162−174.
(44) Vassant, S.; Hugonin, J.-P.; Marquier, F.; Greffet, J.-J. Berreman mode and epsilon near zero mode. *Opt. Exp.* **2012**, *20*, 23971.
(45) Campione, S.; Liu, S.; Benz, A.; Klem, J. F.; Sinclair, M. B.; Brener, I.Epsilon-near-zero modes for tailored light-matter interaction. *Phys. Rev. Appl.***2015**, *4*, DOI: 10.1103/PhysRevApplied.4.044011.
(46) Runnerstrom, E. L.; Kelley, K. P.; Folland, T. G.; Nolen, J. R.; Engheta, N.; Caldwell, J. D.; Maria, J. P. Polaritonic Hybrid-Epsilon-near-Zero Modes: Beating the Plasmonic Confinement vs Propagation-Length Trade-Off with Doped Cadmium Oxide Bilayers. *Nano Lett.* **2019**, *19*, 948−957.
(47) Ghindani, D.; Rashed, A. R.; Habib, M.; Caglayan, H. Gate Tunable Coupling of Epsilon-Near-Zero and Plasmonic Modes. *Adv. Opt. Mater.* **2021**, *9*, 2100800.
(48) MacDonald, K. F.; Sámson, Z. L.; Stockman, M. I.; Zheludev, N. I. Ultrafast active plasmonics. *Nat. Phot.* **2009**, *3*, 55−58.
(49) Raether, H.*Surface Plasmons on Smooth and Rough Surfaces and on Gratings*; Springer, 1988; pp 4−39.
(50) Liu, C.; Alam, M. Z.; Pang, K.; Manukyan, K.; Reshef, O.; Zhou, Y.; Choudhary, S.; Patrow, J.; Pennathurs, A.; Song, H.; et al. Photon Acceleration Using a Time-Varying Epsilon-near-Zero Metasurface. *ACS Photonics* **2021**, *8*, 716−720.
(51) Zhou, Y.; Alam, M. Z.; Karimi, M.; Upham, J.; Reshef, O.; Willner, A. E.; Boyd, R. W. Broadband frequency translation through time refraction in an epsilon-near-zero material. *Nat. Commun.* **2020**, *11*, 2180.
(52) Pang, K.; Alam, M. Z.; Zhou, Y.; Liu, C.; Reshef, O.; Manukyan, K.; Voegtle, M.; Pennathur, A.; Tseng, C.; Su, X.; et al. Adiabatic Frequency Conversion Using a Time-Varying Epsilon-Near-Zero Metasurface. *Nano Lett.* **2021**, *21*, 5907−5913.
(53) Lambrecht, A. Electromagnetic pulses from an oscillating high-finesse cavity: possible signatures for dynamic Casimir effect experiments. *J. Opt. B: Quantum Semiclassical Opt.* **2005**, *7*, S3.